

NATIONAL & INTERNATIONAL SCIENTIFIC EVENTS

International Conference on Research in Engineering, Technology and Science (ICRETS)

Venue: Novotel Berlin Mitte
Location: Berlin, Germany

Begins: January 27, 2020
Ends: January 31, 2020

13th International Joint Conference on Biomedical Engineering Systems and Technologies

Venue: Grand Hotel Excelsior
Location: Valletta, Malta

Begins: February 24, 2020
Ends: February 26, 2020

14th Mediterranean Congress of Chemical Engineering

Venue: Gran Via Venue
Location: Barcelona, Spain

Begins: June 2, 2020
Ends: June 5, 2020

The 49th International Congress and Exposition on Noise Control Engineering

Venue: Convention and Exhibition Center
Location: Seoul, Korea

Begins: August 23, 2020
Ends: August 26, 2020

FISITA World Congress 2020

Venue: O₂ Universum
Location: Prague, Czech Republic

Begins: September 14, 2020
Ends: September 18, 2020

46th Annual Conference of the IEEE Industrial Electronics Society-IECON 2020

Venue: Marina Bay Sands Expo and Convention Centre
Location: Malaysia

Begins: October 18, 2020
Ends: October 21, 2020

11th International Conference on Environmental Science and Development

Venue: K+K Hotel
Location: Barcelona, Spain

Begins: February 10, 2020
Ends: February 12, 2020

17th World Conference on Continuing Engineering Education (IACEE 2020)

Venue: NTNU Campus
Location: Trondheim, Norway

Begins: May 26, 2020
Ends: May 29, 2020

34th European Composite Materials Congress

Venue: Viking Line Terminal
Location: Stockholm, Sweden

Begins: June 9, 2020
Ends: June 11, 2020

36th European and 12nd International Peptide Symposium

Venue: Hotel Meliá Sitges
Location: Barcelona, Spain

Begins: August 30, 2020
Ends: September 04, 2020

14th International Conference on Hydrosience and Engineering

Venue: Radisson Blu Resort & Spa
Location: Cesme, Turkey

Begins: September 22, 2020
Ends: September 25, 2020

23rd International Conference on Electrical Machines and Systems (ICEMS2020)

Venue: ACT CITY Hamamatsu
Location: Hamamatsu, Japan

Begins: November 24, 2020
Ends: November 27, 2020

JOURNAL OF SCIENCE & ENGINEERING

HITTITE

HJSE Official Journal of Hitit University Volume 6, Issue 4, 2019 www.hjse.hitit.edu.tr



HJSE Official Journal of Hitit University Volume 6, Issue 4, 2019 www.hjse.hitit.edu.tr



Abstracted & Indexed in:

TR Dizin Mühendislik ve Temel Bilimler Veri Tabanı | CrossRef | Google Scholar | MIP Database | StuartxChange | ResearchBib | Scientific Indexing Services (SIS)

HITTITE

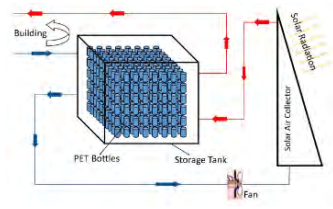
Volume 6, Issue 4, 2019

www.hjse.hitit.edu.tr

Determination of Effect of Bottle Arrangement in the Sensible Thermal Energy Storage System Consisting of Water-Filled PET Bottles on Thermal Performance
 235-242

Dogan Erdemir

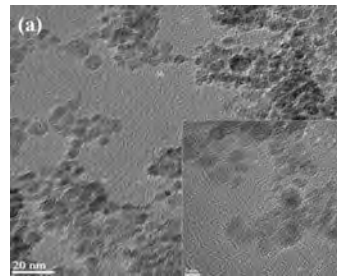
This study presents a theoretical investigation for determining the effect of bottle arrangement on the stored energy amount in the solar heating system.



Magnetic Properties of Manganese Ferrite (MnFe₂O₄) Nanoparticles Synthesized by Co-Precipitation Method
 243-249

Evrin Umut

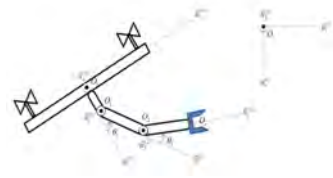
In the presented study, manganese ferrite (MnFe₂O₄) nanoparticles were synthesized by applying a modified co-precipitation method based on the decomposition of metallic precursors in a liquid phase environment in the presence of surfactant oleic acid.



Decoupled Cascaded PID Control of an Aerial Manipulation System
 251-259

Nebi Bulut, Ali Emre Turgut and Kutluk Bilge Arikan

This paper presents the control of an aerial manipulation system with a quadrotor and a 2-DOF robotic arm.



Probiotic Properties of some Lactobacillus spp. that can survive in the Presence of Viral Gastroenteritis
 261-267

Elmas Ceren Ikiz, Gulcin Alp Avci and Hande Alp

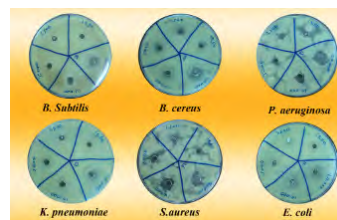
Therefore, to be able to identify the strains that can survive in viral acute gastro-enteritis and their distinguishable features, seven strains of *Lactobacillus spp.* were isolated from the stool samples of 0-5 year old children with viral gastroenteritis in this study.



Investigation of Antibacterial and Cytotoxic Properties of Mix Ligand Complex of Zinc 2-Fluorobenzoate with Nicotinamide
 269-274

Cem Ozturk and Giray Bugra Akbaba

In this study, antibacterial properties of the previously synthesized zinc 2-fluorobenzo-ate with nicotinamide complex at 1.17; 2.33; 4.67; 9.34 and 18.67 mM concentrations was investigated using by agar well diffusion method against *Bacillus subtilis*, *Pseudomonasa eruginosa*, *Staphylococcus aureus*, *Escherichia coli*, *Bacillus cereus* and *Klebsiella pneumoniae* bacterias.



Performance Analysis of an integrated Semi-TransparentThin Film PV Vacuum Insulated Glazing
 275-286

Hasila Jarimi, Ke Qu, Shihao Zhang, Qinghua Lv, Daniel Cooper, Yuehong Su and Saffa Riffat

This paper is intended to design and develop a thermal model of an integrated semi-transparent thin-film PV vacuum glazing with four layers of glass called PV VG-4L.



Owner

Prof. Dr. Ali Osman ÖZTÜRK
on behalf of Hitit University

Editor-in-chief

Prof. Dr. Ali KILIÇARSLAN

Associate Editors

Prof. Dr. D. Ali KÖSE
Assist. Prof. Dr. Öncü AKYILDIZ

Production

Assoc. Prof. Dr. Kazım KÖSE
Mustafa Reşit HABOĞLU
Erhan ÇETİN
Harun Emre KIRAN
Ömer Faruk TOZLU

Editor's Office

Tel: +90 364 227 45 33 / 12 36

Fax: +90 364 227 45 35

Email: alikilicarslan@hitit.edu.tr

Subscription Service:

Tel: +90 364 227 45 33 / 12 82

Fax: +90 364 227 45 35

Email: hjse@hitit.edu.tr

EDITORIAL BOARD

Prof. Dr. İftikhar AHMAD

Prof. Dr. Mike BECKETT

Prof. Dr. İbrahim DİNÇER

Prof. Dr. Ali ELKAMEL

Prof. Dr. Mohamad S QATU

Prof. Dr. Saffa RIFFAT

Prof. Dr. Thanos SALIFOĞLU

Assoc. Prof. Dr. Yuehong SU

Dr. Wojciech NOGALA

Prof. Dr. Yusuf AYZAZ

Prof. Dr. Adil DENİZLİ

Prof. Dr. Ali GENÇER

Prof. Dr. Metin GÜRÜ

Prof. Dr. Murat HOŞÖZ

Prof. Dr. Sadık KAKAÇ

Prof. Dr. Tarık Ömer OĞURTANI

Prof. Dr. Ender SUVACI

Assoc. Prof. Dr. Ali TOPÇU

Prof. Dr. Kazım Savaş BAHÇECİ

Assoc. Prof. Dr. Cengiz BAYKASOĞLU

Prof. Dr. Naki ÇOLAK

Prof. Dr. Vedat DENİZ

Prof. Dr. Hakan GÜNGÜNEŞ

Prof. Dr. Bülent KABAK

Prof. Dr. Ali KILIÇARSLAN

Prof. Dr. Dursun Ali KÖSE

Prof. Dr. İrfan KURTBAŞ

Prof. Dr. İbrahim SÖNMEZ

Assoc. Prof. Dr. Seyfi ŞEVİK

Prof. Dr. Dilber Esra YILDIZ

University of Malakand, Chakdara, Pakistan

Bangor University, Bangor, United Kingdom

Uoit Ontario University, Ontario, Canada

University of Waterloo, Ontario, Canada

Central Michigan University, Michigan, United States

The University of Nottingham, United Kingdom

Aristotle University of Thessaloniki, Thessaloniki, Greece

The University of Nottingham, United Kingdom

Polish Academy of Sciences, Poland

Suleyman Demirel University, Turkey

Hacettepe University, Turkey

Ankara University, Turkey

Gazi University, Turkey

Kocaeli University, Turkey

TOBB University, Turkey

Middle East Technical University, Turkey

Anadolu University, Turkey

Hacettepe University, Turkey

Hitit University, Turkey

Hitit University, Turkey

Hitit University, Turkey

Hitit University, Turkey

Hitit University, Turkey

Hitit University, Turkey

Hitit University, Turkey

Hitit University, Turkey

Hitit University, Turkey

Hitit University, Turkey

Hitit University, Turkey

Hitit University, Turkey

Journal Name	: HITTITE JOURNAL OF SCIENCE AND ENGINEERING
Year	: 2019
Managing Editor	: Prof. Dr. Ali KILIÇARSLAN
Managing Office	: Hitit University Faculty of Engineering
Managing Office Tel	: +90 364 227 45 33 / 12 36
Publication Language	: English
Publication Type	: Peer Reviewed, Open Access, International Journal
Delivery Format	: 4 times a year (quarterly)
Print ISSN	: 2149-2123
Online ISSN	: 2148-4171
Publisher Address	: Hitit Üniversitesi Kuzey Kampüsü Çevre Yolu Bulvarı 19030 Çorum / TÜRKİYE
Publisher Tel	: +90 364 227 45 33/1236



This new issue of Hittite Journal of Science and Engineering contains twelve manuscripts from the disciplines of physics, biology, bio engineering, mechanical engineering, materials science and engineering. These manuscripts were first screened by Section Editors using plagiarism prevention software and then reviewed and corrected according to the reviewer's comments. I would like to express my gratitude to all our authors and contributing reviewers of this issue.

I would like to thank to the President of Hitit University, Prof. Dr. Ali Osman Öztürk, for his support and interest in HJSE and also to the Associate Editors of HJSE, namely Prof. Dr. Dursun Ali Kose and Asst. Prof. Dr. Oncu Akyildiz, as well as our Production Editors Dr. Kazim Kose, Mustafa Reşit Haboğlu, Erhan Çetin, Harun Emre Kıran and Ömer Faruk Tozlu for their invaluable efforts in making of the journal.

It's my pleasure to invite the researchers and scientists from all branches of science and engineering to join us by sending their best papers for publication in Hittite Journal of Science and Engineering.

Dr. Ali Kiliçarslan

Editor-in-Chief

Determination of Effect of Bottle Arrangement in the Sensible Thermal Energy Storage System Consisting of Water-Filled PET Bottles on Thermal Performance

Dogan Erdemir 

Erciyes University, Department of Mechanical Engineering, Kayseri, Turkey

ABSTRACT

This study presents a theoretical investigation for determining the effect of bottle arrangement on the stored energy amount in the solar heating system. 0.5-liter, 1.5-liter and 5-liter water-filled PET bottles, which are widely used in daily life, have been investigated in the terms of thermal energy storage performance. The total energy storage volume is 1,500 liters. The effects of inlet velocity, inlet temperature, bottle volume and bottle arrangement on the stored energy amount have been researched theoretically. At the end of this study, it is determined that using the water-filled PET bottles in the sensible thermal energy storage system is a practical, easy and cheap way to storing solar energy for short period storage. Additionally, since PET bottles have behaved like energy storage capsule, heat exchanger for charging and discharging processes are not required. The working fluid (air) directly circulates over PET bottles in charging and discharging periods. It is observed that decreasing bottle diameter (volume) increased the amount of thermal energy storage. The highest energy storage amount of 8,5 MW is seen in SN=1.25d and SP=2d in-line arrangement. Increasing inlet velocity and inlet temperature have increased the stored energy amount.

Keywords:

Sensible thermal energy storage, Solar heating, Capsule, PET bottle

Article History:

Received: 2019/07/30

Accepted: 2019/11/11

Online: 2019/12/31

Correspondence to: Dogan Erdemir,
Department of Mechanical Engineering,
Erciyes University, 38039, Kayseri, Turkey,
E-mail: erdemir@erciyes.edu.tr,
Phone: +90 352 207 66 66-32111,
Fax: +90 352 437 57 84

INTRODUCTION

Energy storage is a significant solution for the later or cheap usage of energy, when the energy source is unavailable or expensive. The main problem related to renewable energy utilization is the time difference between the energy demand and the availability of energy sources. The most common method for solving this mismatch problem is energy storage. Thermal energy storage (TES) is a common and advanced one among the energy storage methods [1, 2]. Basically, TES is to store the energy in a storage medium by converting the energy sources to heat. TES is divided into two sections, which are sensible and latent TES. While sensible TES is to store the energy as heat by changing the temperature of the storage medium, latent TES is to store the energy as heat by changing the phase of storage medium. TES types and storage materials are selected according to the storage capacity, environmental condition, working condition, type of energy sources, etc. Sensible TES

systems are widely used in small and medium-sized solar energy cooling and heating applications. Water is a convenient storage medium because of its reasonable physical features, relatively harmless, cheapness and easy accessibility [3]. Either the water is kept as a big storage volume such as the tanks, vessels, solar ponds or in many small capsules that are held in a big storage tank. Thermal stratification is the most important issue for the thermal performance of sensible thermal energy storage tanks. Thermal stratification in sensible thermal energy storage tanks has been investigated by many researchers [4-8].

A typical TES system consists of three different processes, which are charging, storing and discharging periods. In the charging period, energy is charged to a storage medium when the energy source is active and/or cheap. The charged energy is kept in an insulated storage container or tank with minimum loss during the

storing period. In the discharging period, the stored energy is used when the energy source is not active and/or expensive. Thus, energy storage systems continue to provide energy, when energy sources are inactive or expensive. For example, in solar energy water and volume heating systems, energy is charged to a storage medium (water, salt, rock bed, etc.) during the daytime hours. The charged energy is stored until the time it is needed. The stored energy is then used to heat up the water or volume. Thermal energy storage (TES) is one of the most advanced and mature among energy storage types.

Kologirou [9] has investigated different solar collectors and their applications. Stinner et al. [10] have determined the performance of building which is integrated sensible TES system. Li [11] has performed the performance evaluation for sensible TES systems over the energy and exergy calculations. Navarro et al. [12, 13] have published two review studies related with active and passive TES systems. Caliskan et al. [14] have performed energy and exergy analyses for evaluating the system performance in building heating system which consists thermo-chemical material and sensible TES. Anderson et al. [15] have researched the packed bed TES system. In their TES system, air is used as heat transfer fluid and alumina is used as storage medium. Cabeza and Or [16] have researched the performance of TES systems in heating and cooling applications for renewable energy sources. Dincer et al. [2] have conducted a study to determine the thermal performance for the sensible thermal energy storage systems. Tian and Zhao [17] have published a detail review study about solar collectors and thermal energy storage applications. Omu et al. [18] have developed a mixed integer programming for fascinating the design of solar domestic hot water system. Nkhonjera et al. [19] have prepared a review study about thermal energy storage designs, heat storage materials. Pintaldi et al. [20] have developed an approach for energetic evaluation of thermal energy storage options for high efficiency solar cooling systems. Ozturk [21] have performed the experimental study for investigating the daily storage of the solar energy by using the volcanic material as the sensible TES material. Rao et al. [22] have presented the theoretical investigation of heat storage characteristics and transient behavior of a sensible heat storage module of 10 MJ storage capacity designed for discharging the heat in the high temperature range for solar power plant applications. Mulane and Havardar [23] have carried out a review study on rock bed thermal energy storage system for thermal stratification and heat extraction. Rezaie et al. [24] have modeled and analyzed the transient behavior during charging and discharging of a fully mixed open TES. Kumar et al. [25] have researched rock bed solar thermal storage system for space heating applications. Alva

et al. [26] have summarized various solar thermal energy storage materials and thermal energy storage systems. The properties of solar thermal energy storage materials are discussed and analyzed.

There are many capsule shapes for TES systems. The most of these shapes are basis on cubic, cylindrical and spherical. Cylindrical and spherical capsules are widely used in the term of heat transfer characteristics. Because cylindrical and spherical capsules supply better the average heat transfer coefficient and lower pressure drop. Also Ismail and Henriquez [27] have emphasized that the plastic based material is useful for TES capsules in the terms of heat transfer and cost. The plastic-based material, such as PVC, PET etc., are widely used in TES system as capsule material, since they are enduring, easy-producing, relative harmless and cheap.

The use of water-filled PET bottles in solar thermal heating applications has been investigated by Altuntop et al. [28], Altuntop and Tekin [29] and Erdemir and Altuntop [30]. Altuntop et al. [28] have presented an analytic model for determining the performance of a sensible thermal energy storage system which is used water-filled PET bottles as a TES unit. Altuntop and Tekin [29] have presented the experimental findings for the solar energy-based floor heating system. TES unit of the system consists of the number of 5,120 1.5-liter water-filled PET bottles. At the end of their study, it has been found that the indoor sports hall can be heated by solar energy and sensible TES system. Erdemir and Altuntop [30] have performed the energy and exergy analyses in order to evaluate the solar energy heating system which is an integrated sensible TES system consists of water-filled PET bottles.

It is observed from the literature survey that using water-filled PET bottles in a sensible TES system is an easy, cheap and ready to use solution for the short period storage of solar energy. Also, there is no clear study related to determining in different working and design conditions the thermal performance of sensible TES unit which consists of water-filled PET bottles. In this study, the effects of bottle volume, bottle arrangement, inlet velocity and inlet temperature on the thermal performance of sensible TES system which is consisted of water-filled PET bottles have been researched theoretically. 0.5-liter, 1.5-liter and 5-liter PET bottles have been used in in-line and staggered arrangements. Different inlet velocity and inlet temperature have been studied. Consequently, in the present study, both the design of system and working conditions have been investigated for the sensible TES unit which consists of water-filled PET bottles.

MATERIAL AND METHODS

Details of the System and PET Bottles

The schematic view of the solar energy heating system, which has the TES system consisted of water-filled PET bottles, is shown in Fig. 1. Solar energy heating system consists of solar collectors, fan, storage unit, water-filled PET bottles and installation equipment. The fans are used for cycling the working fluid air. Air is the working fluid in this study. This system works in three different periods.

1. The heated air in the solar collector is sent to indoor directly when the building needs heating
2. The heated air in the solar collector is sent to TES unit in order to store the solar energy when the building doesn't need heating
3. The stored energy is used, when solar energy not active and building needs heating

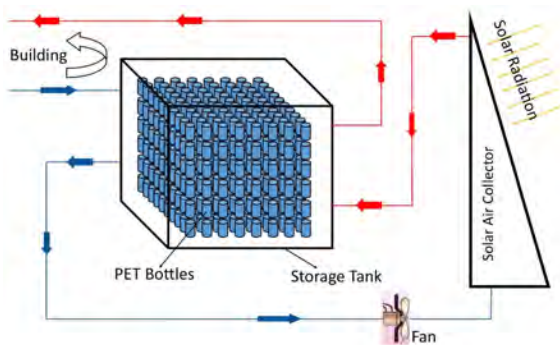


Figure 1. The schematic view of the system

In this study, 0.5-liter, 1.5-liter and 5-liter PET bottles, which are widely used in daily life, have been used as the energy storage capsule in TES system. In addition to being used as energy storage capsules, PET bottles act like heat exchangers. So, the heat exchanger for charging and discharging periods is not required in the system. Air (working fluid) circulates directly over the PET bottles. The views and dimensions of PET bottles are seen in Fig. 2. TES performance of PET bottles has been investigated by placing PET bottles in different arrangements (in-line and staggered) and positions (S_N and S_p). Also, different inlet temperatures and inlet velocities have been studied in order to determine system behavior in different working conditions. Heat transfer analyses have been performed theoretically. Some empirical equations have been applied to the system for determining the amount of stored energy. During the calculations, PET bottles have been assumed as cylinders that have a diameter (d) and the height (H) given, shown in Fig. 2.

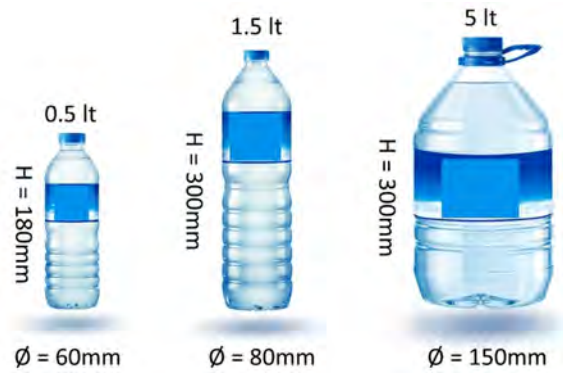


Figure 2. The views and dimensions of PET bottles

Details of Storage Unit and Heat Transfer Analysis

The schematic view of the storage unit is given in Figure 1. 0.5-liter, 1.5-liter and 5-liter PET bottles have been placed to the storage unit in in-line and staggered arrangements, respectively. The total storage volume is 1500 liters. PET bottles have been placed with 10 x 10 arrangement on horizontal plane. Namely, there are 10 bottles in columns and rows on the horizontal plane. The bottle arrangement on the horizontal plane has been considered as constant because the arrangement on the horizontal plane had a significant effect on heat transfer analysis. So, the bottle arrangement in the horizontal plane has been taken as same for all bottle types, in order to compare in the term of heat transfer and storage performance.

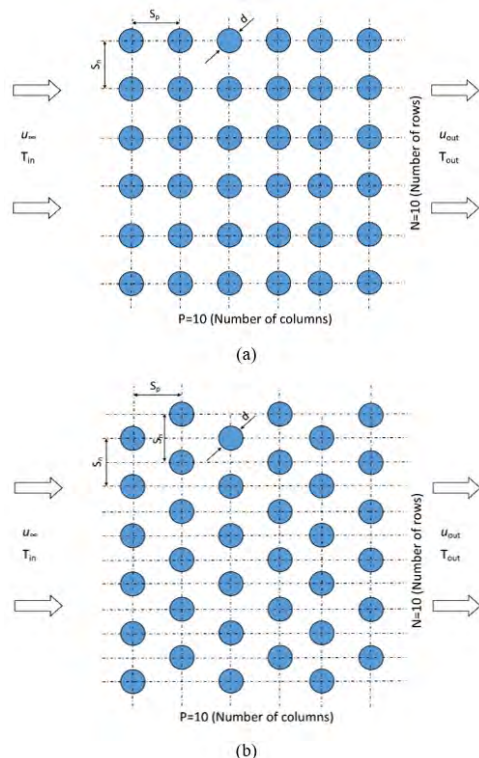


Figure 3. The arrangements of PET bottles a) in-line, b) staggered

The number of bottles in the vertical direction has been changed for different bottle arrangements in order to set the total storage volume of 1500 liters. In the present study, there are 30 arrays for 0.5-liter bottle, 10 arrays for 1.5-liter and 3 arrays for 5-liter in the vertical plane. Total numbers of 0.5-liter bottles are 3000 pieces, 1.5-liter bottles are 300 pieces and 5-liter bottles are 300 pieces. The arrangements in the horizontal plane of PET bottles are seen in Fig. 3. PET bottles have been placed in two different arrangements in the horizontal plane. These are in-line (Fig. 3.a) and staggered (Fig. 3.b). The distance between the bottles has been taken as 1.25d, 1.50d and 2.00d in rows and columns. It is considered that there is no distance between the bottles in the vertical direction. Besides the bottle arrangement, the effects of air inlet velocity and inlet temperature on TES performance have investigated.

Heat transfer analysis for heated air flow across the PET bottles array has been calculated by equations, which is presented by Grimson [31] and situated in Holman [32]. The average heat transfer coefficient in tube banks (PET bottles) can be calculated as follows:

$$Nu_{(d,f)} = \frac{hd}{k_f} = C Re_d^n Pr_f^{1/3} \tag{1}$$

where C and n are constant coefficients taken from the table which is situated in [32]. During the flow across the tube bank, the maximum velocity in tube banks u_{max} must be calculated for determining the maximum Reynolds number $Re_{d,max} \cdot u_{max}$ for in-line and staggered arrangements are given below, respectively:

$$u_{max} = u_{\infty} (S_n / (S_n - d)) \tag{2}$$

$$u_{max} = \frac{u_{\infty} (S_n / 2)}{\left((S_n / 2)^2 + S_p^2 \right)^{1/2} - d} \tag{3}$$

After calculating u_{max} , the maximum Reynolds number ($Re_{d,max}$) can be calculated by Eq.4.

$$Re_{d,max} = \frac{\rho_f u_{max} d}{\mu_f} \tag{4}$$

The average heat transfer coefficient can be calculated by writing $Re_{d,max}$ in Eq.1. The working fluid has been assumed as incompressible. Physical properties of the fluid have been taken as depended on temperature. Also, heat loss has not been taken into consideration. Stored energy amount can be defined as below:

$$\dot{Q}_{stored} = A_{1,sur} (T_{sur} - T_{bulk}) \tag{5}$$

where T_{sur} is the surface temperature of PET bottles and T_{bulk} is the bulk fluid temperature. Also, stored energy amount, \dot{Q}_{stored} is equal to charged energy amount $\dot{Q}_{charged}$,

given in Eq.6.

$$\dot{Q}_{charged} = \dot{m} c_{p,f} (T_{in} - T_{out})$$

The outlet temperature of air from storage unit can be calculated by considering $T_{bulk} = (T_{in} - T_{out}) / 2$ and $\dot{Q}_{charged} = \dot{Q}_{stored}$. Also, T_{sur} can be taken as water temperature inside the bottle.

RESULTS AND DISCUSSION

In this study, the amount of the stored heat in the water filled PET bottles has been investigated theoretically. PET bottles have been placed to a storage tank in in-line and staggered arrangements, respectively. The distances in columns and rows between the PET bottles have been taken as 1.25d, 1.50d and 2.00d. Additionally, the effect of inlet temperature and inlet velocity on thermal energy storage performance have been researched. The parameters used in the present work are summarized in Table 1. As seen from Table 1, 2700 different cases have been investigated. A program code has been developed by using MATLAB 2015a in order to analyze heat transfer in the storage unit. The effect of parameters given in Table 1 on the amount of stored energy has been calculated with this code.

Table 1. Studied parameters

Parameter	Value
Bottle volume, liter	0.5, 1.5, 5
Arrangements	in-line, staggered
S_n	1.25d, 1.5d, 2d
S_p	1.25d, 1.5d, 2d
Inlet velocity, u_{∞} , m/s	0.5, 1, 1.5, ..., 9, 9.5, 10
Inlet temperature, T_{in} , °C	50, 70, 80, 90

The Influence of Bottle Volume and Dimensions

0.5-liter, 1.5-liter and 5-liter PET bottles, which are widely used in daily life, have been used in the present study. Because the arrangement and number of bottles in horizontal plane are significant effect on heat transfer in the storage unit, PET bottles have been placed to horizontal plane in 10 x 10 arrangement. 1500 liters of the total storage volume has been considered. So, the number of bottles in the vertical plane is different. The number of bottles in the vertical plane has not important effect on the heat transfer analysis. Also, it has been considered that there is no distance between the PET bottles in the vertical position. The effect of PET bottle volumes on the stored energy amount (Q_{stored}) for different 12 cases are seen in Fig. 4. As seen from Fig. 4, the stored energy amount has decreased with the increasing bottle volume, because the diameter of bottle increases with increasing bottle volume. So, the maximum Reynolds number has increased with increasing bottle diameter. Higher Reynolds number has caused the higher Nusselt number and average heat transfer coefficient. Although the average

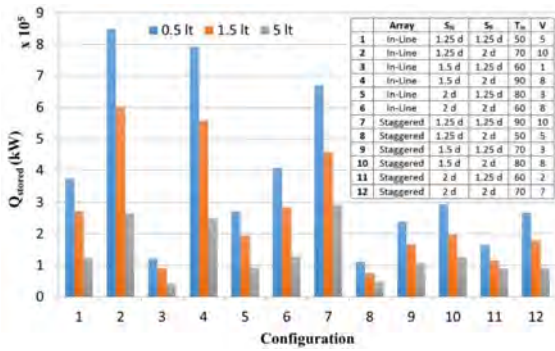


Figure 4. The effect of PET bottle volume on the stored energy amount

heat transfer coefficient has increased with increasing bottle diameter, the stored energy amount has decreased. Because, the total heat transfer surface area for the bottles has decreased with the increasing bottle diameter.

The Influences of Air Inlet Velocity and Temperature

The stored energy amount changing with the inlet velocity is seen in Fig. 5 for the case, which is $S_N=1.25d$, $S_p=1.25d$ and $T_{in}=70$ °C for 5-liter bottle. The treatment seen in Fig. 5 is same for the all cases. $Re_{d,max}$, Q_{stored} , Nu and h have increased with increasing inlet velocity. Because, the turbulent effect in storage unit has increased with increased inlet velocity. So, the stored energy amount has increased with increasing inlet velocity.

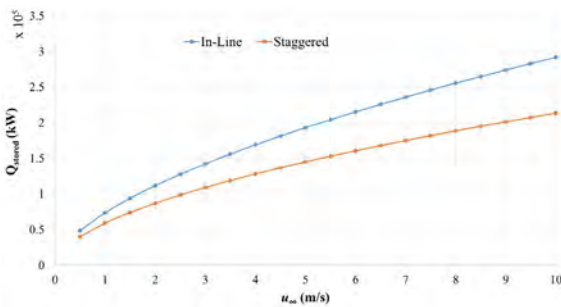


Figure 5. The effect of inlet velocity on the thermal performance of sensible TES

The effect of air inlet temperature on the stored energy amount, Q_{stored} , is seen in Fig. 6. Different five cases are given in Fig. 6. All cases in the present study have showed same behavior with the five cases seen in Fig. 6. As can be seen from Fig. 6, the stored energy amount has increased with higher inlet temperature. Because higher inlet temperature has caused to higher temperature difference between the bottle surface and the bulk temperature. Besides that, the rate of increase of Q_{stored} is not same with the temperature increasing rate. While the inlet temperature has increased from 50 to 90 °C, Q_{stored} increased 27, 21, 17, 14%.

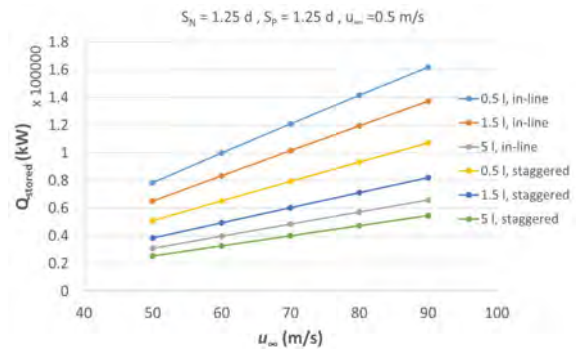


Figure 6. The effect of inlet temperature on the thermal performance of sensible TES

The Influence of PET Bottle Arrangement

Flow over the PET bottles located in the first row is similar the flow over the single PET bottle. When downstream rows are considered, flow conditions depend strongly on the PET bottle arrangement. In in-line arrangement, the pipes stayed back side of the first row are under the higher turbulent affect. With the decreasing S_p , the heat convection coefficient increases due to turbulence effects. In general, the overall heat transfer coefficient for a row increases up to fifth row. After fifth row, significant changing in heat transfer characteristic does not occur depending on flow conditioning. In staggered arrangement, the path of main flow is more complicated than in-line arrangement, so turbulence affects in storage unit is higher. Generally, in low Reynolds numbers ($Re_D < 100$) the overall heat transfer coefficient in staggered arrangement is higher than in-line arrangement. However, the difference in overall heat transfer coefficient between in-line and staggered arrangements decreases with the increasing Reynolds number. The difference in the heat transfer characteristics for the PET bottle arrangements is based on u_{max} and $Re_{d,max}$. These values change with the arrangements. As can be seen from Fig. 5, in-line arrangement shows better heat transfer performance in the same inlet velocity. In the present study, the air inlet velocity has been taken as input parameter. Although the air inlet velocity has been taken same, maximum air velocity in the storage unit and also Reynolds number has changed with the PET bottle arrangement. So, the maximum Reynolds number ($Re_{d,max}$) has been used for comparing the arrangements of PET bottles.

The stored energy amount changing with ($Re_{d,max}$) in in-line and staggered arrangements is seen in Fig. 7 for the case which is $S_N=1.25d$, $S_p=1.25d$, $T_{in}=70$ °C for 5-liter PET bottle (the same case with Fig. 5). As can be seen from Fig. 7 there is no significant difference between in-line and staggered arrangements in the terms of heat transfer characteristic and the stored energy amount. Because Reynolds num-

ber is high in this study. As emphasized before, the overall heat transfer coefficient has affected from the arrangements in low Reynolds number ($Re_D < 100$). All cases studied in the present study showed similar behavior with the case given in Fig. 7.

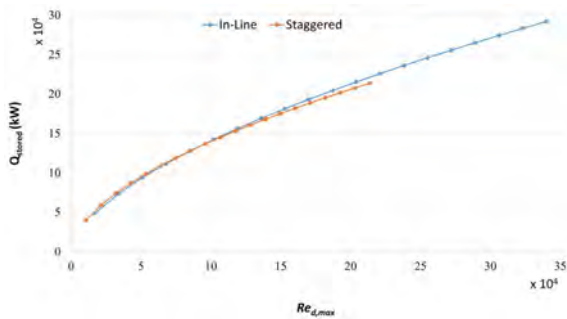


Figure 7. The effect of PET bottle arrangements on the thermal performance of sensible TES

The Influences of S_p and S_N Distances between PET Bottles

In this study, the effects of distances between the PET bottles, which are vertical to flow direction (S_N) and parallel to flow direction (S_p), on the stored energy amount have been investigated. S_N and S_p have been taken as 1.25d, 1.50d and 2.00d. The stored energy amount Q_{stored} changing with S_N and S_p for in-line and staggered arrangements are seen in Fig. 8 and Fig. 9, respectively. The selected case for Fig. 8 and Fig. 9 is $u_{in} = 5$ m/s, $T_{in} = 90$ °C and 0.5-liter PET bottle. The effects of S_N and S_p on the thermal performance are same with this selected case. As can be seen from S_N Fig. 8, in in-line arrangement, the stored energy amount has decreased substantially with the increasing S_N . Because, the turbulent effect has decreased with the increasing S_N distance, the heat transfer between air and water filled PET bottles also has decreased. Therefore, closer PET bottle placement in the direction vertical to flow direction has increased the stored energy amount. The effect of S_p on thermal energy storage performance is also seen in Fig. 9 for in-line arrangement. There is no significant effect of S_p on the thermal performance of system in the same S_N . When S_N increases from 1.25d to 1.50d, Q_{stored} has reduced a small amount. After 1.50d, Q_{stored} has increased a small amount. When all results considered for in-line arrangement, the lower S_N and lower S_p have supplied higher stored heat amount. The effects of S_N and S_p for the staggered arrangement on the system performance is seen in Fig. 9. In the staggered arrangement, in contrast with in-line arrangement, Q_{stored} has increased with increasing S_N . Because the turbulent effects has increased with increasing S_N in storage unit. Consequently, Nusselt number and the overall heat transfer coefficient have increased with the increasing S_N . Additionally, the stored heat decreased with the increasing S_p since the turbulent effects have decreased. Con-

sequently, in order to supply higher stored heat amount in staggered arrangement, S_N should be higher, and S_p should be lower.

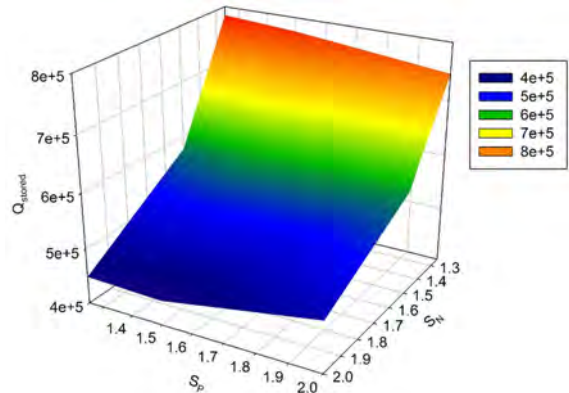


Figure 8. The effects of S_N and S_p on the amount of stored heat for the in-line arrangement

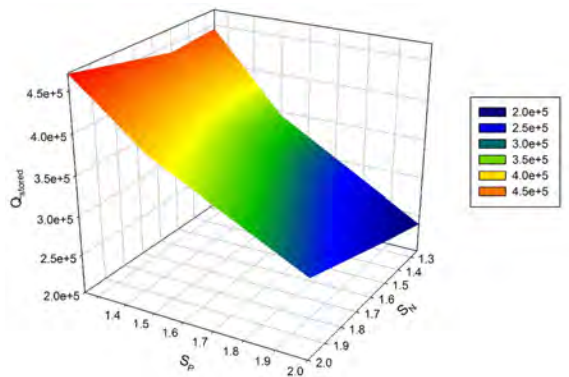


Figure 9. The effects of S_N and S_p on the amount of stored heat for the staggered arrangement

CONCLUSION

This study presents a determination of the effect of bottle arrangements on sensible thermal energy storage for the storage unit which is consisted of water-filled PET bottles. Also, different PET bottle volumes, which are widely used in daily life, 0.5-liter, 1.5-liter and 5-liter are studied. The effect of operating conditions which are inlet temperature and inlet velocity also researched. The total volume of the storage unit is 1500 liters. PET bottles are easy-produced, cheap and recycling materials. Also, they are ready to use. In the present study, the availability of PET bottles using as a thermal energy storage capsule has been investigated theoretically in solar heating system applications. Previous studies have shown that water-filled PET bottles are suitable for low temperature sensible thermal energy storage capsule. The heat exchangers for the collector and building cycles are not required when PET bottles (capsules) have been used in the thermal energy storage unit. In order to supply higher the amount of stored heat, lower volume water-filled PET bottles should be used in the system. There is no significant

difference between in-line and staggered arrangements in terms of the stored energy amount in the higher Reynolds number. Additionally, while lower S_N and S_p should be preferred in the in-line arrangement, higher S_N and lower S_p should be used in the staggered arrangement. The amount of highest stored energy of 8,5 MW is seen in $S_N=1.25d$ and $S_p=2d$ in-line arrangement. Ultimately, it has been observed that using water-filled PET bottles as a sensible thermal energy storage capsule is an easy, cheap, ready to use and high-performance solution.

NOMENCLATURE

Abbreviations

TES	Thermal energy storage
PET	Polyethylene terephthalate

Symbols

$A_{t,sur}$	Total surface area of PET bottles (m^2)
$c_{p,f}$	Specific heat for fluid ($kJ/kg K$)
d	The diameter of the PET bottle (m)
h	Heat transfer coefficient ($W/m^2 K$)
H	The height of the PET bottle (m)
k_f	Heat conduction coefficient for fluid
N	Number of rows
$Nu_{d,f}$	Nusselt number
P	Number of columns
Pr	Prandtl number
\dot{Q}_{stored}	The amount of the stored energy (W)
$\dot{Q}_{charged}$	The amount of the stored energy (W)
Re	Reynolds number
S_p	The distance parallel to the flow direction (m)
S_N	The distance normal to the flow direction (m)
T_{bulk}	Bulk temperature ($^{\circ}C$)
T_{out}	Outlet temperature ($^{\circ}C$)
T_{sur}	Surface temperature ($^{\circ}C$)
T_{in}	Inlet temperature ($^{\circ}C$)
u_{max}	Maximum velocity in the tube bank (m/s)
u_{∞}	Inlet velocity (m/s)
u_{out}	Outlet velocity (m/s)

Greek Letter

\emptyset	The diameter of the PET bottle
ρ_f	The density of the working fluid
μ_f	The viscosity of the working fluid

References

- Acar C. A comprehensive evaluation of energy storage options for better sustainability. *International Journal of Energy Research* 42 (2018) 3732–3746.
- Dincer I, Dost S, and Li X. Performance analyses of sensible heat storage systems for thermal applications. *International Journal of Energy Research* 21, 12 (1997) 1157–1171.
- Dincer I, Rosen MA. *Thermal Energy Storage Systems and Applications*, first ed. John Wiley and Sons, West Sussex, UK.
- Arslan M. Igci AA. Thermal performance of a vertical solar hot water storage tank with a mantle heat exchanger depending on the discharging operation parameters. *Solar Energy* 116 (2015) 184–204.
- Dragsted J, Furbo S, Dannemand M, Bava D. Thermal stratification built up in hot water tank with different inlet stratifiers. *Solar Energy* 147 (2017) 414–425.
- Erdemir D. Altuntop N. Improved thermal stratification with obstacles placed inside the vertical mantled hot water tanks. *Applied Thermal Engineering* 100 (2016) 20–29.
- Rosen MA. The exergy of stratified thermal energy storages. *Solar Energy* 71,3 (2001) 173–185.
- Rosen MA. Tang R. Dincer I. Effect of stratification on energy and exergy capacities in thermal storage systems. *International Journal of Energy Research* 28,2 (2004) 177–193.
- Kalogirou SA. Solar thermal collectors and applications. *Progress in Energy and Combustion Science*, 30,3 (2004) 231–295.
- Stinner S. Huchtemann K. Müller D. Quantifying the operational flexibility of building energy systems with thermal energy storages. *Applied Energy* 191 (2016) 140–154.
- Li G. Sensible heat thermal storage energy and exergy performance evaluations. *Renewable and Sustainable Energy Reviews* 53 (2016) 897–923.
- Navarro L. de Garcia A. Colclough S. Browne M. McCormack SJ. Griffiths P. Cabeza LF. Thermal energy storage in building integrated thermal systems: A review. Part 1. active storage systems. *Renewable Energy* 88 (2016) 526–547.
- Navarro L. de Garcia A. Niall D. Castell A. Browne M. McCormack SJ. Griffiths P. Cabeza LF. Thermal energy storage in building integrated thermal systems: A review. Part 2. Integration as passive system. *Renewable Energy* 85 (2016) 1334–1356.
- Caliskan H. Dincer I. Hepbasli A. Energy and exergy analyses of combined thermochemical and sensible thermal energy storage systems for building heating applications. *Energy and Buildings* 48 (2012) 103–111.
- Anderson R. Bates L. Johnson E. Morris JF. Packed bed thermal energy storage: A simplified experimentally validated model. *Journal of Energy Storage*, 4 (2015) 14–23.
- Cabeza LF. Oró E. 7 – Thermal energy storage for renewable heating and cooling systems, in *Renewable Heating and Cooling*, (2016) Woodhead Publishing. 139–179.
- Tian Y. Zhao CY. A review of solar collectors and thermal energy storage in solar thermal applications. *Applied Energy* 104 (2013) 538–553.
- Omu A. Hsieh S. Orehounig K. Mixed integer linear programming for the design of solar thermal energy systems with short-term storage. *Applied Energy*, 180 (2016) 313–316

19. Nkhonjera L. Bello-Ochende T. John G. King'onde CK. A review of thermal energy storage designs, heat storage materials and cooking performance of solar cookers with heat storage. *Renewable and Sustainable Energy Reviews*, 75 (2017) 157-167.
20. Pintaldi S. Sethuvenkatraman S. White S. Rosengarten G. Energetic evaluation of thermal energy storage options for high efficiency solar cooling systems. *Applied Energy* 188 (2017) 160-177.
21. Ozturk HH. Comparison of energy and exergy efficiencies of an underground solar thermal storage system. *International Journal of Energy Research*, 28,4 (2004) 341-353.
22. Rao CRC. Niyas H. Prasad L. Palanisamy M. Performance Investigation of Lab-Scale Sensible Heat Storage System (2018) Springer, Singapore. 169-186.
23. Mulane SA. Havaladar SN. A Review on Rock Bed Thermal Energy Storage System for Thermal Stratification and Heat Extraction. *International Journal of Current Engineering and Technology* 7 (2017) 335-337.
24. Rezaie B. Reddy BV. Rosen MA. Thermodynamic analysis and the design of sensible thermal energy storages. *International Journal of Energy Research* 41,1 (2017) 39-48.
25. Kumar A. Buddhi D. Yadav SK. Reddy SBK. Studies of Rock Bed Solar Thermal Storage System for Space Heating Applications. *Emerging Trends in Science and Technology* 3,11 (2016) 4764-4770.
26. Alva G. Liu L. Huang X. Fang G. Thermal energy storage materials and systems for solar energy applications. *Renewable and Sustainable Energy Reviews* 68 (2017) 693-706.
27. Ismail KAR. Henriquez JR. Numerical and experimental study of spherical capsules packed bed latent heat storage system. *Applied Thermal Engineering* 22,5 (2002) 1705-1716.
28. Altuntop N. Tekin Y. Demiral D. Analytical investigation of the use of water filled P.E.T. bottles as thermal energy storage unit. Paper presented at 4th International Thermal Energy Congress.
29. Altuntop N. Tekin Y. The first performance results of the solar heating and thermal energy storage by using P.E.T. bottles. Paper presented at European solar Congress (EUROSUN 2002).
30. Erdemir D. Altuntop N. Thermodynamic analysis of sensible thermal energy storage in water filled PET bottles. *International Journal of Exergy* 26,1-2 (2018) 77-92.
31. Grimson ED. Correlation and Utilization of New Data on Flow Resistance and Heat Transfer for Cross Flow of Gases over Tube Banks. *Trans. ASME* 59 (1937) 583-594.
32. Holman JP. *Heat Transfer* (2014) McGraw-Hill, Newyork.

Magnetic Properties of Manganese Ferrite (MnFe_2O_4) Nanoparticles Synthesized by Co-Precipitation Method

Evrım Umut 

Dokuz Eylül University, School of Healthcare, Department of Medical Imaging Techniques, Balçova, Izmir, Turkey

ABSTRACT

In the presented study, manganese ferrite (MnFe_2O_4) nanoparticles were synthesized by applying a modified co-precipitation method based on the decomposition of metallic precursors in a liquid phase environment in the presence of surfactant oleic acid. The synthesized sample was then characterized with X-ray Diffraction (XRD), standard and high resolution Transmission Electron Microscopy (TEM) and Fourier Transform Infrared Spectroscopy (FTIR), which revealed that the as-prepared MnFe_2O_4 particles are monodispersed nanocrystals with an average size of 4.7 nm and well surrounded with dimeric oleic acid coating. The magnetic properties of nanoparticles were first investigated by means of Superconducting Quantum Interference Device (SQUID) magnetometry. The temperature and field dependent magnetization measurements showed that the MnFe_2O_4 nanoparticles exhibit superparamagnetic property with zero coercivity at room temperature and thermal irreversibility. The superparamagnetic behavior of MnFe_2O_4 nanoparticles was further confirmed by conducting zero field Mössbauer Spectroscopy measurements on nanoparticle powders. As to fulfill all the requirements like crystallinity, small size and superparamagnetism, the prepared oleic acid coated MnFe_2O_4 nanoparticles has the potential to be used in biomedical applications like targeted drug delivery, MRI and hyperthermia.

Article History:

Received: 2019/07/30

Accepted: 2019/10/23

Online: 2019/12/31

Correspondence to: Evrim Umut,

Dokuz Eylül University, School of Healthcare,

Department of Medical Imaging Techniques,

Balçova, 35340, Izmir / Turkey

E-mail: evrim.umut@deu.edu.tr,

Phone: +90 (232) 412 47 20

Keywords:

Superparamagnetism, Manganese ferrite, Magnetic nanoparticles, SQUID magnetometry, Mössbauer spectroscopy.

INTRODUCTION

Nanostructured transition metal oxides, also known as spinel ferrites, are commonly studied due to their potential use in a variety of biomedical applications such as magnetic resonance imaging, hyperthermia and targeted drug delivery [1]. The general formula for ferrite family is given as MFe_2O_4 ; $\text{M}=\text{Zn}, \text{Ni}, \text{Co}, \text{Mn}$, where depending on the Curie temperature, magnetic anisotropy and magnetic moment of the substitution metal M, the overall magnetic properties of ferrites can be adjusted in order to optimize their performance in these biomedical applications. In this manner, manganese ferrite MnFe_2O_4 is a good candidate with its relatively high magnetization and biocompatibility [2,3]. For these reasons, nanosized MnFe_2O_4 particles were deeply investigated in literature, where particles were synthesized with different techniques and their surfaces were functionalized with different capping agents.

In the beginning of 2000s, Z. J. Zhang and co-workers, in a series of papers, showed the effect of particle size and interparticle interactions on the general magnetic behavior of MnFe_2O_4 nanoparticles synthesized with reverse microemulsion method [4-7]. By grafting a wide variety of ligands on the surface of MnFe_2O_4 nanoparticles, they also studied the relationship between surface coordination chemistry and the magnetic properties [8]. In 2009, A. Yang et al. demonstrated the change in Neel temperature depending on the cation distribution in MnFe_2O_4 particles prepared with co-precipitation method [9]. Later Aslibeiki and his colleagues, reported observation of a superspin glass-like behavior in nanosized MnFe_2O_4 particles produced by ball-milling technique, where they attribute the origin of this behavior to dipolar interactions among particles [10]. Following these studies, first papers reporting the implementation of MnFe_2O_4 nanoparticles into biomedical applications were published: Tromsdorf et al. [11]

presented the proton NMR relaxivities of superparamagnetic MnFe_2O_4 suspensions in water as a measure of their MRI contrast enhancement efficiencies for the first time. H. Yang et al. published a more comprehensive research, where they investigated the cytotoxicity and cellular uptake of such nanoparticles and compared their performance as MRI contrast agents by means of direct MR images both in-vitro and in-vivo [3]. Regarding the heat generation abilities of these particles D. H. Kim et al. focused on water dispersible surface modified MnFe_2O_4 nanoparticles, which are further coated with chitosan and can be loaded with drugs for possible drug delivery application. By obtaining infrared images of nanoparticle suspensions irradiated by a RF field, they revealed that these suspensions can be used as potential hyperthermia mediators [2].

In this study, we report the characterization results of oleic acid coated MnFe_2O_4 nanoparticles prepared with co-precipitation method and discuss the observed magnetic behavior of these particles on the basis of their physicochemical properties. The paper is organized as follows: In Section 2 the sample preparation procedure and the experimental details are briefly explained. The structural, surface and magnetic characterization results of properties of as-prepared MnFe_2O_4 nanoparticles are discussed in Section 3 and the concluding remarks are given in Section 4.

MATERIALS AND METHODS

MnFe_2O_4 nanoparticles were synthesized and in-situ coated with oleic acid (OA) following a modified chemical co-precipitation technique [12]. Briefly, a solution of 10 mmol $\text{FeCl}_3 \cdot 6\text{H}_2\text{O}$ and 5 mmol $\text{MnCl}_2 \cdot 6\text{H}_2\text{O}$ in 175 ml diethylene glycol (DEG) were mixed in a three neck flask for 1 h under magnetic stirring. By adding another separate 0.5 M NaOH solution in DEG and 4 hours of mixing under nitrogen (N_2) flow, the yellow color of the solution was gradually changed into brown. After heating the resulting solution to 210 °C of temperature, a mixture of oleic acid in DEG (8 mmol / 55 ml) was added. Finally, after 2 h, the solution was cooled down to room temperature and the particles were obtained as precipitate. After washing the precipitate with methanol and dispersing in toluene, as a size selection process, relatively larger particles were isolated from sample by subsequent precipitation, redispersing and centrifugation. All the chemical products were purchased from Sigma-Aldrich and Alfa Aesar company and used without further modification.

The structural characterization of synthesized particles were done by collecting XRPD (x-ray powder diffraction) patterns of the MnFe_2O_4 nanoparticles using a Rigaku D/Max-Ultima diffractometer working with Cu-K_α radiation produced under 40 kV and 40 mA, while the morphology

of the particles were investigated through standard and high resolution Transmission Electron Microscopy (TEM / HRTEM) images obtained with a JEOL JEM-2100F in bright field mode running with 200kV of acceleration voltage. The surface characterization of OA coated MnFe_2O_4 particles were realized by recording the infrared spectra with a Thermo Scientific ATR Fourier Transform Infrared (FTIR) spectrometer for wavenumbers between 4000-650 cm^{-1} .

The magnetic properties of as-prepared MnFe_2O_4 nanoparticles were investigated by conducting magnetometry experiments using a Quantum Design SQUID (Superconducting-Quantum-Interference-Device) MPMS magnetometer. Magnetic field and temperature dependent magnetization measurements were performed on nanoparticle powders. Field dependent measurements were performed by changing the applied magnetic field between ± 5 T at room and at 5 K temperature, while the temperature dependent measurements were done in zero field cooling (ZFC) and field cooling (FC) mode. In ZFC mode first, the sample was cooled down to 5 K without any magnetic field and then the magnetization was measured by applying 100 Oe of constant field and heating the sample back to room temperature. In FC mode, the magnetization is measured under the same static field by cooling down the sample back to 5 K temperature.

The room temperature ^{57}Fe Mössbauer spectra of powder nanoparticle sample was obtained by using a spectrometer equipped with a ^{57}Co γ -radiation source in rhodium matrix. The measurements were done in the transmission geometry in constant acceleration mode with a triangular shape of varying Doppler velocity, where the velocity calibration was done using a 10- μm thick Fe foil and the isomer chemical shifts were determined with respect to Fe.

RESULTS AND DISCUSSION

Fig.1 shows the X-ray powder diffraction (XRPD) pattern of as-prepared MnFe_2O_4 nanoparticles confirming the crystal nature of nanoparticles with cubic spinel structure. The peaks are broadened as compared to bulk crystals due to the nanoscale and the size of the nanocrystals can be calculated according to Debye-Scherrer formalism (Eq.1). In Eq.1, λ is the wavelength of used Cu-K_α radiation, θ is the half angle (in radians) at which the broadened Bragg reflection observed and β is the FWHM (full width at half maximum intensity) of the broadened peak.

$$D = \frac{0.9\lambda}{\beta \cos \theta} \quad (1)$$

By applying this formalism to (311) reflection peak, which is the least effected from experimental line broadening contributions, a mean crystallite size of $d = 4.5$ nm was calculated. This information was further validated with

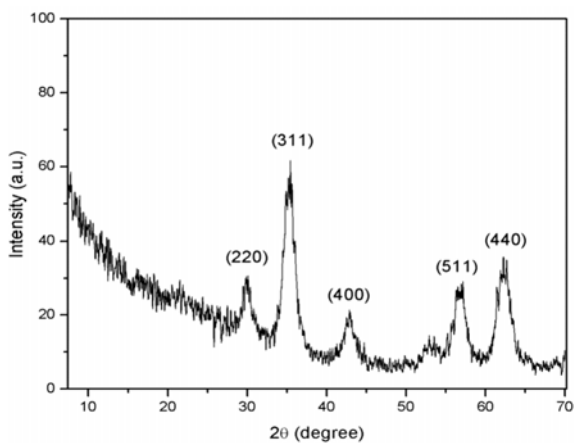


Figure 1. XRPD pattern of MnFe_2O_4 nanoparticles with indexing of peaks according to cubic spinel structure

TEM-HRTEM images of nanoparticles shown in Fig. 2a. The images show that the synthesized particles are mono-dispersed with almost spherical shape and separated from each other due to OA coating, however some agglomerates are present together with isolated particles. The size distribution histogram graph deduced from TEM images is also given in Fig. 2b, which is fitted with log-normal distribution function (solid red line) given in Eq.2 with a mean value of $d_{\text{mean}} = 4.77$ nm and standard deviation of $\sigma = 0.3$ nm, as consistent with XRPD results.

$$f(d) = \frac{1}{d\sqrt{2\pi\sigma^2}} \exp\left[-\frac{\ln\left(\frac{d}{d_{\text{mean}}}\right)^2}{2\sigma^2}\right] \quad (2)$$

Surface characterization of oleic acid (OA) coated MnFe_2O_4 nanoparticles were done by recording FTIR spectra as shown in Fig.3. The set of peaks observed in 3500-4000 cm^{-1} range are fingerprints of the vibrations of the hydroxyl group (O-H) in OA. One can associate the double peak lo-

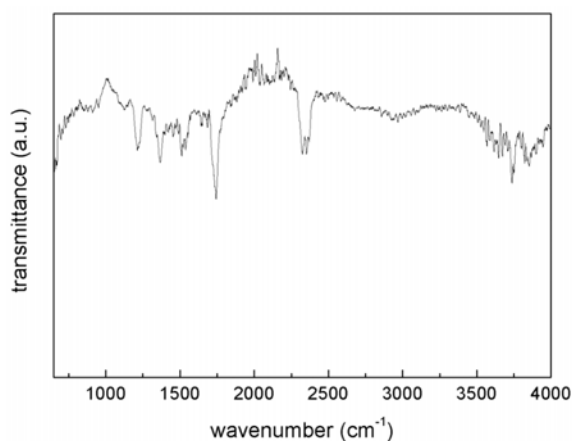


Figure 3. Infrared transmission spectra of oleic acid (OA) coated MnFe_2O_4 nanoparticle powder

cated around 2350 cm^{-1} with C-H stretching (asymmetric and symmetric mode) in the long ethyl chain (CH_2) in OA and methyl group (CH_3) at the end of this chain. Moreover, the strong peak at 1745 cm^{-1} can be attributed to C=O stretching, while the bands at 1512 cm^{-1} , 1370 cm^{-1} and 1210 cm^{-1} can be due to the C-O elongation and angular deformation of C-O-H bonds, which implies that OA molecules were successfully coated around the MnFe_2O_4 surface. One should here also state that; a broad characteristic peak for the intrinsic metal-oxygen bond vibrations occurring in the tetrahedral sites of the spinel structured MnFe_2O_4 magnetic core is generally observed around 600-570 cm^{-1} [3,13], which is unfortunately out of the scanning range of the used spectrometer in this study. However, the tail of this peak can be hardly seen at the shortest wavenumber limit of 650 cm^{-1} in Fig.3.

The magnetic behavior of as-prepared MnFe_2O_4 nanoparticles was investigated by means of magnetometry measurements. Fig.4 shows temperature (M-T) and field dependent (M-H) magnetization curves collected on powders.

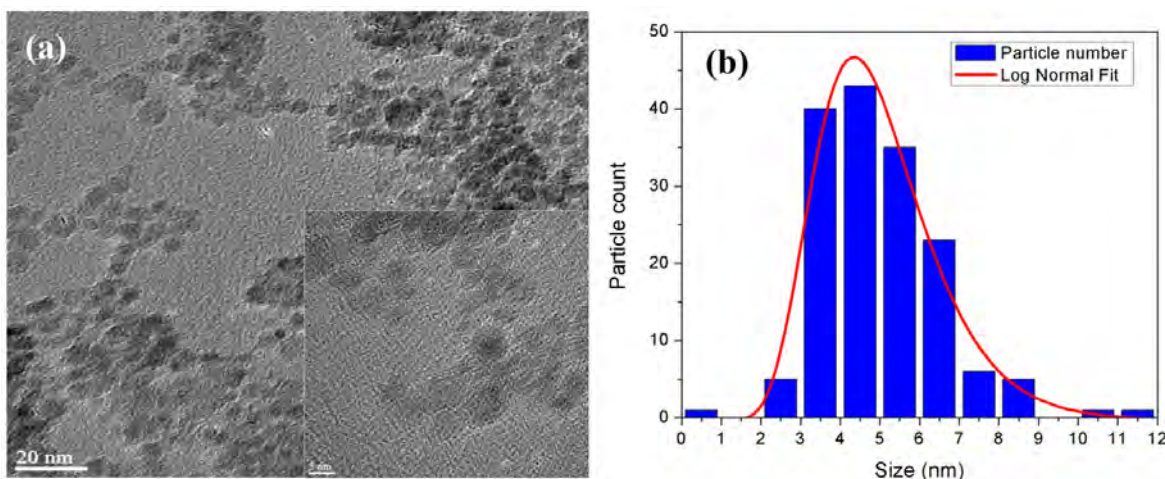


Figure 2. TEM (a) and HRTEM (inset of Fig. 2a) images of OA coated MnFe_2O_4 nanoparticles and size distribution histogram (b). Red curve shows fit with log-normal distribution function (Eq.2)

The zero coercivity observed at room temperature M-H curve (Fig.4a), together with the thermal irreversibility i.e. splitting of zero field cooling - field cooling (ZFC-FC) curves in M-T measurements (Fig.4b) indicates that the nanoparticles possess superparamagnetic behavior with thermally activated magnetization reversal and blocking phenomena. In M-H curve it is observed that the sample reaches a saturation magnetization of 55 emu/g. This value is smaller than the reported magnetization for bulk MnFe_2O_4 (82 emu/g) and the discrepancy originates from the enhanced surface-to-volume ratio of nanoparticles, where the canted surface spins do not contribute to overall magnetization. On the other hand, in M-T curve (Fig.4b) the average blocking temperature, which can be assigned as the maxima of ZFC curve, is approximately $T_b=40$ K and assuming that the particles' magnetic moments obey Arrhenius like reversal (Eq.3), as a first approximation one can roughly estimate a total magnetic anisotropy energy $K_{\text{total}}=2.8 \times 10^4 \text{ J/m}^3$ calculated by using the blocking condition $T_b \cong K_{\text{total}}/21k_B$ obtained for $\tau = 1$ s at $T=T_b$ and $\tau_0=10^{-9}$ s, where k_B is the Boltzmann constant and V is the particle volume [14].

$$\tau = \tau_0 \exp\left(\frac{K_{\text{total}}V}{k_B T}\right) \quad (3)$$

However, another observation on Fig.4b is that in FC curve the magnetization more or less stays constant below the blocking temperature ($T < T_b$) instead of increasing with the same rate as at high temperatures ($T > T_b$), which is an indication that interparticle interactions are effective and give rise to collective motion of particle moments i.e. spin-glass like behavior [15]. In this case, particle moment relaxation can be better described by Vogel-Fulcher-Tammann [16-18] like formalism (Eq.4) rather than the Arrhenius law and one should take into account that the above calculation for total magnetic anisotropy energy K_{total} is not very precise since it takes significant contribution from interactions among particles.

$$\tau = \tau_0 \exp\left(\frac{K_{\text{total}}V}{k_B(T-T_0)}\right) \quad (4)$$

It is also worthwhile to mention about the evolution of some anisotropy dependent parameters i.e. coercivity (coercive field) H_c , saturation magnetization M_s and remanent magnetization M_r with respect to the temperature. For single-domain particles, in the range of $T < T_b$ the temperature dependence of coercivity H_c follows the so called Kneller's law [19,20]:

$$H_c(T) = H_c(0) \left[1 - \left(\frac{T}{T_b}\right)^{1/2}\right] \quad (5)$$

where T_b is the blocking temperature and $H_c(0)$ is the coercivity value at $T=0$ K, which is equal to $H_c(0)=2K_{\text{total}}/\mu_0 M_s$ (in S.I. units) with μ_0 and M_s being the permeability of vacuum and the saturation magnetization at zero temperature, respectively. In Eq.5, by substituting the value of $H_c=240$ Oe for $T=5$ K obtained from M-H curve and the value of $T_b=40$ K obtained from M-T curve given in Fig.4, one calculates $H_c(0)=370$ Oe and the expected behavior of $H_c(T)$ can be depicted as in Fig.5a. The remanent magnetization M_r should follow the same trend with coercivity as to reach zero remanence for $T \geq T_b$ due to the fact that the thermal energy overcomes anisotropy energy barrier giving rise to superparamagnetic regime [19,21]. On the other side, the temperature dependence of M_s below the Curie temperature is generally described by Bloch's law [22] (owing to the behavior of spin wave excitations, particularly "magnons") as $M_s(T)=M_s(0)[1-(T/T_0)^\alpha]$, where the exponent is $\alpha=3/2$ for bulk systems and $\alpha < 2$ for nanosized materials [23,24]. Fig.5b shows a simulated curve of $M_s(T)$ (for $M_s(0)=73$ emu/g, $T_0=650$ K, $\alpha=1.55$) as to contain the experimental M_s values obtained from M-H curves at 300K and 5K given in Fig.4a. One should here note that, a more general approach descri-

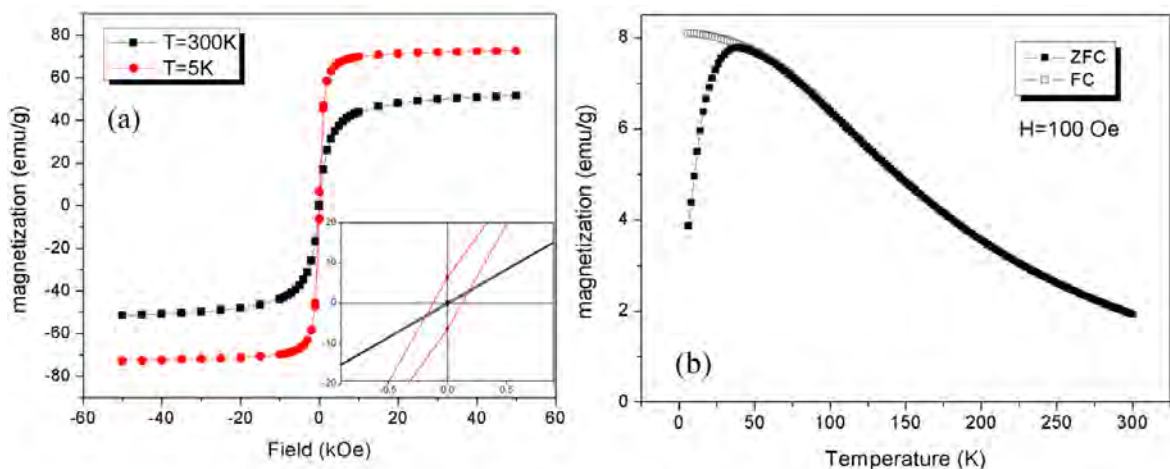


Figure 4. Magnetization curves as a function of magnetic field (a) and temperature (b) obtained on MnFe_2O_4 nanoparticles in powder. Inset graph in (a) shows the magnetization data in enlarged scale

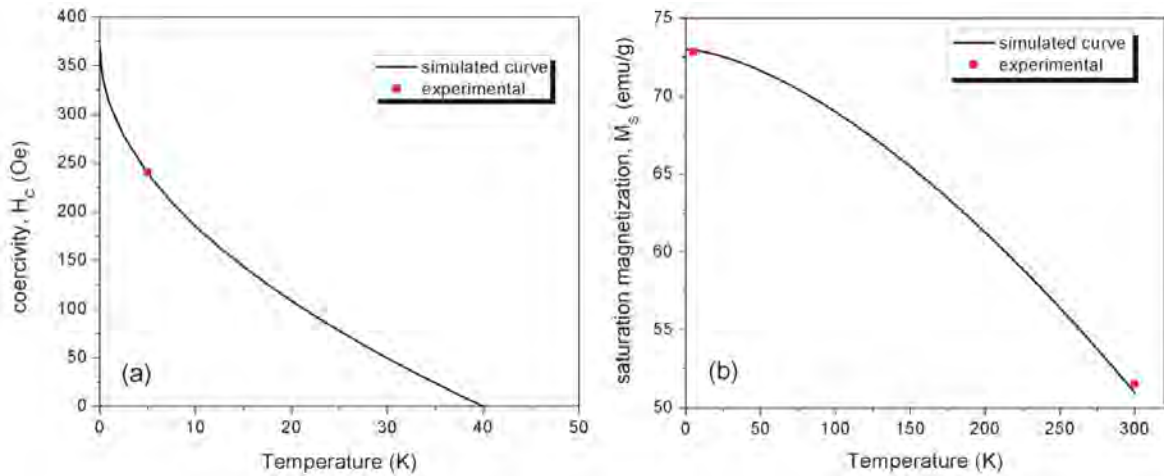


Figure 5. Simulated curves of (a) coercivity H_c according to Kneller's law for $H_c(0)=370$ Oe, $T_b=40$ K and (b) saturation magnetization M_s using Bloch's law for $M_s(0)=73$ emu/g, $T_0=650$ K, $\alpha =1.55$.

bing the temperature dependence of M_s takes into account the so called "surface spin freezing" effect manifesting itself at very low temperatures. In this case, the M_s is given by modified Bloch's law in the form $M_s(T)=M_s(0)[(1-(T/T_0)^\alpha + A_0 \exp(-T/T_f))]$, where the additional second term represents surface contribution with T_f being the freezing temperature at which the surface spins of nanoparticle become frozen (quenched) in a spin-glass like structure [24].

The magnetic properties of OA coated $MnFe_2O_4$ particles were further characterized with zero field ^{57}Fe Mössbauer spectroscopy. The technique measures the transitions between nuclear ground state ($I_g=1/2$) and excited state ($I_e=3/2$) of iron, which are splitted due to the quadrupolar interactions and/or hyperfine (Zeeman) interactions hence acts as a local probe providing information about the charge distribution, oxidation state and symmetry. The room temperature Mössbauer spectra of $MnFe_2O_4$ nanoparticles is shown in Fig.6. The observed intense absorption line at the centre (an asymmetric doublet) is a signature for superparamagnetic behavior of these nanoparticles, where the hyperfine field B_{hf} sensed by ^{57}Fe nuclei fluctuates much faster than the Larmor frequency of nuclear moments. In particular, at room temperature during one Larmor precession time thermal excitation is high enough to reorient the electronic spins more than several times to cancel the average value of B_{hf} which causes the observation of magnetically split levels (sextet) in Mössbauer spectra [25]. This is consistent with results obtained by magnetometry measurements, however considering that the Mössbauer experiment has a characteristic time scale (approximately 10^{-8} s) much shorter than the magnetometry technique (typically in the range of 1-100 seconds), a magnetic system appears superparamagnetic in magnetometry experiment may not appear superparamagnetic in Mössbauer spectroscopy, but observation of blocking features for such small nanoparticles (~4.5 nm for our

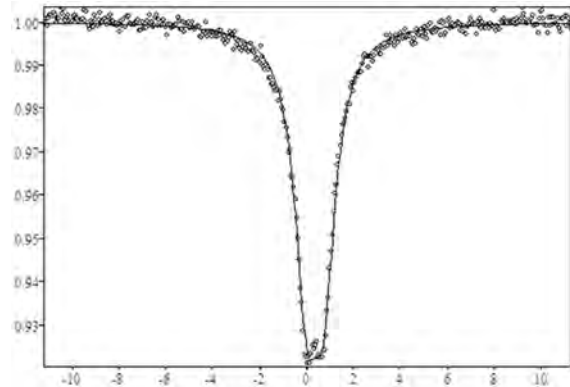


Figure 6. Room temperature ^{57}Fe Mössbauer spectra of $MnFe_2O_4$ nanoparticles (hollow circles) and theoretical fit (solid line)

$MnFe_2O_4$ particles) is only possible at low temperatures and/or under high magnetic fields.

On the other hand, the observation of a doublet (instead of a singlet line) is unambiguously is a result of quadrupolar splitting due to the coupling of Fe with Mn, which has a nuclear spin of $I=5/2$. In particular, the electric field gradient (EFG) induced by the quadrupolar Mn nuclei gives rise to a splitting of the excited state levels ($I=3/2$) of Fe nucleus and the line separation of the doublet gives the energy difference of these splitted levels. Mössbauer spectra was fitted with a special program using a least square technique (Fig.6) [26]. Table 1 summarizes the fit parameters, where A and Γ are the intensity and width of doublet lines, respectively, IS is the isomer chemical shift and QS is quadrupolar splitting in velocity unit (mm/s).

Table 1. The output parameters for fit shown in Fig.6. A: line intensity, Γ : line width, IS: isomer chemical shift, QS: quadrupolar splitting

A1 (imp.)	A2 (imp.)	A1/A2	Γ 1 (mm/s)	Γ 2 (mm/s)	IS (mm/s)	QS (mm/s)
-35898 ± 717	-34656 ± 717	1.036 ± 0.041	1.223 ± 0.014	1.223 ± 0.002	0.337 ± 0.008	0.734 ± 0.009

CONCLUSION

As a promising alternative to most widely used iron oxides in biomedical applications, MnFe_2O_4 particles were synthesized and in situ coated with organic surfactant by following a modified co-precipitation method. The structural characterization by means of XRD, TEM and surface characterization with FTIR experiments revealed that the as-prepared MnFe_2O_4 particles are monodispersed nanocrystallites with an average particle size around 4.5 nm and successfully coated with oleic acid. The SQUID magnetometry measurements performed on powder showed that the MnFe_2O_4 particles exhibit superparamagnetic behavior with zero coercivity at room temperature and thermal irreversibility in zero field cooled - field cooled (ZFC-FC) curves. From ZFC-FC curves the mean blocking temperature was found to be around $T_B=40$ K and the total magnetic anisotropy energy was approximately calculated as $K_{\text{total}}=2.8 \times 10^4 \text{ J/m}^3$. The observed room temperature saturation magnetization $M_S=55 \text{ emu/g}$, resulted to be smaller than the value of bulk MnFe_2O_4 due to the disordered surface spins and the non-increasing behavior of magnetization below T_B in FC curve implied spin-glass like collective particle moment reversal due to interparticle interactions. Based on the deduced parameters from experimental M-H and M-T curves, the expected temperature dependence of coercivity $H_c(T)$ and saturation magnetization $M_s(T)$ were simulated using Kneller's and Bloch's law, respectively. Room temperature ^{57}Fe Mössbauer spectroscopy measurements further confirmed the superparamagnetic property and the existence of Mn in the structure of MnFe_2O_4 based on the quadrupolar splitting in the spectral line. By fitting the Mössbauer spectra the magnitude of the quadrupolar splitting and isomer chemical shift were obtained. As a future study, in order to obtain the cation distribution in crystallite sites of MnFe_2O_4 and calculate the individual magnetic moment values further Mössbauer measurements at low temperatures are planned.

ACKNOWLEDGEMENTS

The author thanks to M. Coşkun from Hacettepe University for providing the sample and A. S. Kamzin from Ioffe Physical-Technical Institute of RAS (St.-Petersburg, Russia) for organizing Mössbauer measurements.

References

1. Umut E, Surface modification of nanoparticles used in biomedical applications, in: Mahmood Aliofkhazraei (Ed.), *Modern Surface Engineering Treatments*, IntechOpen Ltd., London, pp.185–208, 2013.
2. Kim DH, Nikles DE, Brazel CS. Synthesis and characterization of multifunctional chitosan – MnFe_2O_4 nanoparticles for magnetic hyperthermia and drug delivery. *Materials* 3 (2010) 4051–4065.
3. Yang H, Zhang C, Shi X, Hu H, Du X, Fang Y, Ma Y, Wu H, Yang S. Water-soluble superparamagnetic manganese ferrite nanoparticles for magnetic resonance imaging. *Biomaterials* 31 (2010) 3667–3673.
4. Liu C, Zou B, Rondinone AJ, Zhang ZJ. Reverse micelle synthesis and characterization of superparamagnetic MnFe_2O_4 spinel ferrite nanocrystallites. *Journal of Physical Chemistry B* 104 (2000) 1141–1145.
5. Liu C, Zhang ZJ. Size-dependent superparamagnetic properties of Mn spinel ferrite nanoparticles synthesized from reverse micelles. *Chemistry of Materials* 13 (2001) 2092–2096.
6. Rondinone AJ, Liu C, Zhang ZJ, Determination of magnetic anisotropy distribution and anisotropy constant of manganese spinel ferrite nanoparticles. *Journal of Physical Chemistry B* 105 (2001) 7967–7971.
7. Vestal CR, Song Q, Zhang ZJ. Effects of interparticle interactions upon the magnetic properties of CoFe_2O_4 and MnFe_2O_4 nanocrystals. *Journal of Physical Chemistry B* 108 (2004) 18222–18227.
8. Vestal CR, Zhang ZJ. Effects of surface coordination chemistry on the magnetic properties of MnFe_2O_4 spinel ferrite nanoparticles. *Journal of American Chemical Society* 125 (2003) 9828–9833.
9. Yang A, Chinnasamy CN, Greneche JM, Chen Y, Yoon SD, Chen Z, Hsu K, Cai Z, Ziemer K, Vittoria C, Harris VG. Enhanced Neel temperature in Mn ferrite nanoparticles linked to growth-rate-induced cation inversion. *Nanotechnology* 20 (2009) 185704–185713.
10. Aslibeiki B, Kameli P, Salamati H, Eshraghi M, Tahmasebi T. Superspin glass state in MnFe_2O_4 nanoparticles. *Journal of Magnetism and Magnetic Materials* 322 (2010) 2929–2934.
11. Tromsdorf UI, Bigall NC, Kaul MG, Bruns OT, Nikolic MS, Mollwitz B, Sperling RA, Reimer R, Hohenberg H, Parak WJ, Förster S, Beisiegel U, Adam G, Weller H. Size and surface effects on the MRI relaxivity of manganese ferrite nanoparticle contrast agents. *Nano Letters* 7 (2007) 2422–2427.
12. Caruntu D, Remond Y, Chou NH, Jun MJ, Caruntu G, He J, Goloverda G, O'Connor C, Kolesnichenko V. Reactivity of 3D transition metal cations in diethylene glycol solutions: Synthesis of transition metal ferrites with the structure of discrete nanoparticles complexed with longchain carboxylate anions. *Inorganic Chemistry* 41 (2002) 6137–6146.
13. Hosseini SH, Mohseni SH, Asadnia A, Kerdari H. Synthesis and microwave absorbing properties of polyaniline / MnFe_2O_4 nanocomposite. *Journal of Alloys and Compounds* 509 (2011) 4682–4687.
14. Umut E, Coşkun M, Pineider F, Berti D, Güngüneş H. Nickel ferrite nanoparticles for simultaneous use in magnetic resonance imaging and magnetic fluid hyperthermia,

- Journal of Colloid and Interface Science 5520 (2019) 199–209.
15. Dormann JL, Bessais L, Fiorani D. A dynamic study of small interacting particles: superparamagnetic model and spin-glass laws. *Journal of Physics C* 21 (1988) 2015–2034.
 16. Vogel H. The law of relation between the viscosity of liquids and the temperature. *Physikalische Zeitschrift* 22 (1921) 645–646.
 17. Fulcher GS. Analysis of recent measurements of viscosity of glasses. *Journal of American Ceramics Society* 8 (1925) 339–355.
 18. Tammann G, Hesse W. The dependence of viscosity upon the temperature of supercooled liquids. *Zeitschrift für Anorganische und Allgemeine Chemie* 156 (1926) 245–257.
 19. Kneller EF, Luborsky FE. Particle size dependence of coercivity and remanence of single-domain particles. *Journal of Applied Physics* 34 (1963) 656–658.
 20. Osman NSE, Moyo T. Temperature dependence of coercivity and magnetization of Sr_{1/3}Mn_{1/3}Co_{1/3}Fe₂O₄ ferrite nanoparticles. *Journal of Superconductivity and Novel Magnetism* 29 (2016) 361–366.
 21. Chatterjee BK, Ghosh CK, Chattopadhyay KK. Temperature dependence of magnetization and anisotropy in uniaxial NiFe₂O₄ nanomagnets: Deviation from the Callen–Callen power law. *Journal of Applied Physics* 116 (2014) 153904.
 22. Kaplan H. A spin-wave treatment of the saturation magnetization of ferrites. *Physical Review* 86 (1952) 121.
 23. Masina P, Moyo T, Abdallah HMI. Synthesis, structure and magnetic properties of Zn_xMg_{1-x}Fe₂O₄ nanoferrites. *Journal of Magnetism and Magnetic Materials* 381 (2015) 41.
 24. Gao RR, Zhang Y, Yu W, Xiong R, Shi J. Superparamagnetism and spin-glass like state for the MnFe₂O₄ nano-particles synthesized by the thermal decomposition method. *Journal of Magnetism and Magnetic Materials* 324 (2012) 2534–2538.
 25. Yoshida Y, Langouche G. (Eds.) *Mössbauer Spectroscopy*. Springer, 2013.
 26. Semenov VG, Panchuk VV. *Mössbauer Spectra Processing Program MossFit* (private communication)

Decoupled Cascaded PID Control of an Aerial Manipulation System

Nebi Bulut¹, Ali Emre Turgut¹, Kutluk Bilge Arikan²

¹Middle East Technical University, Department of Mechanical Engineering, Cankaya, Ankara, Turkey

²TED University, Department of Mechanical Engineering, Cankaya, Ankara, Turkey

ABSTRACT

This paper presents the control of an aerial manipulation system with a quadrotor and a 2-DOF robotic arm. Firstly, the kinematic model of the combined system and the Denavit-Hartenberg parameters of the serial robotic arm are obtained. Then, to derive the dynamics of the system, the quadrotor and the 2-DOF robotic arm are modeled as a combined system. The Lagrange-d'Alembert formulation is used to obtain the equation of motion of the combined system. Later, decoupled controllers are developed for the generalized coordinates. Decoupled cascaded PID controllers are designed for trajectory tracking of the combined system. Proposed control algorithms are implemented in the MATLAB/Simulink environment and tested using the highly nonlinear system model in simulation. The robustness of the controllers is checked by applying disturbance forces from different directions at the tip point of the 2-DOF robotic arm. The proposed control algorithms performed satisfactorily and showed very low absolute errors.

Keywords:

Aerial manipulation, Robotics, Quadrotor, PID control

Article History:

Received: 2019/08/10

Accepted: 2019/12/09

Online: 2019/12/31

Correspondence to: Nebi Bulut,

Department of Mechanical Engineering,
Middle East Technical University, Çankaya,
Ankara, Turkey,

E-mail: bulutnebi@gmail.com,

Phone: +90 507 575 0592

INTRODUCTION

In the last decade, great amount of research has been performed in the field of unmanned air vehicles (UAV). Among them, rotary wing UAV's i.e. quadrotors or their derivatives such as hexarotors and octorotors drew the most interest due to their simplicity and capabilities [1], [2], [3] and [4]. They have the ability to take-off and land vertically, they have the capability of high maneuverability and they are able to stay in hover position. They are mostly used for rescue, surveillance, and photography.

Nowadays, aerial manipulation attracts the attention of researchers since it brings new capabilities to quadrotors such as carrying payloads and manipulating objects. In most of the aerial manipulation related studies, a robotic arm is added under the UAV. In [8], [9] and [10]; serial manipulators with various degrees of freedom are studied. In [11], a parallel manipulator is exploited. [5], [6] and [7] are a few studies in which a cable suspended manipulator is used in the quadrotor.

There are mainly two different approaches for modeling of aerial manipulators. One approach is building

the kinematic and dynamic model of the UAV separately and taking the effects of the manipulator such as mass and inertia as a disturbance input to the UAV as in [12] and [13]. In the other approach, the UAV and the manipulator are modeled as a single system as in [8], [9] and [17]. For the control system design of aerial manipulators, there are also different approaches in the literature. The first approach is the designing the control algorithms by considering the disturbance forces that are applied to the system. In [14], a compliance controller is implemented to overcome the interaction forces between the end-effector and the environment. To cope with interaction forces and uncertainties while providing precise trajectory tracking, a robust controller design is proposed in [15]. Another aspect of the controller design is whether a single controller is designed to stabilize the coupled system or decoupled controllers are implemented for the vehicle system. In [17] a computed torque method is used to control the UAV and the 2-DOF robot arm. In [8], a single controller is designed by using the coupled equations in order to generate control inputs for both controlling the UAV and the robotic arm. However, in [13], decoupled controllers are presented

to regulate each state of the quadrotor and the robotic arm. The other aspect of the controller implementation is whether linear or nonlinear controllers are used to achieve stable system performance. In [16], the nonlinear model predictive control method is successfully studied to achieve optimized system performance. Linear controllers (PID) are designed to control the overall system via feedback linearized system equations [13].

In this paper, a UAV with a 2-DOF robotic arm mounted at its bottom is studied. Dynamics of the combined system is obtained by using Lagrange-d'Alembert formulation. Decoupled controllers are designed for controlling both the quadrotor and the arm. The performance and robustness of the controllers are shown using numerical simulations.

We improve the state-of-the-art in three different aspects. First, to the best of our knowledge, in most of the studies in the literature, the interaction of the end-effector with the environment is not modeled and most of the time the proposed controllers are tested without the interaction forces. However, in order to use aerial manipulators for tasks such as opening a door or pushing a box; the interaction forces have to be considered. In this paper, we considered interaction forces and designed the controller to be robust against these forces and tested its performance accordingly. Second, unlike a few studies that considered 1-D and small magnitude interaction force, we considered larger magnitude interaction forces in 3-D. Third, although the states of the aerial manipulator are highly coupled, our controller was able to control all states simultaneously unlike most of the studies in the literature.

The organization of this paper is as follows. In Section 2, the kinematic and dynamic modeling of the system are introduced. In Section 3, controller design is discussed. The results of the simulations are presented in Section 4. Finally, in Section 5, discussion of the results and the conclusion of the study are made.

MODELING

Kinematics

Position Analysis

The position analysis is the key factor for the kinematic modeling. Here, the position relations of the combined system and Denavit-Hartenberg parameters of the robotic arm are determined [17]. Fig. 1 shows some of the kinematic parameters of the system. Let $O_p, O_{p'}, O_p, O_2$ and O_b be the origin of the inertial, quadrotor's body, link-1, link-2 and end-effector fixed reference frames, respectively.

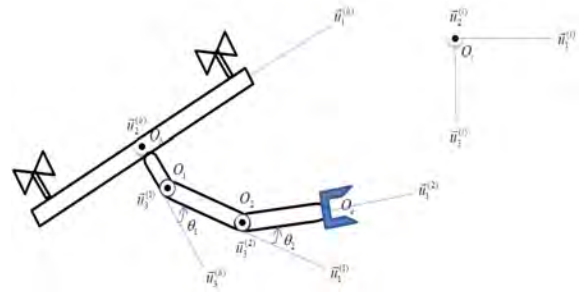


Figure 1. Side view of the unified system and some of the kinematic parameters

$\bar{u}_i^{(k)}$ is the k^{th} basis unit direction vector of the reference frame O_a . Their column matrix representation can be expressed as:

$$\bar{u}_1 = [1 \ 0 \ 0]^T, \bar{u}_2 = [0 \ 1 \ 0]^T, \bar{u}_3 = [0 \ 0 \ 1]^T \quad (1)$$

$\bar{\Omega} = [\theta_1 \ \theta_2]^T$ is the joint angles of the robotic arm. Orientation of the center of mass of the quadrotor is represented by the set of Euler angles; roll, pitch and yaw angles $\bar{\Upsilon} = [\phi \ \theta \ \psi]^T$. By using Euler angles, the rotation matrix between inertial-fixed reference frame to quadrotor body-fixed reference frame can be written as:

$$\hat{C}^{(i,b)} = \begin{bmatrix} c\psi c\theta & c\psi s\theta s\phi - s\psi c\phi & c\psi s\theta c\phi + s\psi s\phi \\ s\psi c\theta & s\psi s\theta s\phi + c\psi c\phi & s\psi s\theta c\phi - c\psi s\phi \\ -s\theta & c\theta s\phi & c\theta c\phi \end{bmatrix} \quad (2)$$

In Eq. (2), $s\alpha$ and $c\alpha$ denote $\sin(\alpha)$ and $\cos(\alpha)$, respectively, and $\hat{C}^{(i,b)}$ is the rotation matrix between frame i to frame b . For the robotic arm, Denavit-Hartenberg parameters are shown in Table 1.

Table 1. Denavit-Hartenberg Parameters

	$k=1$	$k=2$
β_k	$-\frac{\pi}{2}$	0
θ_k	$\theta_1 + \frac{3\pi}{2}$	θ_2
b_k	b_1	b_2

Position of the quadrotor, link-1 and link-2 in the inertial-fixed reference frame can be written as:

$$\bar{p}_q^{(i)} = [x \ y \ z]^T \quad (3)$$

$$\bar{p}_1^{(i)} = \bar{p}_q^{(i)} + \hat{C}^{(i,b)} \bar{p}_1^{(b)} \quad (4)$$

$$\bar{p}_2^{(i)} = \bar{p}_q^{(i)} + \hat{C}^{(i,b)} \bar{p}_2^{(b)} \quad (5)$$

$\bar{p}_q^{(i)}$ is the position of the quadrotor with respect to inertial frame, and $\bar{p}_1^{(b)}$ and $\bar{p}_2^{(b)}$ are the positions of the link-1 and link-2 in quadrotor's body-fixed reference frame, res-

pectively.

Velocity Analysis

The linear velocities of the quadrotor, link-1 and link-2 in the inertial-fixed reference frame can be derived by taking the time derivatives of the Eq's. (3), (4), and (5).

$$\dot{\vec{p}}_q^{(i)} = [\dot{x} \ \dot{y} \ \dot{z}]^T \quad (6)$$

$$\dot{\vec{p}}_1^{(i)} = \dot{\vec{p}}_q^{(i)} + \hat{C}^{(i,b)} \vec{p}_1^{(b)} + \hat{C}^{(i,b)} \dot{\vec{p}}_1^{(b)} \quad (7)$$

$$\dot{\vec{p}}_2^{(i)} = \dot{\vec{p}}_q^{(i)} + \hat{C}^{(i,b)} \vec{p}_2^{(b)} + \hat{C}^{(i,b)} \dot{\vec{p}}_2^{(b)} \quad (8)$$

Then, linear velocities of the links are given in quadrotor body-fixed reference frame in terms of respective Jacobian matrices, \hat{J} further as:

$$\dot{\vec{p}}_1^{(b)} = \hat{J}_{v1} \dot{\vec{\Omega}} \quad (9)$$

$$\dot{\vec{p}}_2^{(b)} = \hat{J}_{v2} \dot{\vec{\Omega}} \quad (10)$$

Following that, Eq's. (7) and (8) can be further written as,

$$\dot{\vec{p}}_1^{(i)} = \dot{\vec{p}}_q^{(i)} + \hat{C}^{(i,b)} SSM(w_q^{(b)}) \vec{p}_1^{(b)} + \hat{C}^{(i,b)} \hat{J}_{v1} \dot{\vec{\Omega}} \quad (11)$$

$$\dot{\vec{p}}_2^{(i)} = \dot{\vec{p}}_q^{(i)} + \hat{C}^{(i,b)} SSM(w_q^{(b)}) \vec{p}_2^{(b)} + \hat{C}^{(i,b)} \hat{J}_{v2} \dot{\vec{\Omega}} \quad (12)$$

Where in these equations SSM is for the skew symmetric matrix operation.

Angular velocity of the quadrotor with respect to the inertial frame can be written in body-fixed and inertial-fixed reference frames, $\vec{w}_q^{(b)}$ and $\vec{w}_q^{(i)}$, respectively as:

$$\vec{w}_q^{(b)} = \hat{L} \dot{\vec{Y}} \quad (13)$$

$$\vec{w}_q^{(i)} = \hat{C}^{(i,b)} \vec{w}_q^{(b)} \quad (14)$$

$$\vec{w}_q^{(i)} = \hat{C}^{(i,b)} \hat{L} \dot{\vec{Y}} = \hat{T} \dot{\vec{Y}} \quad (15)$$

Where,

$$\hat{L} = \begin{bmatrix} 1 & 0 & -s\theta \\ 0 & c\phi & c\theta s\phi \\ 0 & -s\phi & c\theta c\phi \end{bmatrix} \quad (16)$$

Where \hat{L} is the matrix that maps the Euler angular rates to the angular velocities in the quadrotor body-fixed reference frame and maps the derivative of the Euler angles to the quadrotor's angular velocity in the inertial reference frame. Overhead dot (.) is used to represent the derivative of the corresponding variable.

The angular velocities of the links are given in the quadrotor body-fixed reference frame in terms of the Jacobian matrices as,

$$\vec{w}_1^{(b)} = \hat{J}_{w1} \dot{\vec{\Omega}} \quad (17)$$

$$\vec{w}_2^{(b)} = \hat{J}_{w2} \dot{\vec{\Omega}} \quad (18)$$

Later, the angular velocities of the links in the inertial-fixed reference frame are obtained as,

$$\vec{w}_1^{(i)} = \vec{w}_q^{(i)} + \hat{C}^{(i,b)} \hat{J}_{w1} \dot{\vec{\Omega}} \quad (19)$$

$$\vec{w}_2^{(i)} = \vec{w}_q^{(i)} + \hat{C}^{(i,b)} \hat{J}_{w2} \dot{\vec{\Omega}} \quad (20)$$

Now, let us define the generalized coordinates, and the generalized velocities of the unified system as follows,

$$\vec{q} = [x \ y \ z \ \phi \ \theta \ \psi \ \theta_1 \ \theta_2]^T \quad (21)$$

$$\dot{\vec{q}} = [\dot{x} \ \dot{y} \ \dot{z} \ \dot{\phi} \ \dot{\theta} \ \dot{\psi} \ \dot{\theta}_1 \ \dot{\theta}_2]^T$$

By using the generalized velocities, the linear and angular velocities with respect to the inertial-fixed reference frame can be written further in terms of velocity influence coefficients as [18].

$$\dot{\vec{p}}_q^{(i)} = \begin{bmatrix} \hat{I}_{3 \times 3} & \hat{0}_{3 \times 5} \end{bmatrix} \dot{\vec{q}} = \hat{V}_q \dot{\vec{q}} \quad (22)$$

$$\vec{w}_q^{(i)} = \begin{bmatrix} \hat{0}_{3 \times 3} & \hat{T} & \hat{0}_{3 \times 2} \end{bmatrix} \dot{\vec{q}} = \hat{W}_q \dot{\vec{q}} \quad (23)$$

$$\dot{\vec{p}}_1^{(i)} = \begin{bmatrix} \hat{I}_{3 \times 3} & -\hat{C}^{(i,b)} SSM(\vec{p}_1^{(b)}) \hat{L} & \hat{C}^{(i,b)} \hat{J}_{v1} \end{bmatrix} \dot{\vec{q}} = \hat{V}_1 \dot{\vec{q}} \quad (24)$$

$$\dot{\vec{p}}_2^{(i)} = \begin{bmatrix} \hat{I}_{3 \times 3} & -\hat{C}^{(i,b)} SSM(\vec{p}_2^{(b)}) \hat{L} & \hat{C}^{(i,b)} \hat{J}_{v2} \end{bmatrix} \dot{\vec{q}} = \hat{V}_2 \dot{\vec{q}} \quad (25)$$

$$\vec{w}_1^{(i)} = \begin{bmatrix} \hat{0}_{3 \times 3} & \hat{T} & \hat{C}^{(i,b)} \hat{J}_{w1} \end{bmatrix} \dot{\vec{q}} = \hat{W}_1 \dot{\vec{q}} \quad (26)$$

$$\vec{w}_2^{(i)} = \begin{bmatrix} \hat{0}_{3 \times 3} & \hat{T} & \hat{C}^{(i,b)} \hat{J}_{w2} \end{bmatrix} \dot{\vec{q}} = \hat{W}_2 \dot{\vec{q}} \quad (27)$$

In above equations, \hat{V} and \hat{W} are the linear and angular velocity influence coefficients, respectively.

Dynamics

Dynamic model of the unified quadrotor and the robotic arm is obtained by using Lagrange-d'Alembert formulation [17]. It can be written as,

$$\frac{d}{dt} \left(\frac{\partial L}{\partial \dot{\vec{q}}} \right) - \frac{\partial L}{\partial \vec{q}} = \vec{u} + \vec{u}_{ext} \quad (28)$$

$$L = K - U$$

where L is the Lagrange operator, K and U are the total kinetic and potential energies of the combined system. The terms \vec{u} and \vec{u}_{ext} are the generalized control input and the external interaction forces that are applied to end-effector, respectively.

The total kinetic energy, K is written as the summation of the kinetic energies of the each mass elements that are quadrotor mass(m_b), link-1 mass(m_1) and link-2 mass(m_2).

$$K = K_b + K_1 + K_2 \tag{29}$$

$$K_b = \frac{1}{2} \dot{p}_q^{(i)T} m_b \dot{p}_q^{(i)} + \frac{1}{2} \bar{\omega}_q^{(i)T} \hat{C}^{(i,b)} \hat{I}_b \hat{C}^{(i,b)T} \bar{\omega}_q^{(i)} \tag{30}$$

$$K_1 = \frac{1}{2} \dot{p}_1^{(i)T} m_1 \dot{p}_1^{(i)} + \frac{1}{2} \bar{\omega}_1^{(i)T} \hat{C}^{(i,b)} \hat{C}^{(b,1)} \hat{I}_1 \hat{C}^{(b,1)T} \hat{C}^{(i,b)T} \bar{\omega}_1^{(i)} \tag{31}$$

$$K_2 = \frac{1}{2} \dot{p}_2^{(i)T} m_2 \dot{p}_2^{(i)} + \frac{1}{2} \bar{\omega}_2^{(i)T} \hat{C}^{(i,b)} \hat{C}^{(b,2)} \hat{I}_2 \hat{C}^{(b,2)T} \hat{C}^{(i,b)T} \bar{\omega}_2^{(i)} \tag{32}$$

In these equations, \hat{I} is the constant inertia matrix at the corresponding reference frames of the vehicle body and the links bodies.

The total potential energy of the unified system can be expressed as,

$$U = U_b + U_1 + U_2 \tag{33}$$

$$U_b = m_b g \bar{u}_3 \bar{p}_q^{(i)} \tag{34}$$

$$U_1 = m_1 g \bar{u}_3 \bar{p}_1^{(i)} \tag{35}$$

$$U_2 = m_2 g \bar{u}_3 \bar{p}_2^{(i)} \tag{36}$$

where g is the gravity. After the Eq's. (29) and (33) are plugged into Eq. (28) the following form of the equation of motion of the unified system can be obtained as:

$$\hat{M}(\bar{q}) \ddot{\bar{q}} + \hat{C}(\bar{q}, \dot{\bar{q}}) \dot{\bar{q}} + \hat{G}(\bar{q}) = \bar{u} + \bar{u}_{ext} \tag{37}$$

where \hat{M} is positive definite and symmetric inertia matrix, \hat{C} consists of centripetal, Coriolis, gyroscopic terms, and \hat{G} consists of gravity terms.

Alternatively, to find these matrices, the following formulations are used. The total kinetic energy can be expressed in terms of the inertia matrix as [18],

$$K = \frac{1}{2} \dot{\bar{q}}^T \hat{M}(\bar{q}) \dot{\bar{q}} \tag{38}$$

By using the Eq's. (22), (23), (24), (25), (26), (27), and (38), the inertia matrix can be further written as,

$$\begin{aligned} \hat{M}(\bar{q}) = & \hat{V}_q^T m_b \hat{V}_q + \hat{W}_q^T \hat{C}^{(i,b)} \hat{I}_b \hat{C}^{(i,b)T} \hat{W}_q + \\ & \sum_{k=1}^2 \hat{V}_k^T m_k \hat{V}_k + \hat{W}_k^T (\hat{C}^{(i,b)} \hat{C}^{(b,k)}) \hat{I}_k (\hat{C}^{(i,b)} \hat{C}^{(b,k)})^T \hat{W}_k \end{aligned} \tag{39}$$

Also, the elements of the Coriolis matrix can be expressed as follows [19].

$$c_{a,b} = \sum_{j=1}^8 \frac{1}{2} \left\{ \frac{\partial m_{a,b}}{\partial q_j} + \frac{\partial m_{a,j}}{\partial q_b} - \frac{\partial m_{j,b}}{\partial q_a} \right\} \tag{40}$$

Finally, the column matrix \hat{G} can be obtained by using the total potential energy as,

$$\hat{G}(\bar{q}) = \frac{\partial U}{\partial \bar{q}} \tag{41}$$

The generalized input force, \bar{u} and the externally applied disturbance forces, \bar{u}_{ext} are obtained by using the virtual work principle method and expressed as follows.

$$\bar{u} = \hat{S} \begin{bmatrix} \bar{f}_q^{(b)} \\ \bar{\tau}_q^{(b)} \\ \bar{\tau}_{12} \end{bmatrix} = \begin{bmatrix} \hat{C}^{(i,b)} & \hat{0}_{3 \times 3} & \hat{0}_{3 \times 2} \\ \hat{0}_{3 \times 3} & \hat{I} & \hat{0}_{3 \times 2} \\ \hat{0}_{2 \times 3} & \hat{0}_{2 \times 3} & \hat{I}_{2 \times 2} \end{bmatrix} \begin{bmatrix} \bar{f}_q^{(b)} \\ \bar{\tau}_q^{(b)} \\ \bar{\tau}_{12} \end{bmatrix} \tag{42}$$

where, $\det(\hat{S}) = \cos(\theta)$

Therefore, if $\theta \neq \pi n - \frac{\pi}{2}$, $n \in Z$ then, \hat{S} is an invertible matrix. For our case, the pitch angle satisfies this condition.

$$\bar{u}_{ext} = \begin{bmatrix} \hat{I}_{3 \times 3} & \hat{0}_{3 \times 3} \\ SSM(\bar{p}_e^{(b)}) & \hat{I}_{3 \times 3} \\ \hat{J}_{ev}^T & \hat{J}_{eo}^T \end{bmatrix} \bar{P} \tag{43}$$

where the subscripts ${}^{n \times n}$ shows the size of the matrices. $\bar{p}_e^{(b)}$ is the position of the end effector in quadrotor body fixed frame. $\bar{f}_q^{(b)}$ and $\bar{\tau}_q^{(b)}$ are the forces and torques generated by the quadrotor motors, and $\bar{\tau}_{12}$ is the vector of arm's joint torques.

$$\bar{f}_q^{(b)} = [0 \quad 0 \quad f_z]^T, \quad \bar{\tau}_q^{(b)} = [\tau_{q1} \quad \tau_{q2} \quad \tau_{q3}]^T \tag{44}$$

Also, \bar{P} is the vector of the interaction force, \bar{F} and moment, \bar{M} .

$$\bar{P} = [F_1 \quad F_2 \quad F_3 \quad M_1 \quad M_2 \quad M_3]^T \tag{45}$$

In addition, the quadrotor's rotors rotational speeds, ω 's can be mapped to the generated forces and torques by the following relation.

$$\begin{bmatrix} f_z \\ \tau_{q1} \\ \tau_{q2} \\ \tau_{q3} \end{bmatrix} = \begin{bmatrix} -c_T & -c_T & -c_T & -c_T \\ 0 & -dc_T & 0 & dc_T \\ dc_T & 0 & -dc_T & 0 \\ -c_Q & c_Q & -c_Q & c_Q \end{bmatrix} \begin{bmatrix} \omega_1^2 \\ \omega_2^2 \\ \omega_3^2 \\ \omega_4^2 \end{bmatrix} \tag{46}$$

Where c_T and c_Q are the dc motors' thrust and drag coefficients, respectively. d is the distance between one dc motor and the center of mass of the quadrotor. The above relation is obtained by assuming that the square of the rotational speeds of each rotor is proportional to the generated forces and moments [1].

CONTROLLER DESIGN

The decoupled controllers are designed for the position and attitude control of the quadrotor and the angular po-

sition control of the robotic arm joints. While developing controller algorithms, the linearized decoupled equations of motion of the combined system is used. The controller architecture of the combined system is depicted in Fig. 2. The controller contains an outer and an inner loop.

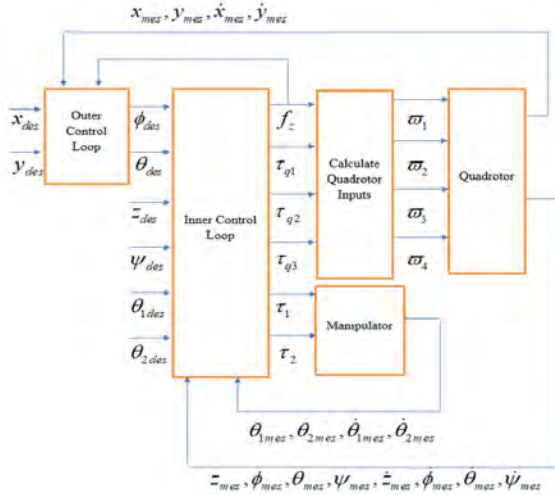


Figure 2. The controller architecture of the unified system

Outer Loop Control

Quadrotor is an underactuated vehicle that has four control inputs while having 6-DOF to be controlled. In other words, in order to have a translational motion in x-direction, the pitch angle should be changed. The same logic is valid for the translational motion in y-direction. The difference is that the roll angle should be changed. Therefore, these four states are heavily coupled with each other. To overcome this problem, an outer loop controller designed to compute the motion references for the roll and pitch angles from the reference values of the translation in x and y directions.

x and y Position Controllers

In this controller, for the desired positions in x and y, intermediate control inputs θ and ϕ are calculated and fed to the inner loop controller. To obtain control law, the following relation is written by using Eq. (42).

$$\begin{aligned} u_1 &= f_z (\cos(\psi) \sin(\theta) \cos(\phi) + \sin(\psi) \sin(\phi)) \\ u_2 &= f_z (\sin(\psi) \sin(\theta) \cos(\phi) - \cos(\psi) \sin(\phi)) \end{aligned} \quad (47)$$

By putting $\psi = 0$, Eq. (47) can be written further as for the desired roll and pitch angles as,

$$\begin{aligned} u_1 &= m\ddot{x} = f_z \theta \\ u_2 &= m\ddot{y} = -f_z \phi \end{aligned} \quad (48)$$

For Eq. (48), following control law is obtained via PID control law with feedback linearizing logic. Where e is the error between desired (des) and measured (mes) states.

$$\begin{aligned} e_x &= x_{des} - x_{mes} \\ e_y &= y_{des} - y_{mes} \end{aligned} \quad (49)$$

$$\theta_{des} = \frac{m}{f_z} (\ddot{x}_{des} + K_{px} e_x(t) + K_{ix} \int_0^t e_x(\tau) d\tau + K_{dx} \frac{de_x(t)}{dt}) \quad (50)$$

$$\phi_{des} = -\frac{m}{f_z} (\ddot{y}_{des} + K_{py} e_y(t) + K_{iy} \int_0^t e_y(\tau) d\tau + K_{dy} \frac{de_y(t)}{dt}) \quad (51)$$

Where K_p , K_i and K_d are the proportional, integral and the derivative gains of the PID controller. m is the total mass of the combined system.

Inner Loop Control

The calculated roll and pitch angles are used as reference values for the roll and pitch controllers. For yaw and altitude controllers, reference values are fed from the outside.

Altitude Controller

A PID control law is proposed by using the following relation that is obtained from Eq. (42).

$$u_3 = m\ddot{z} = f_z + mg \quad (52)$$

The control input can be calculated by using following relation.

$$f_z = m(\ddot{z}_{des} + K_{pz} e_z(t) + K_{iz} \int_0^t e_z(\tau) d\tau + K_{dz} \frac{de_z(t)}{dt}) - mg \quad (53)$$

Attitude Controller

From Eq. (42), the following relations can be written.

$$u_4 = I_{xx} \ddot{\phi} = \tau_{q1} \quad (54)$$

$$u_5 = I_{yy} \ddot{\theta} = \tau_{q2} \quad (55)$$

$$u_6 = I_{zz} \ddot{\psi} = \tau_{q3} \quad (56)$$

The attitude controllers have a cascaded structure as in Fig. 3. There is an inner loop that regulates the angular velocity and there is an outer loop that controls the angular position. Inner loop is stabilized by the PI controller and the outer loop is controlled by the P controller. The control inputs can be written as follows,

$$e_{\dot{\phi}} = \dot{\phi}_{des} - \dot{\phi}_{mes} \quad (57)$$

$$\begin{aligned} \tau_{q1} &= (K_{p2\phi} e_{\dot{\phi}}(t) - \dot{\phi}) [K_{p\phi} e_{\phi}(t) + K_{i\phi} \int_0^t e_{\phi}(\tau) d\tau] \\ \tau_{q2} &= (K_{p2\theta} e_{\dot{\theta}}(t) - \dot{\theta}) [K_{p\theta} e_{\theta}(t) + K_{i\theta} \int_0^t e_{\theta}(\tau) d\tau] \end{aligned} \quad (58)$$

$$\tau_{q3} = (K_{p2\psi} e_{\dot{\psi}}(t) - \dot{\psi}) [K_{p\psi} e_{\psi}(t) + K_{i\psi} \int_0^t e_{\psi}(\tau) d\tau]$$

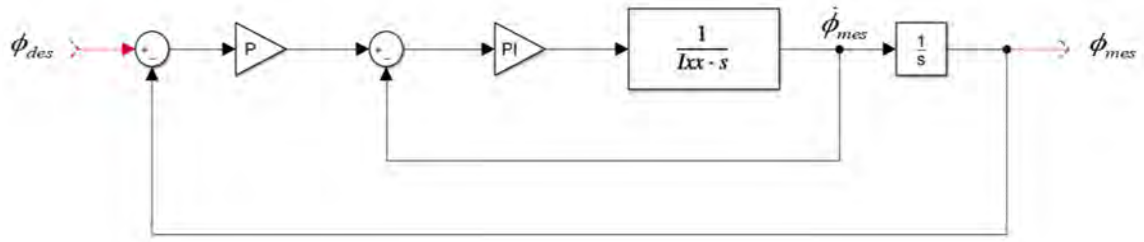


Figure 3. Roll Controller Structure

Robotic Arm Joint Angles Controller

For the joints, the following relations are used to obtain PID control laws. In these equations, I_{12} is total the inertia of the two arms about their total mass centers and I_2 is the inertia of the second link. With the small joint angle assumptions, the following relations are a good approximation for the controller design.

$$I_{12}\ddot{\theta}_1 = \tau_1 - m_{12}g \sin(\theta_1)\left(\frac{b_1 + b_2}{2}\right) \quad (59)$$

$$I_2\ddot{\theta}_2 = \tau_2 - m_2g \sin(\theta_2)\left(\frac{b_2}{2}\right) \quad (60)$$

From the above equations, by using feedback linearizing logic, the control inputs can be written as,

$$\tau_1 = I_{12}(\ddot{\theta}_{1des} + \tau_{\theta 1}) + m_{12}g \sin(\theta_1)\left(\frac{b_1 + b_2}{2}\right) \quad (61)$$

$$\tau_{\theta 1} = K_{p\theta 1}e_{\theta 1}(t) + K_{i\theta 1}\int_0^t e_{\theta 1}(\tau)d\tau + K_{d\theta 1}\frac{de_{\theta 1}(t)}{dt}$$

$$\tau_2 = I_2(\ddot{\theta}_{2des} + \tau_{\theta 2}) + m_2g \sin(\theta_2)\left(\frac{b_2}{2}\right) \quad (62)$$

$$\tau_{\theta 2} = K_{p\theta 2}e_{\theta 2}(t) + K_{i\theta 2}\int_0^t e_{\theta 2}(\tau)d\tau + K_{d\theta 2}\frac{de_{\theta 2}(t)}{dt}$$

SIMULATION RESULTS

The performance of the controllers are assessed using simulation-based analysis as detailed in this section.

Simulation Parameters and Scenario

The proposed control algorithms are tested in MATLAB/Simulink simulation environment. For the controller outputs, the saturation blocks are added to avoid unrealistic inputs to the system. The rotational speeds of the rotors are limited to the 800 rad/sec, the torque inputs of the servo motors are limited to the 3 Nm and the intermediate control inputs; phi and theta are limited to the 17 degrees. The numerical parameters of the combined system are presented in the Table 2.

Table 2. Numerical Parameters of the Combined System

m_b [kg]	2.6550	d [m]	0.3435
$m_{1,2}$ [kg]	0.1700	b_o [m]	0.3435
$I_{xx,b}$ [kgm ²]	0.0457	$b_{1,2}$ [m]	0.3000
$I_{yy,b}$ [kgm ²]	0.0457	$c_{1,2}$ [m]	0.0500
$I_{zz,b}$ [kgm ²]	0.0846	$d_{1,2}$ [m]	0.0500
$I_{xx,12}$ [kgm ²]	7.0830e-05	gravity [m/s ²]	9.8100
$I_{yy,12}$ [kgm ²]	0.0013	c_f [N/(rad/s) ²]	2.7400e-05
$I_{zz,12}$ [kgm ²]	0.0013	c_o [Nm/(rad/s) ²]	0.0470e-05

Table 3. The Gains of the Proposed Controllers

	x	y	z	ϕ	θ	ψ	θ_1	θ_2
K_p	24.790	24.790	39.430	1.959	1.959	1.269	1325	4669
K_i	12.360	12.360	27.880	20.880	20.880	4.390	6169	40370
K_d	9.407	9.407	12.170	-	-	-	70.450	129.800
K_{p2}	-	-	-	9.172	9.172	3.339	-	-

Table 4. The Reference Values of the Controlled Variables

Time [s]	0-9	10-19	25-30	30-60
x [m]	0-5	5	5	5
y [m]	0-3	3	3	3
z [m]	-	-2	-2	-2
ϕ [deg]	-	-	-	-
θ [deg]	0-(-5)	-	-	-
ψ [deg]	0	-5	-5	-5
θ_1 [deg]	0	0-15	15	15
θ_2 [deg]	0	0-10	10	10
F_1 [N]	0	0	0-5	5
F_2 [N]	0	0	0-2	2
F_3 [N]	0	0	0-6	6

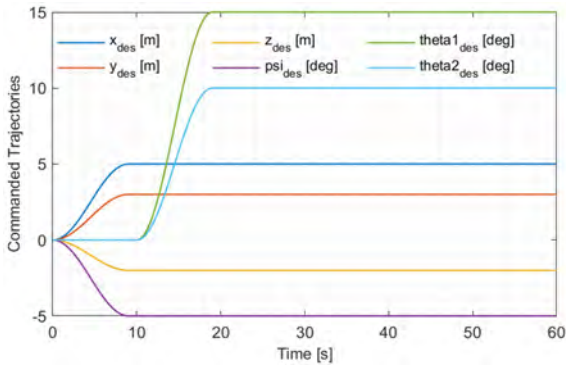


Figure 4. The Desired Values of the Directly Controlled Parameters

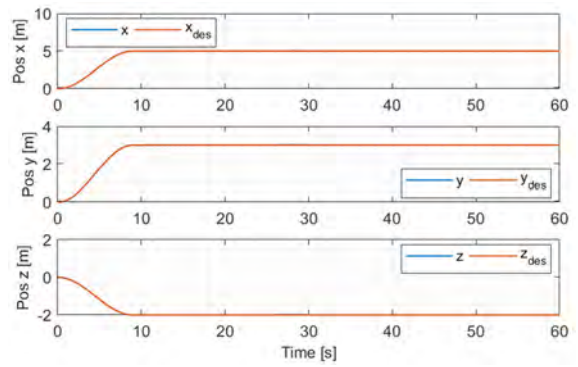


Figure 6. The Desired and Achieved Cartesian Position of the Quadrotor

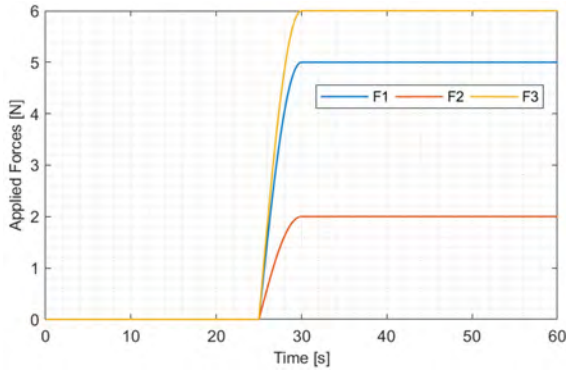


Figure 5. The Applied Disturbance Forces

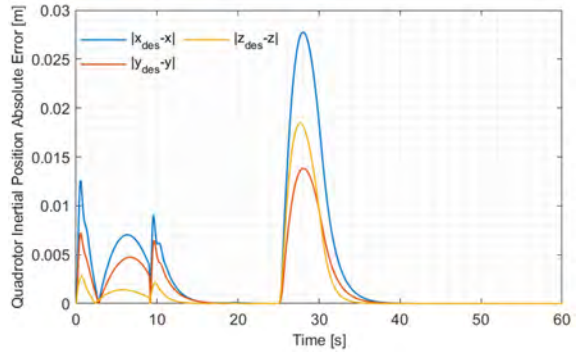


Figure 7. The Absolute Error Between Desired and Achieved Inertial Position of the Quadrotor

The gains of the designed controllers are given in Table 3. These gains are obtained by using the root locus method of the classical control theory.

The proposed controllers are tested with a simulation scenario. This scenario is shown in Table 4 and Fig. 4.

Firstly, the quadrotor is commanded to move to the predefined positions (5 m in x, 3 m in y, and -2 m in z) and yaw angle joint angles of the robotic arm are kept at 0. Then, the robotic arm is moved to the predefined angles (15 degree in θ_1 and 10 degree in θ_2). Finally, the disturbance forces are applied to the end-effector of the serial manipulator (6 N in +x-direction, 2 N in +y-direction and 6 N in +z-direction).

Quadrotor Position Control

The performance of the position controller is evaluated and the response of the aerial manipulator in the inertial reference frame is depicted in Fig. 6 and Fig. 7.

Although the robotic arm is active and external disturbances are applied to the system, the quadrotor tracked the input well (Fig. 6) and the maximum absolute error is less than 0.03 m during the course of the motion (Fig. 7).

Quadrotor Attitude Control

Due to the underactuated nature of the quadrotors, the

attitude dynamics of quadrotors is manipulated to move the quadrotor to a desired position. Fig. 8 and Fig. 9 present the reference and actual values of the Euler angles during the position control in Section 4.2. Fig. 10 shows the corresponding absolute error due to the difference between the desired and achieved values.

Due to the underactuated nature of the system, the performance of the attitude control system is effective in the performance of position control. The quadrotor tracks the desired attitude values well (Fig. 8). During the transient period, the maximum error is around -4 degrees in theta and 2 degrees in phi (Fig. 9). The maximum absolute error is almost 1.2 degrees in theta (Fig. 10).

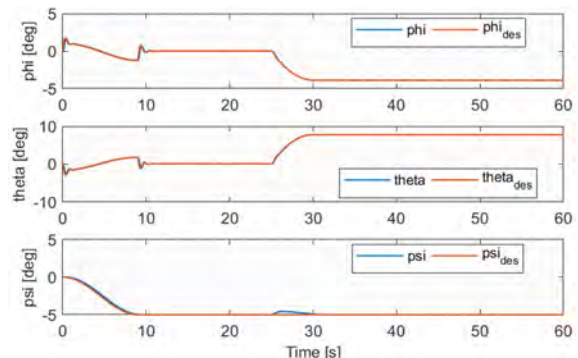


Figure 8. The Desired and Achieved Attitude of the Quadrotor

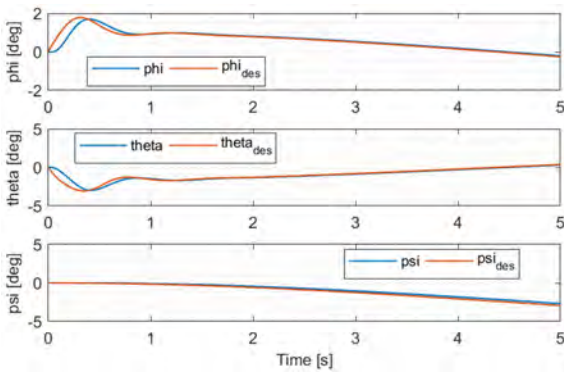


Figure 9. The Zoomed Version of the Desired and Achieved Attitude of the Quadrotor

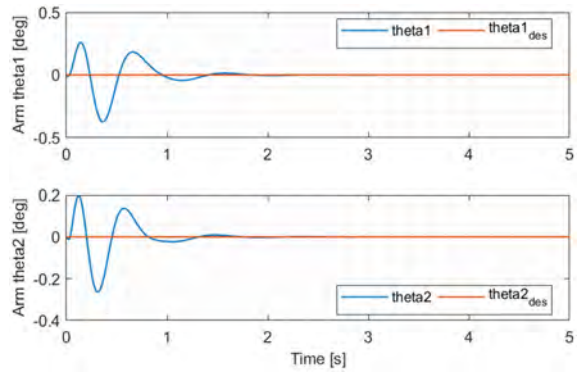


Figure 12. The Zoomed Version of the Desired and Achieved Joint Angles of the Robotic Arm

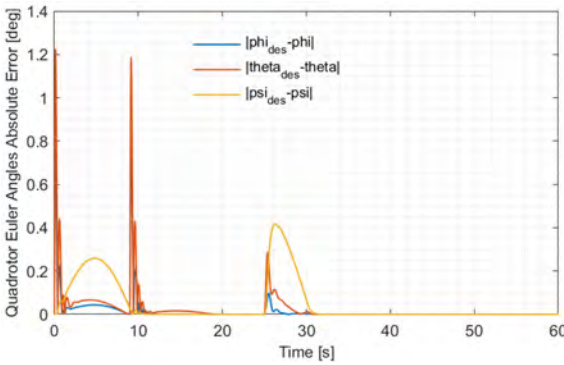


Figure 10. The Absolute Error Between the Desired and Achieved Attitude of the Quadrotor

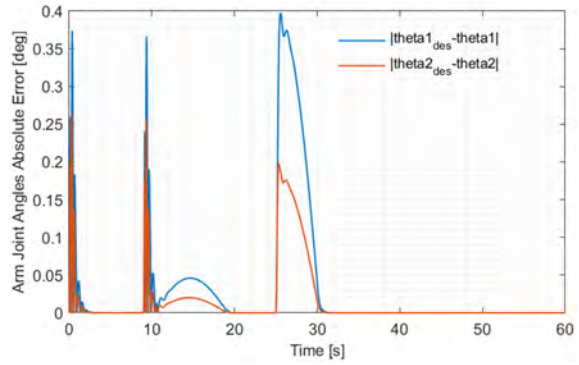


Figure 13. The Absolute Error Between the Desired and Achieved Joint Angles of the Robotic Arm

Robotic Arm Joint Angles Control

The coupled arm is controlled during the position control experiment. The reference and actual values of the joint angles is depicted in Fig. 11 and its zoomed version is depicted in Fig. 12. Fig. 13 shows the corresponding absolute error due to the difference in the reference and the actual values.

The robotic arm tracked the desired angles well both in the steady state (Fig. 11) and transient (Fig. 12) periods. The maximum absolute error in both axes is less than 0.5 degrees (Fig. 13).

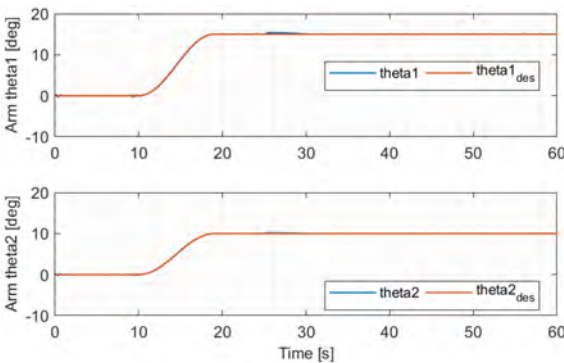


Figure 11. The Desired and Achieved Joint Angles of the Robotic Arm

DISCUSSION AND CONCLUSION

In this paper, decoupled controllers are proposed for an aerial manipulation system composed of a quadrotor and a serial 2-DOF robotic arm. First, for the position of the quadrotor and joint angles, decoupled PID controllers are designed by using feedback linearization technique. Then, cascaded PID controllers are proposed for the attitude dynamics of the quadrotor. Here, reference values of the roll and pitch angle of the quadrotor are the output of the position controllers of the x and y. Designed controllers are tested in a simulation environment with highly nonlinear dynamic models.

At first, nonzero cartesian positions and yaw angle are commanded to the quadrotor. The aerial manipulator reaches these reference trajectories in 9 seconds. Due to the transient and coupled dynamics of the system, there are some oscillations. However, these oscillations are suppressed with the action of the controllers (Figs. 6, 7 and 8). Also, there are some small deviations from the zero reference values of the joint angles as shown in Figs. 11, 12 and 13. This is caused by the faster pitch dynamics of the quadrotor and the transient dynamics of the system. These oscillations are controlled by the joint controllers. Then, at 10 seconds, the serial manipulator is commanded to track the reference values. The joint controllers track these references successfully.

The quadrotor is affected from this action slightly, but it is suppressed by position controllers. Finally, the disturbance forces are applied to the end-effector of the serial manipulator at 25 seconds as shown in Fig. 5. The quadrotor deviates from its original position, but it comes to the reference position very fast with the action of the controllers. The attitude controllers tilt the quadrotor to balance these multi-directional forces as illustrated. Thus, it has nonzero roll and pitch angles as illustrated in Fig. 9 after the disturbance forces are applied. The joint controllers deal with these disturbances very effectively.

To sum up, the controllers' performances are tested with the coupled reference commands and disturbance forces. The performance of the controllers is found to be satisfactory.

As a future work, the sensor models of the accelerometer, gyro, and the indoor localization system will be implemented into simulation environment. Then, the gains of the controllers will be updated. Finally, we plan to implement the developed controller algorithms in a real system.

References

1. Kotarski, Denis, Zoran Beni, and Matija Krznar. Control design for unmanned aerial vehicles with four rotors. *Interdisciplinary Description of Complex Systems: INDECS 14.2* (2016) 236–245.
2. Das, Abhijit, Kamesh Subbarao, and Frank Lewis. Dynamic inversion with zero-dynamics stabilisation for quadrotor control. *IET Control Theory and Applications* 3.3 (2009) 303–314.
3. Sadr, Sara, S. Ali A. Moosavian, and Payam Zarafshan. Dynamics modeling and control of a quadrotor with swing load. *Journal of Robotics* 2014 (2014) 1–12.
4. Mahony, Robert, Vijay Kumar, and Peter Corke. Multirotor aerial vehicles: Modeling, estimation, and control of quadrotor. *IEEE Robotics and Automation Magazine* 19.3 (2012) 20–32.
5. Goodarzi FA, Lee D, Lee T. Geometric stabilization of a quadrotor UAV with a payload connected by flexible cable. In *2014 American Control Conference*, pp. 4925–4930, 2014.
6. Sreenath K, Kumar V. Dynamics, control and planning for cooperative manipulation of payloads suspended by cables from multiple quadrotor robots. In *Robotics: Science and Systems IX*, 2013.
7. Alothman, Y., Guo, M., & Gu, D. Using iterative LQR to control two quadrotors transporting a cable-suspended load. *IFAC-PapersOnLine* 50.1 (2017) 4324–4329.
8. Kim S, Choi S, Kim HJ. Aerial manipulation using a quadrotor with a two DOF robotic arm. In *2013 IEEE/RSJ International Conference on Intelligent Robots and Systems*, pp. 4990–4995. 2013.
9. Caccavale, F., Giglio, G., Muscio, G., & Pierri, F. Adaptive control for UAVs equipped with a robotic arm. *IFAC Proceedings Volumes* 47.3 (2014) 11049–11054.
10. Jimenez-Cano A, Martin J, Heredia G, Ollero A, Cano R. Control of an aerial robot with multi-link arm for assembly tasks. In *2013 IEEE International Conference on Robotics and Automation*, pp. 4916–4921, 2013.
11. Danko TW, Chaney KP, Oh PY. A parallel manipulator for mobile manipulating UAVs. In *2015 IEEE International Conference on Technologies for Practical Robot Applications (TePRA)*, pp. 1–6, 2015.
12. Orsag M, Korpela C, Bogdan S, Oh P. Lyapunov based model reference adaptive control for aerial manipulation. In *2013 International Conference on Unmanned Aircraft Systems (ICUAS)*, pp. 966–973, 2013.
13. Khalifa A, Fanni M. A new quadrotor manipulation system: Modeling and point-to-point task space control. *International Journal of Control, Automation and Systems* 15.3 (2017) 1434–46.
14. Giglio G, Pierri F. Selective compliance control for an unmanned aerial vehicle with a robotic arm. In *22nd Mediterranean Conference on Control and Automation*, pp. 1190–1195, 2014.
15. Mello LS, Raffo GV, Adorno BV. Robust whole-body control of an unmanned aerial manipulator. In *2016 European Control Conference (ECC)*, pp. 702–707, 2016.
16. Garimella G, Kobilarov M. Towards model-predictive control for aerial pick-and-place. In *2015 IEEE International Conference on Robotics and Automation (ICRA)*, pp. 4692–4697, 2015.
17. Bulut, N., Turgut, A. E., & Arıkan, K. B. (2019). Computed Torque Control of an Aerial Manipulation System with a Quadrotor and a 2-DOF Robotic Arm. In *2019 International Conference on Informatics in Control, Automation and Robotics (ICINCO)*, 2019.
18. Ozgoren, M. K. *Lecture Notes for ME 522 (Principles of Robotics)*, Department of Mechanical Engineering, METU, Ankara, 2017.
19. Siciliano B, Sciavicco L, Villani L, Oriolo G. *Robotics: Modelling, planning and control*, Springer, London, 2010.

Probiotic Properties of some *Lactobacillus* spp. that can survive in the Presence of Viral Gastroenteritis

Elmas Ceren Ikiz¹, Gulcin Alp Avci¹ , Hande Alp² 

¹Hitit University, Department of Molecular Biology and Genetics, Çorum, Turkey

²Child Allergy Specialist, Remzi Oguz Arik Neighborhood, Kavaklıdere Street, 23/2, Ankara, Turkey

ABSTRACT

Viral acute gastroenteritis is a serious health problem worldwide with the high morbidity and mortality rates. In fact there is no available antiviral treatment for gastroenteritis alternatively, the use of probiotics on which have numerous benefits, has been on the increase recently. Therefore, to be able to identify the strains that can survive in viral acute gastroenteritis and their distinguishable features, seven strains of *Lactobacillus* spp. were isolated from the stool samples of 0-5 year old children with viral gastroenteritis in this study. Strains were identified by API 50 CH test. EPS production capacities, acid resistance, bile tolerance, antibiotic susceptibilities, and antimicrobial activities against *Escherichia coli* ATCC 25922 were determined in the order to investigate their probiotic features. Strains were characterized as *Lactobacillus plantarum*. All strains survived in De Man Rogosa and Sharpe (MRS) broth with adjusted pH values of 2 and 3, despite high inhibition rates (95.2-99.2% and 98.3-99.2%, respectively). Furthermore, all strains maintained their viability within MRS broth mediums that contain 0.15%, 0.2% and 0.3% bile (viability rates as 81.4-92.5%, 80.9-87.3% and 73.2-89.2%, respectively). *Exopolysaccharide* production (4.13-50.33 mg/mL) was observed in all strains except for 182a. No antimicrobial activity was detected against *E. coli* ATCC 25922. All strains experienced high sensitivity to erythromycin while showing resistance to vancomycin. In conclusion, *L. plantarum* strains obtained in this study can be further investigated for describe other probiotic features and may be used for the production of new probiotic products to provide sufficient therapies in further studies.

Keywords:

Acute Gastroenteritis, Probiotics, *Lactobacillus* spp.

INTRODUCTION

Gastroenteritis which can affect all age groups, especially children under the age of 5, is an important health problem in both developed and developing countries worldwide with high mortality rate, causing socioeconomic burden [1, 2]. It can be classified as acute, dysenteric or chronic. Acute gastroenteritis causing major outbreaks by viral, parasitic or bacterial agents has high morbidity and mortality all over the world as well as in Turkey. The most common etiologic factor of acute gastroenteritis is viral agents. Millions of diarrhea attacks and outpatient examinations are observing worldwide due to the viral gastroenteritis, and worse, more than 2 million children are hospitalized each year [1, 3]. In the lead of rotaviruses, viral gastroenteritis can also caused by different viral agents that include norovirus, adenovirus, bocavirus, sapovirus and astrovirus [4]. In viral gastroenteritis, fecal-orally transmitted virus particles cross over the gastrointestinal tract and bind

to intestinal epithelium and cause inflammation in epithelial cells. As a result of inflammation-causing villous atrophy and mucosal damage, absorption of nutrients and fluids is impaired and the accumulated substances are excreted with severe diarrhea. In addition to diarrhea, acute gastroenteritis with fever, vomiting, nausea and abdominal pain lasts 1-2 weeks and causes significant loss of fluid [3, 4]. In order to overcome these diseases, especially in children's units, schools, elderly care centers, social areas and at home, hygienic cautions, carefully washing of the nutrients, well-balanced diet and vaccines are recommended. There is no available vaccine produced against rotavirus and other viral agents, except Rotarix and Rotateq in which United States has been using as therapeutics [2]. Viral gastroenteritis is a self-limiting disease with no effective antiviral drug treatment in use. The main treatment is to provide recovery of lost fluid and electrolytes. To restore intestinal flora

Article History:

Received: 2019/08/21

Accepted: 2019/12/15

Online: 2019/12/31

Correspondence to: Elmas Ceren Ikiz,
Hitit University, Department of Molecular
Biology and Genetics
Tel: +90 364 227 7000
Fax: +90 364 227 7005
E-Mail:ceren_kesepara@hotmail.com

balance, recent studies have focused on dietary supplementation of probiotics that have many health-beneficial effects, such as cancer prevention, immune system regulation, assistance to lactose digestion, regulation of intestinal flora, heart disease prevention, and lowering serum cholesterol levels [1, 5, 6]. Because of breast milk is the main source of probiotic and prebiotic nutrition, it is recommended that, breastfeeding should be more often for the homeostasis of intestine and meals per day of babies fed by supplementary food rather than mother's milk should be increased. Several probiotics such as *Bifidobacterium bifidum*, *Streptococcus thermophilus*, *Lactobacillus reuteri*, *Lactobacillus casei* and *Lactobacillus rhamnosus* (GG origin) have been reported to be useful in gastroenteritis diarrhea [7, 8], however, those are still limited. We hypothesize that probiotic bacteria are able to survive and maintain colonization, possibly by developing new features or improving already existed ones under all stress conditions mentioned above caused by viral acute gastroenteritis. This is a new insight of our study revealed because in literature most of researchers have based their study on the strains isolated from healthy individuals and fermented products. Therefore, the first objective of this study was to isolate lactobacilli that could survive in the presence of viral acute gastroenteritis agents. The second aim of this study was to determine some probiotic properties of these lactobacilli. Strains obtained from this study may be use in future research with purpose of developing new probiotic products or using as supplements in nutritional therapies.

MATERIAL AND METHODS

Isolation and Identification of Bacteria

In our study, 51 stool samples previously determined as rotavirus positive (18), adenovirus positive (17), adenovirus/rotavirus positive (2) and negative (14) by ELISA method were used. Lactobacilli strains were isolated by culture method from 10% Phosphate-Buffered Saline (PBS, pH:7.4) diluted stool samples. For isolation, incubation was provided in MRS Broth (Merck, Darmstadt, Germany) and MRS-Agar mediums (pH 6.8 ± 0.02) at 37°C for 18-24 hours in an anaerobic environment. MRS-Agar mediums were prepared by adding 1.5% Agar-agar (Merck, Darmstadt, Germany). Anaerobic environment was obtained by Anaerocult® C (Merck, Darmstadt, Germany) kit. The strains were stored in 60% glycerol at -80°C.

Classical and biochemical identification methods were used for *Lactobacillus* strains. Colony morphology of bacteria was observed and their microscopic morphology and response to gram staining were examined. API® 50 CH / CHL (API System, Bio-Merieux, France) tests were applied for the identification of biochemical bacteria.

Determination of Some Probiotic Properties

Exopolysaccharide Production of Isolates

The method obtained from literature is used for EPS production [9]. In spectrophotometer with 600 nm wavelength, the Optical Density 600nm values of active *Lactobacillus* strains were adjusted to 0.600. Strains ($OD_{600} \sim 0,600$) were inoculated in new MRS medium at 2% rate and incubated at 37 ° C in the anaerobic environment for 24 hours. After 24 hours, each 1 mL of active cultures was boiled in sterile eppendorf tubes at 96 ° C for 10-15 minutes and allowed to cool. Samples were centrifuged at 13000 rpm for 25 min with an addition of 170 µl 85% Trichloroacetic acid (Merck, Darmstadt, Germany). The supernatants were again centrifuged by adding an equal volume of ethanol in the new sterile eppendorf tubes. For the second time, ethanol was added onto the pellets, then, dissolved and centrifuged again to precipitate. Precipitated samples were dissolved in 1 mL dH₂O and the amount of EPS was determined using phenol-sulfuric acid method [10]. To determine the amount of EPS production, the standard curve was extracted using glucose solutions ranging from 5 to 100 mg/L.

Tolerance to Acid and Bile of Isolates

In order to determine the reproduction rate of lactobacilli in acidic medium, MRS media were prepared as pH 2.0, pH 3.0, pH 6.8 (control) and pH 8.0. Mediums' pHs have adjusted by pH meter (with 1 N NaOH and 1 N HCl). All strains were activated twice before experiment to obtain cultures in logarithmic phase. Twice activated *Lactobacillus* spp. strains were incubated in the MRS medium with different pHs at 37°C in anaerobic media for 24 hours. After 24 hours, the density of the cultures was measured by spectrophotometer set to a wavelength of 600 nm.

To characterize the resistance of isolated strains to bile; MRS media containing 0% (control), 0.15%, 0.2% and 0.3% bile salt was prepared and twice activated *Lactobacillus* spp. were inoculated in these media ($OD_{600} = 0.600$), after incubation at 37°C in anaerobic media for 24 hours, the intensity of cultures was measured by spectrophotometer (600 nm).

Resistance to Antibiotics of Isolates

Disc diffusion method was preferred to analyze whether strain resists to antibiotics. Twice activated *Lactobacillus* spp. cultures' OD values at 600 nm were adjusted to 0.600. Each 100 µl amount of cultures was inoculated upon Muller-Hinton Agar medium, and then, antibiotic discs (penicillin G, vancomycin, chloramphenicol, azithromycin, tetracycline, ampicillin, gentamicin, clindamycin, erythromycin, amikacin) were placed. The diameters of the inhibition zones formed after 24 hours of the anaerobic incubation at 37°C were measured.

Antimicrobial Activity against *E. coli* ATCC 25922 of Isolates

Disc diffusion method was used to determine the antimicrobial activity of the strains. Twice activated *Lactobacillus* spp. strains and *E. coli* ATCC 25922 cultures' OD values at 600 nm were set to 0.600. 100 µl of *E. coli* culture were inoculated upon Muller-Hinton Agar media (Merck, Darmstadt, Germany), and sterile discs that prepared from Watmann No: 4 filter papers were placed. 5 µl, 10 µl and 15 µl of *Lactobacillus* spp. strains were added onto the prepared sterilized discs, and petri dishes were incubated at 37°C for 24 hours in anaerobic media. After 24 hours, the inhibition zone diameters were measured.

Statistical Analysis

In all studies, the mean values of two different parallels are given. SPSS 20.0 (SPSS Inc., Chicago) program was used for statistical analysis. According to the one-way ANOVA correlation, the relationships between EPS production and resistance to different pHs as well as EPS production and bile tolerance were investigated.

RESULTS

Isolation and Identification of Bacteria

The seven *Lactobacillus* spp. were isolated from 51 stool samples. One (66a) of these strains was isolated from viral negative patient, and the rest (87a, 87b, 182a, 182b, 183a and 209a) was isolated from rotavirus positive samples. *Lactobacillus* spp. strains could not be isolated from adenovirus positive samples. Microscopic and colony morphologies of isolated strains are shown in the Fig. 1.



Figure 1. Microscopic image and colony morphology of *Lactobacillus* strains



Figure 2. API test results (from left to the right ; after 0 h, 24 h and 48 h) ; Yellow color was described as positive result, purple color as negative result and intermediate color as pseudo positive result.

Table 1. API 50 CH identification test results of isolates.

Strains codes	API results (% Identification rates)
66a	<i>L. plantarum</i> (99,9%)
87a	<i>L. plantarum</i> (99,8%)
87b	<i>L. plantarum</i> (98,9%)
182a	<i>L. plantarum</i> (99,9%)
182b	<i>L. plantarum</i> (99,9%)
183a	<i>L. plantarum</i> (99,9%)
209a	<i>L. plantarum</i> (99,3%)

API 50 CH identification test results of the 7 *Lactobacillus* strains are given in Fig. 2 and Table 1.

Determination of Some Probiotic Properties

Exopolysaccharide Production of Isolates

The EPS production of the samples is given in Table 2. The strain showing the highest EPS production in *L. plantarum* 182b strain, but EPS production was not detected in the 182a strain. EPS production capacity determination studies for isolated and identified strains were performed in two different time intervals. Due to the variable results in measurements, statistically standard deviation could not be calculated.

Table 2. The Exopolysaccharide production amount of isolated strains

Strain Codes	EPS Production (mg/L)
<i>L. plantarum</i> 66a	5.54
<i>L. plantarum</i> 87a	9.17
<i>L. plantarum</i> 87b	7.93
<i>L. plantarum</i> 182a	ND
<i>L. plantarum</i> 182b	50.33
<i>L. plantarum</i> 183a	4.13
<i>L. plantarum</i> 209a	9.01
<i>L. plantarum</i> DSM 20174*	132.0

*: *L. plantarum* DSM 20174; Reference strain

Tolerance to Acid and Bile of Isolates

The viability measurements of seven strains in MRS media adjusted pH 2.0, pH 3.0, pH 6.8 (control) and pH 8.0 are shown in Table 3. It was indicated that seven *L. plantarum* strains were also active at pH 2.0 according to the viability measurements in different acidic environments.

In medium without bile and with 0.15%, 0.2% and 0.3% bile, viability measurements for seven strains are given in Table 4. As a result of bile tolerance measurement, seven strains experienced less growth in the media with bile than control. The strains that possessed the highest and lowest bile tolerance were characterized as 66a and 209a, respectively.

Table 3. Acid resistance of isolated strains in different pHs

Strain Codes	Acid resistance			
	pH 2.0	pH 3.0	pH 6.8 ^a	pH 8.0
<i>L. plantarum</i> 66a	0.11 ± 0.08	0.02 ± 0.01	2.33 ± 0.00	2.25 ± 0.01
<i>L. plantarum</i> 87a	0.07 ± 0.11	0.04 ± 0.00	2.33 ± 0.08	2.27 ± 0.20
<i>L. plantarum</i> 87b	0.03 ± 0.01	0.03 ± 0.01	2.33 ± 0.36	2.81 ± 0.03
<i>L. plantarum</i> 182a	0.02 ± 0.01	0.02 ± 0.01	2.44 ± 0.17	2.41 ± 0.06
<i>L. plantarum</i> 182b	0.04 ± 0.01	0.02 ± 0.01	2.50 ± 0.03	1.25 ± 0.04
<i>L. plantarum</i> 183a	0.04 ± 0.01	0.04 ± 0.01	2.46 ± 0.02	2.53 ± 0.02
<i>L. plantarum</i> 209a	0.02 ± 0.00	0.03 ± 0.02	2.22 ± 0.02	2.26 ± 0.10
<i>L. plantarum</i> DSM 20174 ^b	0.24 ± 0.20	0.38 ± 0.10	3.52 ± 0.50	3.46 ± 0.34

pH 6.8^a: Control medium*L. plantarum* DSM 20174^b: Reference strain**Table 4.** Viability measurements of isolated strains in different bile concentration

Strain Codes	Bile tolerance			
	0% ^a	0.15%	0.20%	0.30%
<i>L. plantarum</i> 66a	2.33 ± 0.00	2.04 ± 0.04	2.04 ± 0.02	2.09 ± 0.08
<i>L. plantarum</i> 87a	2.33 ± 0.08	1.97 ± 0.05	1.96 ± 0.01	1.96 ± 0.10
<i>L. plantarum</i> 87b	2.33 ± 0.36	1.89 ± 0.01	1.93 ± 0.01	1.99 ± 0.07
<i>L. plantarum</i> 182a	2.44 ± 0.17	2.02 ± 0.00	2.01 ± 0.01	1.86 ± 0.26
<i>L. plantarum</i> 182b	2.50 ± 0.03	2.07 ± 0.17	2.02 ± 0.05	2.15 ± 0.10
<i>L. plantarum</i> 183a	2.46 ± 0.02	2.04 ± 0.03	2.01 ± 0.08	1.85 ± 0.06
<i>L. plantarum</i> 209a	2.22 ± 0.02	2.06 ± 0.05	1.86 ± 0.01	1.63 ± 0.03
<i>L. plantarum</i> DSM 20174 ^b	3.52 ± 0.50	3.82 ± 0.10	3.18 ± 0.05	1.02 ± 0.02

^a: bile free^b: Reference Strain

Resistance to Antibiotics of Isolates

Seven isolated strains of *L. plantarum* were resistant to vancomycin. While the strain 87a was also showing resistance to tetracycline; the strain 87b experienced resistance to penicillin and tetracycline. The strains 182a and 209a showed resistance to penicillin beside vancomycin. Overall, all strains presented susceptibility to clindamycin, azithromycin, ampicillin, gentamicin, erythromycin and chloramphenicol. The highest sensitivity of all strains was measured for erythromycin. The most resistant strains against 10 antibiotics measured were strains 87a and 87b. The least resistant strains were the 182a and 182b strains. Inhibition zone measurements are given in Table 5.

Antimicrobial Activity against *E. coli* ATCC 25922 of isolates

The antimicrobial effect on *E. coli* ATCC 25922 was not observed in three different concentrations (5 µl, 10 µl and 15 µl) of seven *L. plantarum* strains.

DISCUSSION

The formation of intestinal microbiota begins with birth.

The population of microorganisms in the baby's intestine reaches up to 10⁹-10¹⁰ of bacteria rising from the environment of contact with such as doctors, mother and other individuals, mother's milk and nutrients in the first days of post-natal [11, 12]. The imbalances in dietary habits, drug use and diseases lead to the change of natural intestinal microbiota in humans, and thus, to an imbalance in the nutrient absorption and dehydration. An important factor in the change of intestinal flora is acute gastroenteritis (AGE) infections in the early stages of life [13-15].

As one from the negative patient and six from the rotavirus positive patients, seven gram (+) bacilli strains were isolated. No isolation from adenovirus positive samples could be obtained. It is thought that cell lysis caused by adenoviruses is an important obstacle in adhesion of bacteria. Thus, the survival rates of not adhesive bacteria are decreased significantly.

The classical identification methods and API 50 CHL test results revealed that 7 of these strains belonged to the *Lactobacillus plantarum* strains. Most of the studies have been based on the isolation of probiotic bacteria from healthy individuals [16-18]. In our study, unlike literature, probiotic strains that can sustain their viability despite the changing conditions and inflammation were isolated from patients with AGE. Therefore in the literature, species diversity is higher in isolation and isolation success has been higher. This arises from the increasingly difficulties in bacterial colonization due to epithelial damage, as well as the excretion of bacteria with excrement due to diarrhea [16-18].

In order to overtake the gastrointestinal tract and colonize the intestine when taken orally; the probiotics need to survive in the acidic environment of the stomach, in the high bile concentration of the intestine, and in the presence of a wide variety of pathogens [19, 20]. For this purpose, in vitro imitations of these conditions were prepared and acid resistance and bile tolerance of isolated strains were investigated.

All isolates were determined to have high inhibition at pH 2.0, but they were able to maintain their viability. Strains' rate of decrease at pH 2.0 compared with pH 6.8 (control) varied between 95.2% and 99.2%. The decrease rate of strains at pH 3.2 according to the control ranged from 98.3% to 99.2%. The strain with the highest tolerance to the acidic medium was determined as *L. plantarum* 66a while the lowest tolerance was characterized as *L. plantarum* 182a. In the literature, lactobacilli strains with high inhibition in acidic environment have been reported [18, 21-24], and particularly in one study researchers concluded that the strains could not maintain their viability in the acidic environment [18]. In our study, despite the presence of AGE, all strains

Table 5. Antibiogram test results of strains (mm zone diameter)

Strain Codes	Bile tolerance									
	DA ^a	AZM ^b	P ^c	AMP ^d	AK ^e	C ^f	E ^g	TE ^h	CN ⁱ	VA ^k
<i>L. plantarum</i> 66a	25.0±0.0	28.4±1.2	15.6±0.2	22.4±0.5	15.0±0.0	24.0±0.3	22.3±1.1	12.6±1.6	17.4±1.6	NIZ ^m
<i>L. plantarum</i> 87a	17.9±0.2	20.6±0.5	13.2±0.2	20.8±1.1	17.3±1.1	18.8±0.7	22.0±0.0	NIZ	14.9±0.2	NIZ
<i>L. plantarum</i> 87b	17.4±0.5	20.1±2.6	NIZ	23.4±0.6	15.0±1.4	21.3±1.7	29.5±1.1	NIZ	20.3±0.3	NIZ
<i>L. plantarum</i> 182a	16.0±0.0	27.6±4.4	NIZ	21.5±1.2	22.6±1.6	24.1±0.2	27.0±0.0	12.9±1.9	23.9±1.6	NIZ
<i>L. plantarum</i> 182b	20.2±1.1	26.3±1.8	13.4±0.7	14.8±0.7	24.1±1.6	28.0±1.1	31.1±0.6	14.8±3.9	21.4±0.5	NIZ
<i>L. plantarum</i> 183a	20.0±0.7	25.5±0.3	12.7±1.8	20.4±0.5	17.8±1.1	15.5±0.0	24.1±0.2	12.7±0.1	17.1±0.9	NIZ
<i>L. plantarum</i> 209a	14.1±0.8	15.9±1.2	NIZ	22.4±0.9	18.6±0.5	21.4±0.7	26.5±1.4	10.0±0.0	20.6±1.1	NIZ

DA^a: Clindamycin (2 µg), AZM^b: Azithromycin (15 µg), P^c: Penicillin (10 µg), AMP^d: Ampicillin (10 µg), AK^e: Amikacin (30 µg), C^f: Gentamicin (30 µg), E^g: Erythromycin (15 µg), TE^h: Tetracycline (30 µg), CNⁱ: Chloramphenicol (10 µg), VA^k: Vancomycin (30 µg), NIZ^m: No inhibition zone

were able to maintain their presence in low acidity.

The viability of strains decreased as the concentration of bile increased. The decrease rate of cultures in 0.3% bile concentration was compared with the control with no bile varied between 10.2% and 26.8%. The strain with the highest tolerance was determined as *L. plantarum* 66a when the strain with the lowest tolerance was determined as *L. plantarum* 209a. In some studies investigating the resistance of lactobacilli strains isolated from healthy babies to high bile salt concentrations, a high rate of inhibition was reported in the 0.3% concentration of bile salt [18, 21-26]. The viability of *L. plantarum* strains examined in our study has decreased, parallel to the most studies in the literature.

Exopolysaccharides are structures those are produced by the bacterium, which are found in the cell wall and bind the bacteria to the cell. These saccharides protect the cells against antibiotics and toxic substances, support immunity, and thus have antitumoral and cholesterol-lowering activity [27, 28]. The probiotic bacteria have an importance, for the colonization race with pathogen ones and, are capable of producing EPS which is physically protective and enhance the adhesion to the intestine. Therefore, it is highly preferred for a probiotic bacterium that the high EPS production capacity. In this study, EPS production capacities of isolated 7 strains were investigated and EPS production was measured in all strains except *L. plantarum* 182a. The EPS values measured in the rest 6 *L. plantarum* strains ranged from 4.13 to 50.33 mg/mL. Some of researchers reported that the range of EPS production of probiotic strains isolated from fermented products and human feces was 102-263 mg/L [29]; while others noted this range for kefir bacteria as 173-378 mg/L [21]. Furthermore, in another study the EPS production range of lactic acid bacteria isolated from children feces age of 4-15 years have reported as 70-290 mg/L [18] and different researchers having investigated the probiotic properties of *Lactobacillus* strains found the range of EPS production as 62-287 mg/L [30]. In our study with compared to the literature, six of the *L. plantarum* strains showed low EPS production, while one showed no production. We claimed that

the differences between the each measurement might be due to the source of the strains, the incubation conditions and the medium content. In our study, although the strains were isolated from an important infection condition called viral acute gastroenteritis, they were able to maintain their EPS production capability and the vitality in the intestine, even if there is a smaller amount of EPS production.

Since the study of replica within each group may potentially affect the significance of statistical analysis. There was no significant relationship between the EPS production of the strains and their resistance in acidic environments ($p>0.05$). There was no significant correlation between EPS production of strains and tolerance to different bile concentrations too ($p>0.05$). This was thought to be due to fluctuations in EPS production capacity. Statistically, there was a positive correlation between the acid resistance and the bile tolerance of the strains when resistance and tolerance of the strains were evaluated together ($p<0.05$).

Although probiotic bacteria remained viable throughout the gastrointestinal tract and colonized in the intestine, they need to be strong against further threats including the use of antibiotics to sustain this colonization and conserve their presence in the flora [19, 20]. In addition, the transmission of antibiotic resistance genes to pathogenic bacteria from food bacteria and the proliferation of resistant pathogens in intestine are concerned as an important health issue. The inhibition effects of probiotics that possess antibiotic resistance genes, as well as their metabolites on pathogenic bacteria have recently been used strategically to prevent or treat infections such as acute gastroenteritis [19, 20]. A probiotic bacterium should at least be resistant to common antibiotics and must have antimicrobial activity on pathogenic bacteria [19, 20]. In our study, all *Lactobacillus plantarum* strains showed resistance to vancomycin. Overall, all strains showed susceptibility to clindamycin, azithromycin, ampicillin, gentamicin, erythromycin, and chloramphenicol. The antibiotic with the highest sensitivity of all strains was characterized as erythromycin. European Committee on Antimicrobial Susceptibility Testing (EU-

CAST) antibiotic resistance assessment data did not define the inhibition zone range in the disk diffusion method for gram-positive anaerobe bacteria. The resistant/sensitive terms mentioned in our study were used according to the zone formation and the size of the inhibition zone. Measurements of resistance/susceptibility of strains by EUCAST Minimum inhibitory concentration (MIC) method can be supported by further studies. In the literature, resistance of lactobacilli strains isolated from healthy babies to various antibiotics has been investigated. In our study, similar to literature, all *L. plantarum* strains experienced high sensitivity to erythromycin while showing resistance to vancomycin. Different results have been observed in different strains against other 8 used antibiotics [18, 26, 32-34].

One of the important features of probiotic bacteria is that they can inhibit pathogenic bacteria by producing HO, lactic acid, and various bacteriocins, and also, they can maintain flora balance [19, 20]. In our study, antimicrobial activity of isolated lactobacilli strains on pathogen *E. coli* ATCC 25922 was investigated by disk diffusion method and no formation of the inhibition zone was observed. The inhibition effect of lactobacilli strains against various pathogens has been criticized in many studies and different results have been reported. In a study, different *Lactobacillus* species such as *L. pentosus*, *L. casei spp rhamnosus*, *L. paracasei*, *L. casei*, *L. plantarum* and *L. fermentum* showed inhibition effects against *E. coli* ATCC with zone size 4 to 10 mm [18]. Another study reported inhibition zone sizes of *L. plantarum* strains against *E. coli* as 16-20 mm [19]. While some researchers reported inhibition zone sizes of isolated strains against *E. coli* as 11,3-14,8 mm, others noted as 0-23 mm [22, 35]. In our studies, the antimicrobial effect on *E. coli* ATCC 25922 was not observed in three different concentrations (5 µl, 10 µl and 15 µl) of seven *L. plantarum* strains.

CONCLUSION

The first objective of this study was to isolate lactobacilli that could survive in the presence of viral acute gastroenteritis agents. The second aim of this study was to determine some probiotic properties of these lactobacilli. As a result, it was observed that some *L. plantarum* strains were able to maintain their colonization in the intestine, despite of the viral infection and diarrhea. The some strains were able to maintain their viability in acidic environment, and even in media with bile salt. For this reason, when taken orally, the probiotic strains will be able to colonize in the intestine maintaining their viability in certain proportions, within acidic conditions of stomach as well as in bile condition of gut. Also, it was observed that the strains were resistant to vancomycin. In the works that we plan to do later, we aim to investigate some

probiotic properties such as to adhere to intestinal cells, production of some secondary metabolites, cholesterol removal and bile salt deconjugation.

ACKNOWLEDGEMENT

This study was supported by University of Hitit, Department of Scientific Research Projects (Project No. FEF19004.17.004)

REFERENCES

- Anderson EJ. Prevention and treatment of viral diarrhea in pediatrics. *Expert Reviews* 8 (2010) 205-217.
- Donà D, Mozzo E, Scamarcia A, Picelli G, Villa M, Cantarutti L, Giaquinto C. Community-Acquired Rotavirus Gastroenteritis Compared with Adenovirus and Norovirus Gastroenteritis in Italian Children: A Pediatric Study. *International Journal of Pediatrics* (2016) 5236243.
- Wilhelmi I, Roman E, Sanchez-Fauquier A. Viruses causing gastroenteritis. *Clinical Microbiology and Infection* 9 (2003) 247-262.
- Dashti AS, Ghahremani P, Hashempour T, Karimi A. Molecular Epidemiology of Enteric Adenovirus Gastroenteritis in under-Five-Year-Old Children in Iran. *Gastroenterology Research and Practice* (2016) 2045697.
- De Angelis M, Calasso M, Cavallo N, Di Cagno R, Gobbetti M. Functional proteomics within the genus *Lactobacillus*. *Proteomics* 16 (2016) 946-62.
- Gonzalez-Ochoa G, Flores-Mendoza LK, Icedo-Garcia R, Gomez-Flores R, Tamez-Guerra P. Modulation of rotavirus severe gastroenteritis by the combination of probiotics and prebiotics. *Archives in Microbiology* 199 (2017) 953-961.
- Grandy G, Medina M, Soria R, Araya M. Probiotics in the treatment of acute rotavirus diarrhea. A randomized, double-blind, controlled trial using two different probiotics preparations in Bolivian children. *Biomed Center: Infectious Diseases* (2010) 253.
- Vandenplas Y. 2016. Probiotics and prebiotics in infectious gastroenteritis. *Best Practice & Research Clinical Gastroenterology* 30 (2016) 49-53.
- Valerie MM, Rawson HL. Effects of exopolysaccharide-producing strains of thermophilic lactic acid bacteria on the texture of stirred yoghurt. *International Journal of Food Science and Technology* 34 (1999) 137-143.
- Dubois M, Gilles KA, Hamilton JK, Peters PA, Smith F. Colorimetric method for determination of sugars and related substances. *Analytical Chemistry* 28 (1956) 350-356.
- Luckey TD, Floch MA. Introduction to intestinal microbiology. *American Journal of Clinical Nutrition* 25 (1972) 1291-1295.
- Collins MD, Ribson GR. Probiotics, prebiotics and Synbiotics: Approaches for modulating the microbial ecology of the gut. *American Journal of Clinical Nutrition* 69 (1999) 1052-1057.
- Arrieta MC, Stiemsma LT, Amenyogbe N, Brown EM, Finlay B. The intestinal microbiome in early life: health and disease. *Frontiers in Immunology* 5 (2014) 427.
- Arbolea S, Watkins C, Stanton C, Ross RP. Gut Bifidobacteria populations in human health and aging. *Frontiers in Microbiology* 7 (2016) 1204.
- Chen ST, Tsai CN, Lee YS, Lin CY, Huang KY, Chao HC, Lai MW, Chiu CH. Intestinal microbiome in children with severe and complicated acute viral gastroenteritis. *Scientific reports* 7 (2017)

- 46130.
16. Jacobsen CN, Nielsen VR, Hayford AE, Moller PL, Michaelsen KF, Pærregaard A, Sandström B, Tvede M, Jakobsen M. Screening of Probiotic Activities of Forty-Seven Strains of *Lactobacillus* spp. by in vitro Techniques and Evaluation of the Colonization Ability of Five Selected Strains in Humans. *Applied and Environmental Microbiology* 65 (1999), 4949-4956.
 17. Martin R, Jimenez E, Olivares M, Marin ML, Fernandez L, Xaus J, Rodriguez JM. *Lactobacillus salivarius* CECT 5713, a potential probiotic strain isolated from infant feces and breast milk of a mother-child pair. *International Journal of Food Microbiology* 112 (2006) 35-43.
 18. Tulumoglu Ş, Yuksekdağ ZN, Beyatli Y, Şimsek Ö, Çınar B, Yaşar E. Probiotic properties of lactobacilli species isolated from children's feces. *Anaerobe* 24 (2013) 36-42.
 19. Kaushik JK, Kumar A, Duary RK, Mohanty AK, Grover S, Batish VK. Functional and probiotic attributes of an indigenous isolate of *Lactobacillus plantarum*. *Plosone* 4 (2009) e8099.
 20. Annuk H, Shchepetova J, Kullisaar T, Songisepp E, Zilmer M, Mikelsaar M. Characterization of intestinal lactobacilli as putative probiotic candidates. *Journal of Applied Microbiology* 94 (2003) 403-412.
 21. Sabir F, Beyatli Y, Cokmus C, Onal-Darilmaz D. Assessment of potential probiotic properties of *Lactobacillus* spp., *Lactococcus* spp., and *Pedococcus* spp. Strains isolated from Kefir. *Journal of Food Science* 75 (2010)
 22. Shokryazdan P, Sieo CC, Kalavathy R, Liang JB, Alitheen NB, Faseleh Jahromi M, Ho YW. Probiotic Potential of *Lactobacillus* Strains with Antimicrobial Activity against Some Human Pathogenic Strains. *BioMed Research International* (2014) 927268.
 23. Verdenelli MC, Ghelfi F, Silvi S, Orpianesi C, Cecchini C, Cresci A. Probiotic properties of *Lactobacillus rhamnosus* and *Lactobacillus paracasei* isolated from human faeces. *European Journal of Nutrition* 48 (2009) 355-363.
 24. Nawaz M, Wang J, Zhou A, Ma C, Wu X, Xu J. Screening and characterization of new potentially probiotic lactobacilli from breast-fed healthy babies in Pakistan. *African Journal of Microbiology Research* 5 (2011) 1428-1436.
 25. Papamanoli E, Tzanetakakis N, Litopoulou-Tzanetaki E, Kotzekidou P. Characterization of lactic acid bacteria isolated from a Greek dry-fermented sausage in respect of their technological and probiotic properties. *Meat Science* (2003) 859-867.
 26. Kotsou MG, Mitsou EK, Oikonomou IG, Kyriacou AA. In vitro assessment of probiotic properties of *Lactobacillus* strains from infant gut microflora. *Food Biotechnology* 22 (2008) 1-17.
 27. Nikolic M, Lopez P, Strahinic I, Suarez A, Kojic M, Fernandez-Garcia M, Topisirovic L, Golic N, Ruas-Madiedo P. Characterization of the exopolysaccharide (EPS)-producing *Lactobacillus paraplantarum* BGCG11 and its non-EPS producing derivative strains as potential probiotics. *International Journal of Food Microbiology* 158 (2012) 155-162.
 28. Caggianiello G, Kleerebezem M, Spano G. Exopolysaccharides produced by lactic acid bacteria: from health-promoting benefits to stress tolerance mechanisms. *Applied Microbiology Biotechnology* 100 (2016) 3877-86.
 29. Aslim B, Yüksekdağ ZN, Beyatli Y, Mercan N. Exopolysaccharide production by *Lactobacillus delbrückii* subsp. *bulgaricus* and *Streptococcus thermophilus* strains under different growth conditions. *World Journal of Microbiology & Biotechnology* 21 (2005) 673-677.
 30. Ren D, Li C, Qin Y, Yin R, Du S, Ye F, Liu C, Liu H, Wang M, Li Y, Sun Y, Li X, Tian M, Jin N. In vitro evaluation of the probiotic and functional potential of *Lactobacillus* strains isolated from fermented food and human intestine. *Anaerobe* 30 (2014) 1-10.
 31. EUCAST Disk Diffusion Method for Antimicrobial Susceptibility Testing - Version 7.0 (January 2019) http://www.eucast.org/fileadmin/src/media/PDFs/EUCAST_files/Disk_test_documents/2019_manuals/Manual_v_7.0_EUCAST_Disk_Test_2019.pdf
 32. Temmerman R, Pot B, Huys G, Swings J. Identification and Antibiotic Susceptibility of Bacterial Isolates from Probiotic Products. *International Journal of Food Microbiology* 81 (2003) 1-10.
 33. Kirtzalidou E, Pramateftaki P, Kotsou M, Kyriacou A. Screening for lactobacilli with probiotic properties in the infant gut microbiota. *Anaerobe* 17 (2011) 440-443.
 34. Klopper KB, Deane SM, Dicks LMT. Aciduric Strains of *Lactobacillus reuteri* and *Lactobacillus rhamnosus*, Isolated from Human Feces, Have Strong Adhesion and Aggregation Properties. *Probiotics and Antimicrobial Proteins* 10 (2017) 89-97.
 35. Olivares M, Diaz-Ropeo MP, Martin R, Rodriguez JM, Xausi J. Antimicrobial potential of four *Lactobacillus* strains isolated from breast milk. *Journal of Applied Microbiology* 101 (2006) 72-9.

Investigation of Antibacterial and Cytotoxic Properties of Mix Ligand Complex of Zinc 2-Fluorobenzoate with Nicotinamide

Cem Ozturk¹, Giray Bugra Akbaba¹

¹Kafkas University, Department of Bioengineering, Kars, Turkey

ABSTRACT

In this study, antibacterial properties of the previously synthesized zinc 2-fluorobenzoate with nicotinamide complex at 1.17; 2.33; 4.67; 9.34 and 18.67 mM concentrations was investigated using by agar well diffusion method against *Bacillus subtilis*, *Pseudomonasa eruginosa*, *Staphylococcus aureus*, *Escherichia coli*, *Bacillus cereus* and *Klebsiella pneumoniae* bacterias. The MTT method was used to determine the cytotoxic properties of the complex on human peripheral blood cells at the same concentrations. According to the results of the antibacterial study, it was determined that the complex showed a good antibacterial effect on all bacteria at 18.67 and 9.34 mM concentrations. The complex exhibits to have a suppressive effect only on *S. aureus* bacteria at a concentration of 2.33 mM. It was observed that the complex was antibacterial on all bacteria except *B. cereus* and *E. coli* at a concentration of 4.67 mM. The complex was found to have no growth inhibiting effect on any bacteria at a concentration of 1.17 mM. The cytotoxicity of the complex was investigated by MTT test method and it was determined that the cell viability decreased due to increasing concentration according to the test results. Cell viability at 1.17; 2.33; 4.67; 9.34 and 18.67 mM was determined to be 86.20%, 86.05%, 72.87%, 64.77% and 6.42%, respectively.

Keywords:

Zinc complexes, Antibacterial activity, MTT, Cytotoxicity, Antibiotics

Article History:

Received: 2019/08/23

Accepted: 2019/10/25

Online: 2019/12/31

Correspondence to: Giray Bugra Akbaba,

Department of Bioengineering, Kafkas University, 36100, Kars, Turkey

E-mail: gbugraakbaba@hotmail.com,

Phone: +90 474 225 11 50,

Fax: +90 474 225 12 82

INTRODUCTION

The purpose of crystal engineering is to explore new materials with striking properties that can be used in a variety of implementation areas. Metal complexes with an important place in crystal engineering consist of anions or molecules called ligands, which bind to a metal cation and metal atom at the center of symmetry. Metal complexes have been the subject of interest with the diversity of their structures for many years. The structures of metal complexes were determined to be influenced by the biological and physical properties of metal cations, ligands and intermolecular interactions [1-4]. Medical inorganic chemistry, which has an important place in materials science, is a multidisciplinary field consisting of chemistry, pharmacology, toxicology, and biochemistry. Medical chemists focus on the design and synthesis of new metal-based molecules with greater enhanced biological activity, better selectivity, low toxicity and multiple roles of mechanical effects to overcome the

clinical problems of commercially available drugs due to their side effects. Metal complexes are growth inhibitors of bacteria, which is supported by in vitro and in vivo studies [5, 6].

Carboxylic acids have many biological activities such as anti-inflammatory, antibacterial and antifungal. In dermatology, the sodium salt of benzoic acid is used as an antifungal agent. The antibacterial activity of carboxylic acids can be increased by forming complexes with metal ions. The anti-inflammatory and antibacterial activity of metal complexes was determined to be greater than free acid. Therefore, it is crucial to learn about the structure and binding relationships of complexes in the preparation of effective antibacterial species. However, activity is also known to decrease in some similar complexes. Recently, studies on antimicrobial activity of non-steroid anti-inflammatory drugs have shown that the complexes of transition metals

with various nitrogen-containing ligands show increased antimicrobial activity [7, 8]. Various metal complexes accelerate the effect of the drugs and organic therapeutics. Cobalt (II) mefenamic acid, naproxen, or tolfenamic acid [9-11] and mangan (II) tolfenamic acid complexes [12], copper (II) mefenamic acid, naproxen, diclofenac, diflunisal, and flufenamic acid complexes [13-15] exhibit biological activity. Zinc complexes with biologically active ligands have pharmaceutical effects because they are able to catalyze enzymatic processes in biological systems. Aromatic carboxylates (such as Naproxen, Ibuprofen, Indometacin) and aliphatic carboxylates (such as Valproic Acid) of zinc complexes with nitrogen-based ligands have been synthesized and their antibacterial and antimalarial properties have been studied recently. Most of zinc carboxylates with N-, O-, S- donor ligands have also antibacterial activity [16- 19].

In this study, the antibacterial activity of previously synthesized zinc 2-fluorobenzoate complexes with nicotinamide was determined against *Bacillus subtilis*, *Pseudomonas Aeruginosa*, *Staphylococcus aureus*, *Escherichia coli*, *Bacillus cereus* and *Klebsiella pneumoniae* by agar well diffusion method. Cytotoxicity of the complex was studied using MTT test method.

MATERIALS AND METHODS

Materials

Chemicals and Instruments

The compound used in the study was a previously synthesized and its structure was determined. The molecular structure of the complex was given in Fig. 1. Mueller Hinton Agar (Oxoid), Phosphate Buffered Saline, Antibiotic Antimycotic Solution, L-Glutamine solution, Histopaque-1077 and Dimethylsulfoxide (Sigma-Aldrich), BIO-AMF-1 medium and BIOAMF-1 supplement (Biological Industries) and MTT Cell Proliferation Assay Kit (Cayman Chemical) were purchased commercially. In this study, Nüve Steamart OT 40L autoclave, Nüve BM 101 Water bath, J.P. Selecta Digiheat drying and sterilization oven, ISOLAB vortex mixer, HETTICH EBA 200 centrifuge device, Panasonic MCO-170AICUVH-PE CO₂ Incubator and BioTek Epoch Spectrophotometer were used.

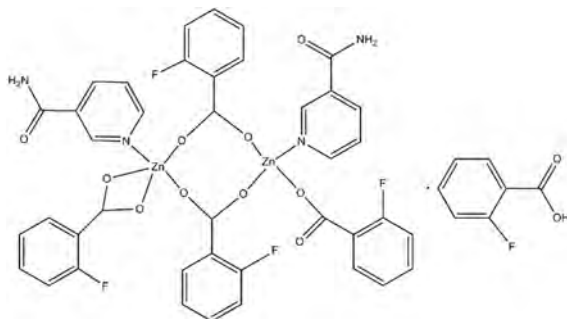


Figure 1. Molecular structure of the test compound [20]

Methods

Determination of Antibacterial Activity

Agar well diffusion method was used to evaluate the antibacterial effects of different concentrations of the tested compound. *B. subtilis* (ATCC 6633), *B. cereus* (ATCC 8035), *S. aureus* (ATCC 25923), *K. pneumoniae* (ATCC 33499), *P. aeruginosa* (ATCC 27852) and *E. coli* (ATCC 259222) were used in the study. Bacteria were stored at 4 °C until they were used. For the preparation of the agar to be used, 38 g Mueller Hinton (MH) agar was boiled and mixed in 1 L distilled water until completely dissolved. The prepared agar solution was kept in an autoclave for 15 minutes at 121 °C for sterilization. The agar transferred to Petri dishes and was cooled at the room temperature. Dimethyl sulfoxide (DMSO) was used as a negative control group. The cultivation of microorganisms was done on the prepared agar. Then, 5 mm diameter wells were formed on the agar surface. 50 µL of the tested compound were added to the wells. Petri dishes were incubated for 12 hours at 37 °C, and the diameter of the inhibition zone around each well was measured with the help of a ruler. The experiments were carried out in triplicate.

MTT Analysis

For the preparation of the culture medium, 75 mL of amnion cell culture medium, 15 mL of supplement, 1.5 mL of penicillin+streptomycin+amphotericin B (Antibiotic Antimycotic Solution) and 2 mL of L-glutamine were added in a sterile tube and kept at 37 °C. Lymphocytes were isolated from a human peripheral blood sample and cell counting was performed using a Thoma slide. After that 100 µL culture medium and 100 µL cell suspension (50000 cells/well) were added to the 96-well plates, respectively. The microplate was kept for 24 hours in 5% CO₂ incubator at 37 °C, allowing the cells to proliferate and adherence to the surface. After the incubation period was complete, 100 µL aliquots of different concentrations (1.17; 2.33; 4.67; 9.34 and 18.67 mM) of the compound were added to the wells. The cells were incubated at 37 °C for 24 hours in the incubator. When the incubation period was complete, 10 µL of MTT reagent was added to each well. The plate was gently mixed on the shaker. The cells were incubated at 37 °C for 3-4 hours. After incubation, formazan formed in the cells was seen as crystals in the bottom of the wells. Then, 200 µL DMSO was added to each well after the medium in the well was completely removed. It was kept in the incubator at 37 °C for 24 hours to dissolve the formazan crystals. At the end of the incubation, the absorbance values were measured by spectrophotometer at 570 nm.

RESULTS

Antibacterial Activity

Antimicrobial effects of zinc complex against Gram positive (*Bacillus subtilis*, *Bacillus cereus*, and *Staphylococcus aureus*) and Gram negative (*Klebsiella pneumoniae*, *Pseudomonas aeruginosa* and *Escherichia coli*) bacterial species were evaluated, and the results were given in Table 1 and Fig. 2. The compound at the concentrations of 18.67 and 9.34 mM was found to have antibacterial effects against all bacteria. It was found that the complex had no inhibitory effect on any bacteria at a concentration of 1.17 mM, meaning that the complex was not antibacterial at that concentration. At 2.33 mM concentration, the complex exhibits to have a suppressive effect only against *S. aureus* bacteria. It was determined that the complex showed antibacterial effect in all bacterial species except *B. cereus* and *E. coli* bacteria at 4.67 mM. The inhibition zones formed are seen in Fig. 3.

MTT Test

The results of MTT assay were evaluated. The absorbance values were measured by spectrophotometer. The decrease in cell viability according to the cell control group was calculated and obtained the percent inhibition values (Fig. 4). The % inhibition values were calculated according to the following formula and the obtained values are given in Table 2 and Fig. 4.

$$\text{Percent inhibition (\%)} = \frac{CVCC - CVTC}{CVCC} \times 100$$

(CVCC = Cell viability in cell control, CVTC= Cell viability at test concentrations)

When the obtained values are examined, it is seen that cell viability decreases with increasing concentration. At the concentrations of 1.17 mM, 2.33 mM, 4.67 mM and 9.34 mM, cell viability decreased by 13.80%, 13.95%, 27.13% and 35.23%, respectively. The cell death at 18.67 mM, the highest concentration we studied, was 93.58% and the highest cytotoxic effect was occurred at this concentration.

Table 1. Antibacterial activity results

Derişim	Inhibition zone diameters (mm)					
	Gram Positive			Gram Negative		
	<i>B. subtilis</i>	<i>B. cereus</i>	<i>S. aureus</i>	<i>K. pneumoniae</i>	<i>P. aeruginosa</i>	<i>E. coli</i>
Streptomycin (5.16×10^{-4} mM)	21.33	20.33	19.33	20.67	20.67	20.00
18.67 mM	18.67	16.33	20.33	18.67	14.33	16.00
9.34 mM	14.33	13.33	11.67	13.67	12.67	11.33
4.67 mM	8.67	-	10.00	8.67	10.00	-
2.33 mM	-	-	6.67	-	-	-
1.17 mM	-	-	-	-	-	-
DMSO	-	-	-	-	-	-

* <6 mm no antimicrobial activity; 6-15 mm weak antimicrobial activity; 15-20 mm strong antimicrobial activity; 20-25 mm very strong antimicrobial activity [21-23].

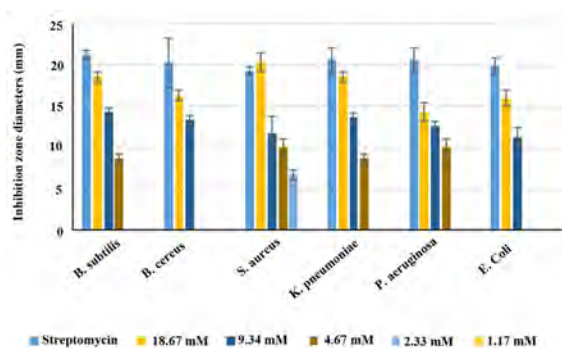


Figure 2. Comparison of inhibition zones in the studied concentrations

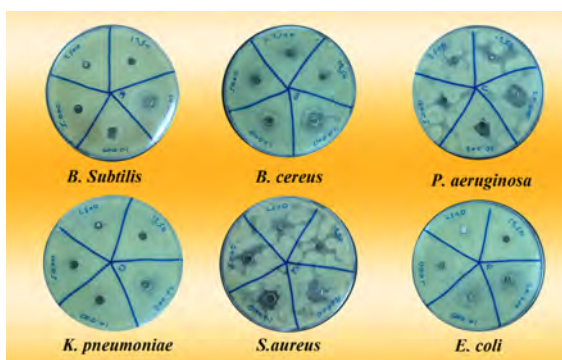


Figure 3. Inhibition zones formed by different concentrations of the tested compound

Table 2. Cell viability and inhibition values (%)

Concentrations	Cell Viability (%)	Inhibition (%)
Cell Control	100.00	-
1.17 mM	86.20	13.80
2.33 mM	86.05	13.95
4.67 mM	72.87	27.13
9.34 mM	64.77	35.23
18.67 mM	6.42	93.58

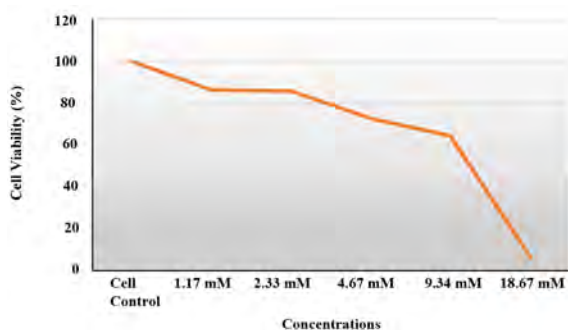


Figure 4. The percentages of cell viability

DISCUSSION

The antibacterial effect of zinc 2-fluorobenzoate nicotinamide complex at 1.17, 2.33, 4.67, 9.34 and 18.67 mM concentrations against *Bacillus cereus*, *Bacillus subtilis*, *Staphylococcus aureus*, *Pseudomonas aeruginosa*, *Escherichia coli* and *Klebsiella pneumoniae* was studied by agar well diffusion method. Cytotoxic effect of the complex on human peripheral blood lymphocyte cultures was determined by MTT method in vitro conditions. In this section, obtained results were evaluated and compared with literature.

The synthesis of new compounds has gained importance in the pharmaceutical sector due to the resistance of bacteria to antibiotics. The biological activities of the synthesized compounds are also examined. However, advanced clinical trials are not possible for all compounds for reasons such as time and economy. The antibacterial activities and toxic properties of newly synthesized compounds need to be determined. Therefore, researchers have very big tasks. Because high antibacterial activity and low toxicity make the compound a more important drug material. In this context, metal complexes have an important place in drug chemistry.

Omar and Abu Ali studied the antibacterial effect of zinc ibuprofen's complexes with 4,4'-bipyridine, 1,10-phenanthroline, 2,9-dimethyl-1,10-phenanthroline, 1,2-dimethylimidazole, 1,2-dimimidazole, 2-dimethylimidazole, 2-amino-6-picoline [24] and Ali et al. studied the antibacterial effect of zinc ibuprofen's complexes with 2-aminopyridine, 2-aminomethylpyridine and 2,2'-bipyridine and 2-(Methylamino)pyridine against *Micrococcus luteus*, *Staphylococcus aureus*, *Bacillus subtilis*, *Escherichia coli*, *Klebsiella pneumonia* and *Proteus mirabilis* at 6 g.L⁻¹ (6000 ppm) concentration [19]. Complexes with 4,4'-bipyridine, 1,10-phenanthroline, 2,9-dimethyl-1,10-phenanthroline and 2,2'-bipyridine were found to be effective on gram positive bacteria. These two studies show that the antibacterial effect may change depending on the metal and ligand used. The antibacterial effects of these compounds decrease as concentration decreases. There are no findings on toxic

ity in the studies. Zinc complexes of naproxen, one of the nonsteroidal and anti-inflammatory drugs, have also been synthesized. Antibacterial effects of the complexes obtained using different pyridine derivatives were studied by disc diffusion method against *Escherichia coli* and *Salmonella aureus* and by agar well diffusion method for *Staphylococcus aureus*, *Micrococcus luteus*, *Klebsiella pneumoniae*, *Pseudomonas aeruginosa*, *Proteus mirabilis* and *Escherichia coli*. The complexes obtained in these studies were suggested as antibiotics. But the toxicity of the complexes was not investigated [18, 25].

The antibacterial properties of zinc coumarin-3-carboxylate (100-1000 µg/mL) [26], zinc 5-iodo and 5-bromosalicylate (0.001-200 mmol.dm⁻³) [27], zinc 2-bromobenzoate (0.01-2.0 mmol.dm⁻³) [28] and zinc salicylates (1 mg/mL) [29] have been investigated. Although the main ligands has antibacterial activity, it has been reported that the antibacterial effect increases in some complexes (especially with pyridine derivatives). However, no additional studies have been carried out the toxicity of these compounds as well. In these studies, the importance of carboxylate complexes was emphasized related to their antibacterial properties. The most prominent feature that distinguishes our study from these studies was the antibacterial activity test as well as studying the cytotoxicity of the complex. In this study, it was determined that the compound has antibacterial properties according to inhibition zone diameters at the concentrations of 0.02 g/mL (18.67 mM) and 0.01 g/mL (9.34 mM). At 0.02 g/mL (18.67 mM) concentration, the complex showed a good antibacterial effect on the *B. cereus*, *B. subtilis*, *S. aureus*, *P. aeruginosa*, *E. coli* and *K. pneumoniae*. But the cytotoxicity results showed that the rate of death of lymphocyte cells was 93.58 % at same concentration. Similarly, a moderate antibacterial effect occurred at a concentration of 0.01 g/mL on all studied bacteria, while MTT test results found 35.23% cell death. There is no study on the antibacterial activity of zinc 2-fluorobenzoate and its other pyridine derivatives and any of its complexes in the literature. Antibacterial and cytotoxic effects of zinc 2-fluorobenzoate were investigated for the first time in this study.

There are also some studies in the literature that investigate the cytotoxicity of different zinc complexes. For example, Zhu et al. synthesized zinc 2,4,5-benzenetetracarboxylic acid complex with 1,3,5-Tris (1-imidazolyl) benzene and its cytotoxicity was determined by MTT method on HeLa and KB cancer cell lines at the concentrations of 4, 12, 36, 110 and 330 µg.mL⁻¹ [30]. In a study conducted with the concentration close to the concentrations in our study, it was reported that zinc complex of Schiff bases derived from o-vanillin was cytotoxic on A549, HeLa, HL-60 and K562 cancer cell lines at a concentration of 1% [31]. Although the complexes synthesized in these studies were suggested as an

anticarcinogenic agent, their effects on healthy cells at the concentrations studied were not investigated. The results of our study were evaluated as negative, indicating that the tested compound was cytotoxic on the human lymphocyte cell line.

CONCLUSIONS

In this study, antibacterial and cytotoxic properties of pre-synthesized zinc 2-fluorobenzoate nicotinamide complex were evaluated. The complex showed good activity against Gram positive (*B. subtilis*, *B. cereus* and *S. aureus*) and Gram negative (*K. pneumonia*, *P. aeruginosa* and *E. coli*) bacteria at 18.67 mM concentration. At the same concentration, the complex was found to exhibit cytotoxic properties. The antibacterial effect of the concentration was found to decrease as the concentration decreased. The cytotoxicity of the complex increases with increasing concentration. The biological activity of the compound becomes insignificant due to increased death in lymphocyte cells at the concentration at which the antibacterial effect increases. In conclusion, when the findings obtained from this study are evaluated, the zinc 2-fluorobenzoate complex with nicotinamide exhibits antibacterial properties and is not recommended as a drug-specific material because it is cytotoxic at the same concentrations.

ACKNOWLEDGEMENT

This study was produced from the master thesis of the first author. The authors thank to Dr. Cem Öziç and Dr. Füreya Elif Özbek for their supports.

References

- Noro S, Miyasaka H, Kitagawa S, Wada T, Okubo T, Yamashita M, Mitani T. Framework Control by a Metalloligand Having Multicoordination Ability: New Synthetic Approach for Crystal Structures and Magnetic Properties. *Inorganic Chemistry* 44(1) (2005) 133-146.
- Teo P, Hor TSA. Spacer directed metallo-supramolecular assemblies of pyridine carboxylates. *Coordination Chemistry Reviews* 255(1-2) (2011) 273-289.
- Gündüz T. *Koordinasyon Kimyası*, third ed. Gazi Kitabevi, Ankara, 2005.
- Yamada K, Yagishita S, Tanaka H, Tohyama K, Adachi K, Kaizaki S, Kumagai H, Inoue K, Kitaura R, Chang HC, Kitagawa S, Kawata S. Metal-Complex Assemblies Constructed from the Flexible Hinge-Like Ligand H2bhnq: Structural Versatility and Dynamic Behavior in the Solid State. *Chemistry – A European Journal* 10(11) (2004) 2647-2660.
- Weiss RB, Christian MC. New cisplatin analogues in development. *Drugs* 46(3) (1993) 360-377.
- Sathiyaraj S, Sampath K, Butcher RJ, Pallegogu R, Jayabalakrishnan C. Designing, structural elucidation, comparison of DNA binding, cleavage, radical scavenging activity and anticancer activity of copper(II) complex with 5-dimethyl-2-phenyl-4-[(pyridin-2-ylmethylene)-amino]-1,2-dihydro-pyrazol-3-one Schiff base ligand. *European Journal of Medicinal Chemistry* 64 (2013) 81-89.
- Uivarosi V. Metal Complexes of Quinolone Antibiotics and Their Applications: An Update. *Molecules* 18(9) (2013) 11153-11197.
- Rizzotto M. A search for antibacterial agents, in: Bobbarala V. (Ed.). *A search for antibacterial agents*. InTech., Croatia, pp. 73-88, 2012.
- Dimiza F, Papadopoulos AN, Tangoulis V, Psycharis V, Raptopoulou CP, Kessissoglou DP, Psomas G. Biological evaluation of non-steroidal anti-inflammatory drugs-cobalt(II) complexes. *Dalton Transactions* 39(19) (2010) 4517.
- Dimiza F, Papadopoulos AN, Tangoulis V, Psycharis V, Raptopoulou CP, Kessissoglou DP, Psomas G. Biological evaluation of cobalt(II) complexes with non-steroidal anti-inflammatory drug naproxen. *Journal of Inorganic Biochemistry* 107(1) (2012) 54-64.
- Tsilio S, Kefala LA, Perdih F, Turel I, Kessissoglou DP, Psomas G. Cobalt(II) complexes with non-steroidal anti-inflammatory drug tolfenamic acid: Structure and biological evaluation. *European Journal of Medicinal Chemistry* 48 (2012) 132-142.
- Zampakou M, Rizeq N, Tangoulis V, Papadopoulos AN, Perdih F, Turel I, Psomas G. Manganese(II) Complexes with the Non-steroidal Anti-Inflammatory Drug Tolfenamic Acid: Structure and Biological Perspectives. *Inorganic Chemistry* 53(4) (2014) 2040-2052.
- Dimiza F, Fountoulaki S, Papadopoulos AN, Kontogiorgis CA, Tangoulis V, Raptopoulou CP, Psycharis V, Terzis A, Kessissoglou DP, Psomas G. Non-steroidal anti-inflammatory drug-copper(II) complexes: Structure and biological perspectives. *Dalton Transactions* 40(34) (2011) 8555-8568.
- Fountoulaki S, Perdih F, Turel I, Kessissoglou DP, Psomas G. Non-steroidal anti-inflammatory drug diflunisal interacting with Cu(II). Structure and biological features. *Journal of Inorganic Biochemistry* 105(12) (2011) 1645-1655.
- Tolia C, Papadopoulos AN, Raptopoulou CP, Psycharis V, Garino C, Salassa L, Psomas G. Copper(II) interacting with the non-steroidal anti-inflammatory drug flufenamic acid: Structure, antioxidant activity and binding to DNA and albumins. *Journal of Inorganic Biochemistry* 123 (2013) 53-65.
- Darawsheh M, Abu Ali H, Abuhijleh AL, Rappocciolo E, Akkawi M, Jaber S, Maloul S, Hussein Y. New mixed ligand zinc(II) complexes based on the antiepileptic drug sodium valproate and bioactive nitrogen-donor ligands. Synthesis, structure and biological properties. *European Journal of Medicinal Chemistry* 82 (2014) 152-163.
- Abu Ali H, Darawsheh MD, Rappocciolo E. Synthesis, crystal structure, spectroscopic and biological properties of mixed ligand complexes of zinc(II) valproate with 1,10-phenanthroline and 2-aminomethylpyridine. *Polyhedron* 61 (2013) 235-241.
- Abu Ali H, Fares H, Darawsheh M, Rappocciolo E, Akkawi M, Jaber S. Synthesis, characterization and biological

- activity of new mixed ligand complexes of Zn(II) naproxen with nitrogen based ligands. *European Journal of Medicinal Chemistry* 89 (2015) 67-76.
19. Abu Ali H, Omar SN, Darawsheh MD, Fares H. Synthesis, characterization and antimicrobial activity of zinc(II) ibuprofen complexes with nitrogen-based ligands. *Journal of Coordination Chemistry* 69(6) (2016) 1110-1122.
 20. Özbek FE. 2-Halojenobenzoat Komplekslerinin Sentezi ve Özellikleri. Thesis of Ph.D. Graduate School of Applied and Natural Sciences, Kafkas University (2011) 222 pages.
 21. Al-Majidi SMH. Synthesis of some new 4-oxo-thiazolidines, tetrazole and triazole derived from 2-SH-benzothiazole and antimicrobial screening of some synthesized. *Journal of Saudi Chemical Society* 18(6) (2014) 893-901.
 22. Bauer AW, Kirby WMM, Sherris JC, Turck M. Antibiotic Susceptibility Testing by a Standardized Single Disk Method. *American Journal of Clinical Pathology* 45 (1966) 493-496.
 23. Chohan ZH, Supuran CT. Organometallic compounds with biologically active molecules: in vitro antibacterial and antifungal activity of some 1,1'-(dicarbohydrazono) ferrocenes and their cobalt(II), copper(II), nickel(II) and zinc(II) complexes. *Applied Organometallic Chemistry* 19(12) (2005) 1207-1214.
 24. Omar SN, Abu Ali H. New complexes of Zn(II) with the anti-inflammatory non-steroidal drug, ibuprofen and nitrogen donor ligands. Synthesis, characterization and biological activity. *Journal of Coordination Chemistry* 70(14) (2017) 2436-2452.
 25. Chiniforoshan H, Tabrizi L, Hadizade M, Sabzalian MR, Chermahini AN, Rezapour M. Anti-inflammatory drugs interacting with Zn (II) metal ion based on thiocyanate and azide ligands: Synthesis, spectroscopic studies, DFT calculations and antibacterial assays. *Spectrochimica Acta Part A: Molecular and Biomolecular Spectroscopy* 128 (2014) 183-190.
 26. Islas MS, Martínez Medina JJ, Piro OE, Echeverría GA, Ferrer EG, Williams PAM. Comparisons of the spectroscopic and microbiological activities among coumarin-3-carboxylate, o-phenanthroline and zinc(II) complexes. *Spectrochimica Acta Part A: Molecular and Biomolecular Spectroscopy* 198 (2018) 212-221.
 27. Košická P, Gyoryová K, Smolko L, Gyepes R, Hudecová D. Synthesis, crystal structures, spectral, thermal and antimicrobial properties of new Zn(II) 5-iodo- and 5-bromosalicylates. *Journal of Molecular Structure* 1155 (2018) 232-238.
 28. Krajníková A, Gyoryová K, Hudecová D, Kovárová J, Vargová Z. Thermal decomposition and antimicrobial activity of zinc(II) 2-bromobenzoates with organic ligands. *Journal of Thermal Analysis and Calorimetry* 105(2) (2011) 451-460.
 29. Chooset S, Kantacha A, Chainok K, Wongnawa S. Synthesis, crystal structure, luminescent properties and antibacterial activities of zinc complexes with bipyridyl and salicylate ligands. *Inorganica Chimica Acta* 471 (2018) 493-501.
 30. Zhu M, Zhao H, Peng T, Su J, Meng B, Qi Z, Jia B, Feng Y, Gao E. Structure and cytotoxicity of zinc (II) and cobalt (II) complexes based on 1,3,5-tris(1-imidazolyl) benzene: DNA Binding; Fluorescence; anticancer; Apoptosis; Molecular docking. *Applied Organometallic Chemistry* 33(3) (2019) e4734.
 31. Niu MJ, Li Z, Chang GL, Kong XJ, Hong M, Zhang Q. Crystal Structure, Cytotoxicity and Interaction with DNA of Zinc (II) Complexes with o-Vanillin Schiff Base Ligands. *PLOS ONE* 10(6) (2015) e0130922.

Performance Analysis of an integrated Semi-Transparent Thin Film PV Vacuum Insulated Glazing

Hasila Jarimi¹, Ke Qu¹, Shihao Zhang¹, Qinghua Lv^{1,2}, Daniel Cooper¹, Yuehong Su¹, Saffa Riffat¹

¹Nottingham University, Architecture and Built Environment, Nottingham, United Kingdom

²Hubei University of Technology, Environmental Hubei Collaborative Innovation Center for High-efficient Utilization of Solar Energy, Hubei, Wuhan, China

ABSTRACT

This paper is intended to design and develop a thermal model of an integrated semi-transparent thin-film PV vacuum glazing with four layers of glass called PV VG-4L. The design of the glazing involves integration between a thin-film PV glazing with a double vacuum glazing (both manufactured independently), and an additional layer of self-cleaning coated glass. For the mathematical model, the energy balance equations were derived for the thin-film PV glass, the glass panes of the vacuum glazing and the edges of the internal and external glass surfaces (facing indoors and outdoors respectively). The model was numerically solved in MATLAB. To evaluate the performance of the PV VG-4L, the prototype was manufactured and investigated at lab-scale and also under real conditions. At lab-scale, experiments were conducted at steady-state conditions using a TEC driven calibrated hot box at Sustainable Energy Research Lab, University of Nottingham, UK. Meanwhile, outdoors, the prototype was tested at a research house at the University of Nottingham, UK. The developed model was then validated against the experimental results by direct comparison on the trend of the experimental and theoretical curves obtained, and also by conducting error analysis using root mean squared percentage deviation (RMSPD) method. When tested using the calibrated hot box, by following closely the ISO 12567 standards, the average measured total U-value is 0.6 W/m²K. From the analysis, the computed RMSPD value for the glazing surface temperature and the U-value are 4.75 % and 0.96% respectively. The RMSPD computed for the glazing surface temperatures, electrical power generated under real conditions and U-value are 2.58 %, 1.4% and 6.86 % respectively. The theoretical and experimental results are concluded to be in good agreement. The thermal and electrical performance of a building retrofitted with and without PV VG-4L was examined and discussed. At building efficiency level, the PV VG-4L not only can produce power, but it also has high insulating properties. The promising U-value implies that the glazing's range of potential applications can be improved depending on the energy needs and applications, which includes its use in BIPV solar façades (PV curtain walling) for commercial buildings, greenhouses, skylights and conservatories.

Keywords:

Semi-transparent thin-film PV; Low U-value; SHGC.

INTRODUCTION

There is a continuous growth in global buildings sector reaching an estimated 235 billion m² in 2016. Building energy consumption was reported to account for 28% of global energy-related CO₂ emissions in 2018. It has also been reported that, in that year, buildings-related CO₂ emissions rise to as high as 9.6 Gt CO₂ for the second year in a row [1]. In terms of efficient building sector, there is a great potential for building-integrated PV technologies (BIPV) to offer potential energy savings of a building by gener-

ating solar energy resources captured via the building materials itself. This is portrayed by the global BIPV market which is estimated to reach revenues of around \$7 billion by 2024, growing at a CAGR of approximately 15% during 2018-2024 [2].

A thin-film photovoltaic (PV) glass is a clean energy technology that uses transparent photovoltaic cells such as amorphous silicon (α -Si) and microcrystalline/amorphous (μ C-Si) to harvest solar energy. These pho-

Article History:

Received: 2019/10/08

Accepted: 2019/10/31

Online: 2019/12/31

Correspondence to: Hasila Jarimi,
Nottingham University, Department of
Architecture and Built Environment,
School of Engineering, United Kingdom

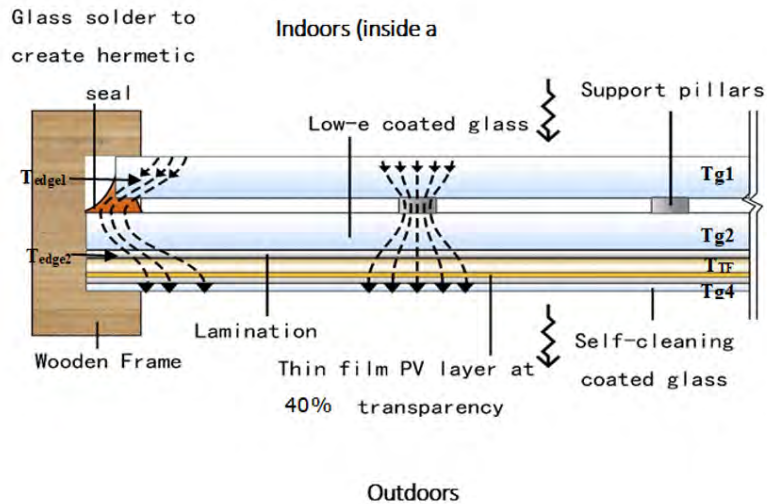


Figure 1. Schematics of PV VG-4L and the heat flow through the glass panes.

Photovoltaic cells are typically deposited on super-clear float glass, with TCO layers as the conductive layers and an ultra-clear float glass as the glass cover. When replacing a building envelope, in the context of building insulation performance which is mainly represented by the U-value, thin-film PV glass has a similar thermal transmittance (U-value) to single glazing ($\sim 5 \text{ W/m}^2\text{K}$) [3]. Therefore, to improve its thermal performance, thin-film PV glass is generally integrated into double glazing applications [4]. However, such configurations have certain limitations, including the heavy weight due to the thick frame, while the use of the inert gas between the glass panes is not easy to maintain. A group of researchers from China [5] proposed an integration between a thin-film PV glazing with a vacuum glazing. The glazing prototype was designed and manufactured in such a way that a lamination layer was sandwiched between the thin film PV glazing unit and a vacuum glazing unit, both are independently manufactured. According to the researchers, although semi-transparent photovoltaic windows can generate electricity in situ, they also increase the cooling load of buildings significantly due to the waste heat as a by-product. Experiment has been conducted and the results have indicated that the prototype can not only generate electricity, but also help reduce the cooling load as well as improve the indoor thermal comfort. Recently, researchers [6] investigated a combined semi-transparent multicrystalline PV vacuum glazing. They have found that the combination of multicrystalline PV cells with vacuum glazing provide low overall heat transfer coefficient, reduces solar heat gain, generates clean electricity and allows comfortable daylight. In this paper, a novel design of semi-transparent thin-film PV glazing integrated with a vacuum glazing and a layer of self-cleaning coated glass called PV-VG 4L is introduced. Setting it apart from the research conducted by the researchers mentioned above, this paper is intended to develop the thermal model and also to discuss the performance analysis of the novel glazing design in detail both in the lab and real conditions.

Using the validated mathematical model, a building thermal load retrofitted with PV VG-4L in winter condition in the UK was examined.

DESIGN CONCEPT AND HEAT TRANSFER ANALYSIS OF THIN FILM PV VACUUM INSULATED GLAZING (PV VG-4L)

The design of PV VG-4L is illustrated in Figure 1. PV VG-4L involves an integration between a thin film PV glazing with a double vacuum glazing (both manufactured independently) and an additional layer of self-cleaning coated glass which totaling 4 layers of glass units which gives the total thickness of 14 mm. The use of self-cleaning coating on the glass surface will increase PV life time, enhance efficiency by 1-3%, and reduce cleaning requirements. The layers were combined via Ethylene Vinyl Acetate (EVA) film using an autoclave facility which was set at its optimum temperature and pressure. For this research, a-Si thin film PV glazing (40% transparency) was used. The heat transfer was analysed based on the following temperature nodes which are; the average glass temperature facing indoors denoted by T_{g1} , the average internal glass temperature denoted by T_{g2} , the average temperature of the thin film PV glass denoted by T_{TF} and the average temperature of the self-cleaning coated glass denoted by T_{g4} . The lateral heat transfer ends at the point right at the edge sealing and the temperature was denoted as T_{edge1} . Due to high thermal conductivity of the edge sealing, it acts as a short circuit for the heat transfer at the edges of the glazing. Meanwhile, due to high thermal conductivity between g2 and g4, the lateral heat conduction in the glass slab g2 and thin film PV glass (TF) are assumed negligible. The temperature of the position in g4, of which the edge heat transfer takes place is denoted as T_{edge1} .

ted as T_{edge2} . For the uninsulated edges, there will be heat transferred from the internal ambient to the area around the edges.

When the PV panel absorbed solar radiation, a fraction of the absorbed solar radiation will be converted into useful power meanwhile a fraction will be wasted in the form of heat. This heat released by the PV panel is insulated from the building via the vacuum layer of which, the main heat transfer occurs in the gap are mainly due to radiation and conduction through the support pillars and the edge seal. In the summer, this can be considered as an advantage since the installation of PV glazing would normally cause additional heating during summer of which in return, increase the cooling load of a building. Based on the heat transfer mechanism, the energy balance equations at steady state conditions were developed. In order to simplify the analysis, the following assumptions have been made:

- The heat transfer involved is assumed symmetrical. Therefore, we only consider a quarter of the PV VG-4L area in the heat transfer analysis.
- In this study, we have considered the lateral heat transfer through the glass slab in g1 and g4. This is because, the vacuum glazing is highly thermally insulated which makes the lateral heat transfer to become prominent.
- The edge boundaries of the PV VG-4L are well insulated and hence the edge losses are assumed negligible.
- Due to high thermal conductivity of the edge sealing, the edge seal is assumed as a thermal short circuit.
- Meanwhile, due to high thermal conductivity between g2 and g4, the lateral heat conduction in the glass slab g2 and thin-film PV glass (TF) are assumed negligible.
- Multireflection between the inner glass panes are considered in the calculation of the absorbed solar radiation by the glass layers.

To simulate the performance of the PV VG-4L, energy balance equations were developed for each of the temperature nodes.

For g1:

$$\underbrace{S_{g1}}_1 + \underbrace{h_{a-g1}(T_{a,i} - T_{g1})}_2 = \underbrace{h_{g1-g2}(T_{g1} - T_{g2})}_3 + \underbrace{h_{k-edge}(T_{g1} - T_{edge1})}_4 \quad (1)$$

The heat transfer terms are defined as follows:

- 1: The rate of the solar energy received by the glass cover or surface facing indoors after transmission through different glass layers per unit area; 2: The rate of heat transfer from the indoor ambient to g1 per unit area; 3: The rate of heat transfer from g1 to g2 per unit area. The heat transfer includes heat conduction through the glass slabs of g1, followed by heat transfer in the vacuum gap (due to the heat conduction of the gas particles) radiative heat transfer, and heat conduction through the support pillars; 4: The rate of lateral heat conducted along the x-direction and y-direction of the PV VG-4L from the centre of the PV VG-4L.

For Tedge1:

$$\underbrace{h_{k-edge} \gamma_c (T_{g1} - T_{edge1})}_4 + \underbrace{h_{i-edge} \gamma_{edge} (T_{a,i} - T_{edge1})}_5 = \underbrace{h_{edge} \gamma_{edge} (T_{edge1} - T_{edge2})}_6 \quad (2)$$

The heat transfer terms are defined as follows:

- 5: The rate of heat transfer from the indoor ambient to the edge area per unit glazing area (if not insulated); 6: The rate of heat transfer from edge 1 to edge 2 through g2, TF and EVA layer per unit area.

For g2:

$$\underbrace{h_{g1-g2}(T_{g1} - T_{g2})}_3 + \underbrace{S_{g2}}_7 = \underbrace{h_{g2-TF}(T_{g2} - T_{TF})}_8 \quad (3)$$

The heat transfer terms are defined as follows:

- 7: The rate of the solar energy received by g2 after transmission through different glass layers per unit area; 8: The rate of heat transfer from g2 to TF through the EVA layer per unit area.

For TF:

$$\underbrace{h_{g2-TF}(T_{g2} - T_{TF})}_8 + \underbrace{S_{TF}}_9 = \underbrace{h_{TF-g4}(T_{TF} - T_{g4})}_{10} \quad (4)$$

The heat transfer terms are defined as follows:

- 9: The rate of the solar energy received by thin film PV layer (TF) after transmission through different glass layers per unit area; 10: The rate of heat transfer from TF to g4 through the EVA layer per unit area.

For Tedge2:

$$\underbrace{h_{edge} \gamma_{edge} (T_{edge1} - T_{edge2})}_6 = \underbrace{h_{k-edge} \gamma_c (T_{edge2} - T_{g4})}_{11} \quad (5)$$

Table 1. The definition of the symbol used.

Symbol	Definition	Symbol	Definition
S_{g1}, S_{g2}, S_{TF}	The absorbed solar radiation for $g1$, $g2$ and TF respectively	γ_c	Correction factor due to the total area of the PV VG-4L
γ_{edge}	Correction factor due to the total area of edge sealing	h_{edge}	Conductive heat transfer coefficient due to the edge sealing
δ_{edge}	The edge sealing thickness	h_{iedge}	Total heat transfer coefficient from the indoor ambient air to the uninsulated edge sealing area
h_p	Heat transfer coefficient through the support pillars	h_{g1-g2}	The total heat transfer coefficient from $g1$ to $g2$ of vacuum glazing
h_{k_edge}	The lateral heat transfer to the glass edge	h_{g2-TF}	The total coefficient of heat transfer by conduction from $g2$ to the thin film PV glass layer TF .
h_{a-g1}	Total heat transfer coefficient from the internal ambient to $g1$	k_{edge}	Thermal conductivity through the edge sealing
h_{TF-g4}	The total heat transfer coefficient by conduction from the thin film PV glass layer TF to $g4$.	T_{a-i}	Indoor ambient temperature
h_o	Total heat transfer coefficient from the external glass $g4$ to the ambient	T_{a-o}	Outdoor ambient temperature

The heat transfer terms are defined as follows:

11: The rate of lateral heat conduction along the x-direction and y-direction of the PV VG-4L from the centre of the PV VG-4L.

For γ_c :

$$\frac{h_{TF-g4}(T_{TF}-T_{g4})}{10} + \frac{h_{k_edge}\gamma_c(T_{edge2}-T_{g4})}{11} + \frac{S_{g4}}{12} = \frac{h_o(T_{g4}-T_{a-o})}{14} \quad (6)$$

The heat transfer terms are defined as follows:

12: The rate of the solar energy received by $g4$ after transmission through different glass layers per unit area; 14: The rate of heat transfer from $g4$ to T_{a-o} per unit area.

To theoretically predict the glazing's electrical performance, the following correlation developed by Schott [7] and Evans [8] is used:

$$\eta_{eff} = \eta_{Tref} (1 - \beta_{ref} (T_{TF} - T_{ref})) \quad (7)$$

Where β_{ref} temperature coefficient of the thin-film PV is cells and η_{Tref} is the electrical efficiency at reference temperature (25°C). From the simulation, the values of the average temperature of the glass sheets (layers) were used to compute the heat transfer coefficients summarised in Table A.1. The centre thermal resistance R_{centre} and the edge thermal resistance R_{edge_tot} can be computed as in equation (8) and (9) respectively.

$$R_{centre} = \frac{1}{h_{a-g1}} + \frac{1}{h_{g1-g2}} + \frac{1}{h_{g2-TF}} + \frac{1}{h_{TF-g4}} + \frac{1}{h_o} \quad (8)$$

$$R_{edge_tot} = \frac{1}{h_{edge}} + \frac{1}{h_{k_edge}} + \frac{1}{h_{iedge}} \quad (9)$$

U-value is defined as the measure of heat transfer or thermal transmittance from a warm space of a building to the external cooler environment or vice versa. It reflects how well a glazing unit as a heat insulator. In this study, the centre U-value (U_{centre}) and the total U-value (U_{total}) may be computed using equation 10 and 11 respectively:

$$U_{centre} = \frac{1}{R_{centre}} \quad (10)$$

$$U_{total} = U_{centre}\gamma_c + u_{edge_tot}\gamma_{edge} \quad (11)$$

In this study, to solve the energy balance equations, we have used the inverse matrix method. MATLAB is used to carry out the iteration process with Newton-Raphson iteration technique is used to estimate the temperature and hence the temperature-dependent heat transfer coefficients of the variables.

RESULTS AND DISCUSSIONS

U-Value Measurement using A TEC Driven Calibrated Hot Box

A PV VG-4L prototype as shown in Fig. 2 was manufactured. The U-value of the prototype was evaluated using the TEC-driven calibrated hot box built at the University of Nottingham. Interested readers may refer to [9] for



Figure 2. The PV VG-4L prototype

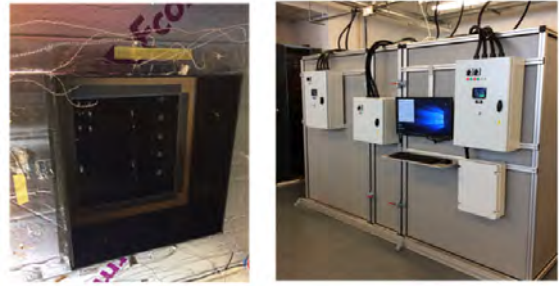


Figure 3. The calibrated hot box with the installed sample

further details. As can be seen in Figure 3, by following closely ISO 12567 standards, the sample was installed at the specimen area of the calibrated hot box. It was tested under three different air temperature conditions summarised in Table 2. However, the air speed in the hot and cold side were fixed at 0.3 m/s and 1.5 m/s respectively. Using the calibrated hot box, we could estimate the total heat transfer coefficient from the hot and cold surface of the PV VG-4L prototype. The values were then used as the input parameters for the computer simulation. To derive the absolute error, the Kline–McClintock second power law as given in NCEES (National Council of Examiners for Engineering and Surveying) (2001) is used. These errors were represented by the error bars of the associated curves. Additionally, the guideline in ISO 12567 was also being referred to evaluate the error from indoor testing.

The mathematical model validation method is performed by comparing the results obtained experimentally and theoretically based on the trends shown on the related graphs. In this study, the mathematical model has been validated against the indoor experimental data with the input parameters recorded in the experiment were used in the computer simulation for all the three different conditions. In addition to the direct comparison between the simulation and theoretical curves, the validation of the mathematical model is further justified using root mean square percentage deviation (RMSPD). As shown in Figure 4, and summarised in Table 3, the evaluated glazing surface temperatures and U-value are found to be in good agreement such that the trend of the theoretical curves are consistent with the experimental curves and the computed RMSPD for the temperatures and U-value are 4.75% and 0.96% respectively.

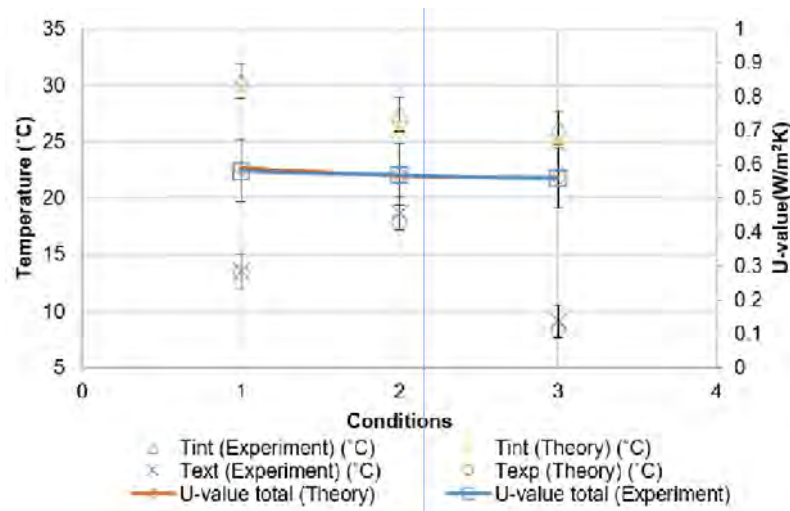


Figure 4. Comparison between the theoretical and experimental results for the glazing surface temperature and U-value using the calibrated hot box.

Table 2. Comparison between the Theoretical and Experimental Results for the glazing surface temperature and U-value using the calibrated hot box under different sets of controlled ambient temperature conditions.

Cond.	Text (°C)	Tint (°C)	Tint (Exp) (°C)	Text (Exp) (°C)	Tint (Theo) (°C)	Tint (Theo) (°C)	U-value total (Exp)	U-value total (Theo)
1	12.7	32.70	30.34	13.50	29.73	13.40	0.56	0.58
2	17.5	27.5	27.40	18.65	26.05	17.89	0.57	0.56
3	7.6	27.83	25.19	9.13	24.92	8.19	0.56	0.56

Table 3. Measured parameters and uncertainties

Parameters	Sensor	Uncertainties
Temperatures	K-type Thermocouples	$\pm 1.5\text{ }^\circ\text{C}$
Heat flux	Hukseflux Thermal Sensors	$\pm 1.9 \times 10^{-6}\text{ V}/(\text{W}/\text{m}^2)$
Solar radiation	Pyranometer	$\pm 5\%$
Maximum power produced by the PV VG-4L	RO4 with Keysight 34972A	Electric current (I) ($\pm 1.5\text{ }\mu\text{A}$) Voltage (V) ($\pm 190\text{ }\mu\text{V}$)

Performance Analysis under Real Conditions

The developed mathematical model has been validated against indoor experimental analysis. Nonetheless, the true performance of the PV VG-4L under real sky conditions still needs to be investigated in order to further justify the validity of the mathematical model especially that the electrical performance of the thin film PV glazing could not be evaluated indoors. That said, this section first discusses the performance of the PV VG-4L under real conditions. To carry out the testing, the prototype was installed at E.ON 2016 research house at the University of Nottingham, United Kingdom with latitude of 52.9438° N , and longitude of -1.1934° W . It is important to note that the pyranometer to measure the incident solar radiation was placed parallel to the surface of the PV VG-4L. It is worth emphasising that the outdoor monitoring of the PV VG-4L has been conducted under two conditions; during the day and during the night (at zero solar radiation). The thermal and electrical characteristics of the PV VG-4L under real conditions were monitored using the sensors as summarised in Table 4. During the day, the reading given by the heat flux sensor for the thermal transmittance of the PV VG-4L gives the value of the heat

gain. Therefore, during the day, the only parameters that are being considered are the surface temperature difference of the PV VG-4L, its electrical power produced, and also the estimated g-factor. The typical monitoring period is between 9:30 a.m. to 5:00 p.m. in a typical day of June. Meanwhile, the focus of the experiment during the night is the thermal transmittance measurement or U-value. A 1kW convective heater was used as the heat source for indoors.

Figure 5 shows the solar radiation, surface temperatures of the PV VG-4L, and both internal and external; glazing surface temperature during the day and night. It should be noted that for the data taken on the 27th of June to 28th of June 2019, the average heating temperature was set to heat the ambient room at 24 to 25 $^\circ\text{C}$. On the day of testing, the sky was in a clear sky condition and hence clear pattern of solar radiation curve with the time of the day was obtained. At low –zero solar radiation, the indoor surface temperature of the PV VG-4L is in general higher than its external surface temperature. However, as the incident solar radiation increases, the external surface temperature increases. The trend of the graph is explained as follows; when the PV component of the PV VG-4L absorbed the incident solar ra-

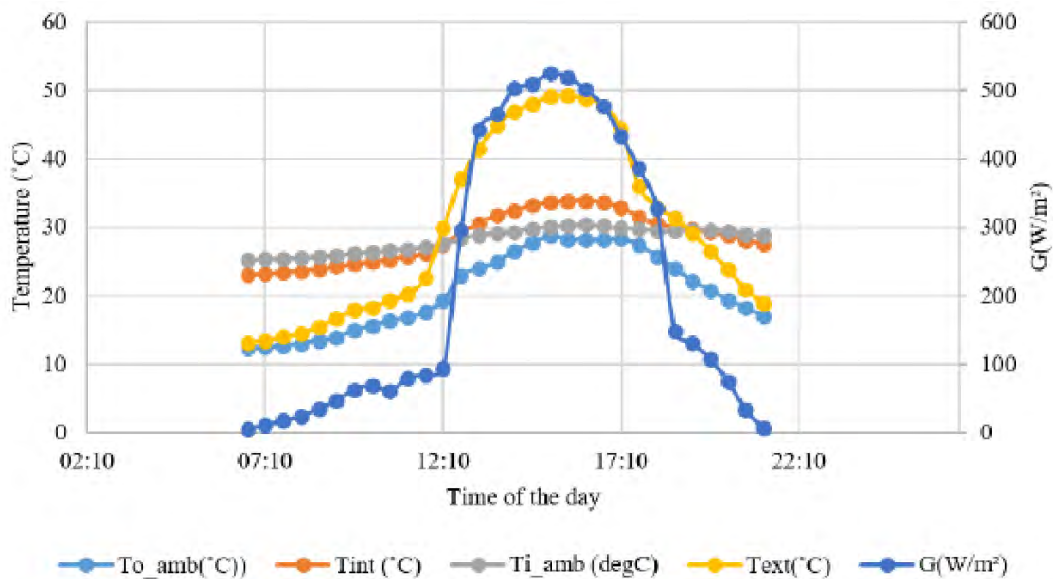


Figure 5. Variation in the external glazing surface temperature (Textl), internal glazing surface temperature (T_int), Outdoor ambient temperature (To_amb), indoor ambient temperature (Ti_amb) and solar radiation with time of the day.

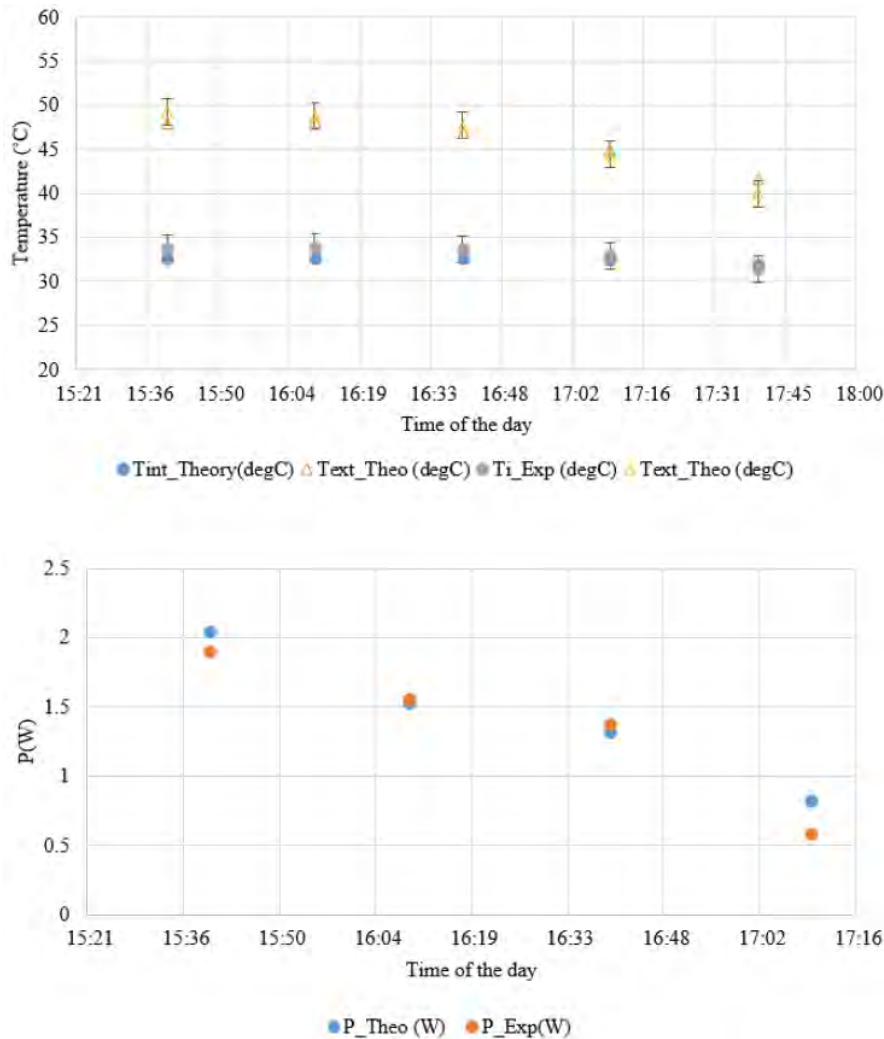


Figure 6. Top: Outdoor Experimental and Theoretical Curves for the Glazing surface temperatures (Tint) for the internal surface and (Text) for the external surface and bottom: Power produced per for 0.4 m x 0.4 m prototype as per time constant of the PV VG-4L with time of the day.

radiation, a fraction was converted into electrical energy meanwhile the rest was wasted in the form of heat. This heat act as the secondary heat source (q_2) due to the PV element. However, the vacuum layer behind the PV component of the PV VG-4L act as the insulation layer or barrier to the heat flow of (q_2) from being transferred indoors. As a result, the external surface temperature of the PV VG-4L became higher compared to its internal surface temperature, which is an advantage in the summer. For the data analysis, all the data was recorded for every 1 minute.

The outdoor experimental results as discussed previously, were compared with the theoretical results using the developed mathematical model. Due to the varying condition of the ambient climate, the electrical performance and thermal characteristics of PV VG-4L in a steady state condition are analysed as per time constant of the PV VG-4L. From our analysis, it is concluded that the computed time constant for the PV VG-4L is approximately 30 minutes.

The experimental results were compared based on the PV VG-4L surface temperature difference and electrical performance at quasi-steady state during the day and thermal transmittance or U-value during the night. Based on local weather data, the average wind speed during the day and night were approximated at 4.6 m/s and 3.5 m/s respectively. In the modelling, the dependency of the thermal and hence electrical performance of the PV VG-4L with the incident angle value which changes with the location and time of the day are being considered. The comparisons between the outdoor experimental and theoretical results are represented in Figure 6 and Figure 7 for the reading during the day and night respectively. The trend given by both outdoor experimental and theoretical curves are in good agreement. Figure 6 shows that the maximum power produced at average solar radiation of 500 W/m² is approximately 12 W/m² for 0.4 m x 0.4 m PV VG-4L made of amorphous silicon solar cells. It is worth emphasizing that, a different power produced is expected when a different type of thin film PV is

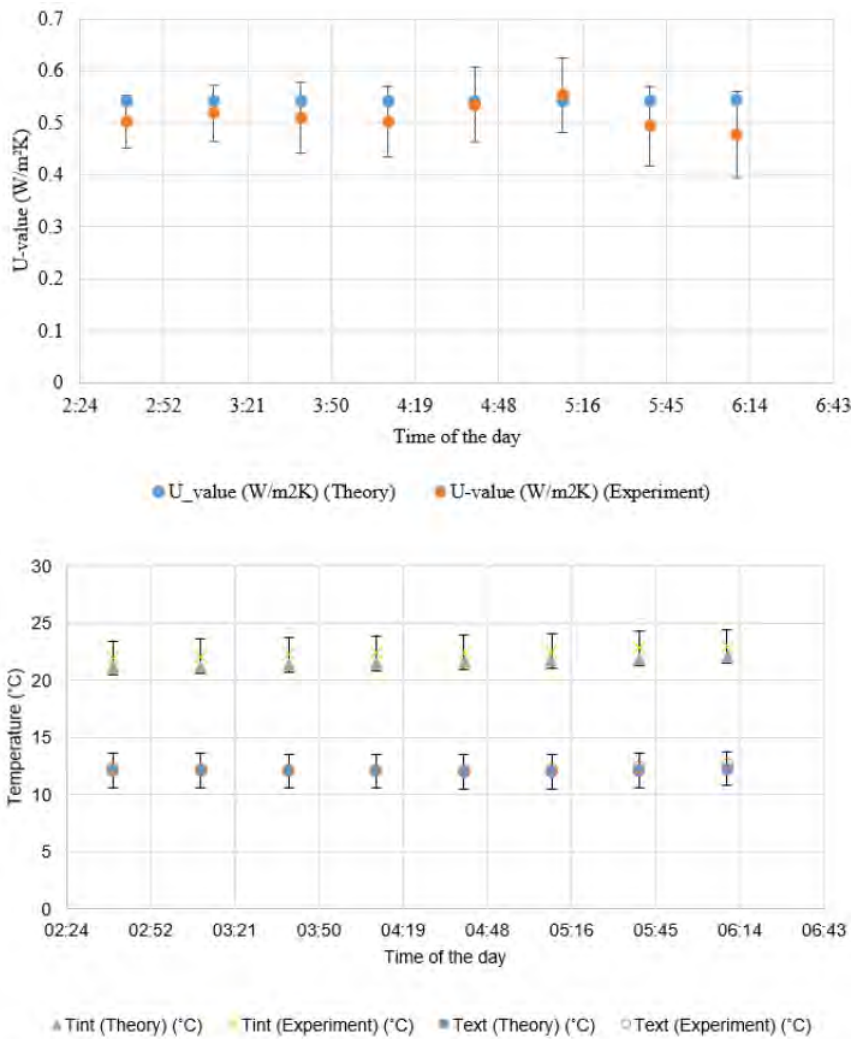


Figure 7. Top: Outdoor Experimental and Theoretical Curves for the Glazing surface temperature and bottom: U-value for 0.4 m x 0.4 m prototype as per time constant of the PV VG-4L with the time of the day (data was taken on the 27th of June 2019 at low-zero solar radiation).

used as the prototype. In order to further justify the validity of the mathematical model, error analysis using RMSPD analysis was performed. The average RMSPD for the glazing surface temperatures, the power produced and U-value are 2.58 %, 1.4% and 6.86 % respectively. It is worth noting that the derived absolute errors for the power produced are too small to be included in the plotted curves.

Angle Dependence Solar Direct Transmittance

When the PV component of the PV VG-4L absorbed solar radiation, a fraction will be wasted in the form of heat which then reemitted or reradiated into the building internal space. This secondary heat source q_i factor when combined with the solar direct transmittance τ_e the glazing will give us the solar heat gain coefficient or solar gain factor (g-value) given in equation (12).

$$g(\theta) = \tau_e(\theta) + q_i(\theta)$$

However, it is very important to emphasize that, τ_e is solar angular dependence which means, the value will change according the sunny hours and hence the angle of the solar incidence θ onto the PV VG-4L. Other than the solar heat gain coefficient, τ_e is also important to compute

Table 4. The angular dependence solar direct transmittance $\tau_e(\theta)$

The angle of solar incidence ϑ	Angular dependence solar direct transmittance $\tau_e(\vartheta)$
0	22.0
10	21.8
20	21.6
30	21.3
40	21.1
50	19.6
60	18.7
70	15.1

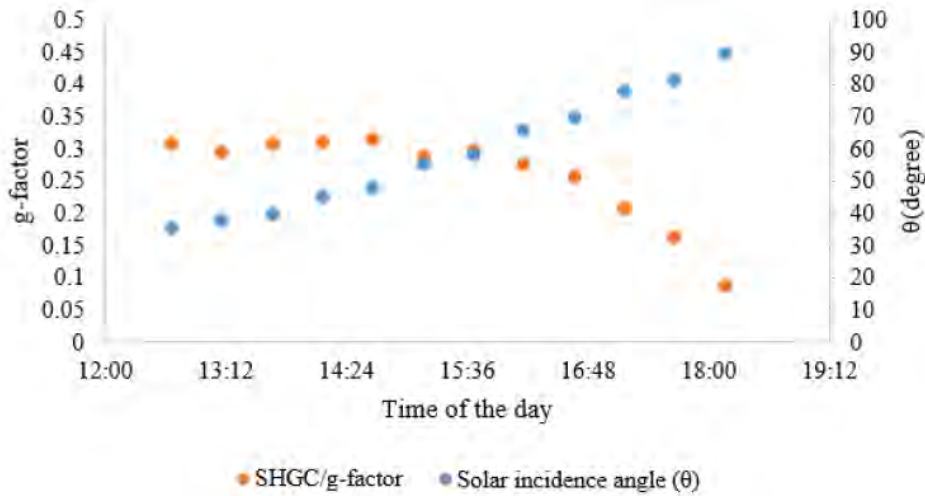


Figure 8. Obtained solar gain factor (g-factor) and the angle of incidence with time of the day.

the total amount of solar radiation absorbed by the different element of the PV VG-4L namely S_{g1} , S_{g2} , and S_{TP} , in the above discussed mathematical model. Using the EDTM SS2450 solar spectrum meter [10], the normal incidence solar direct transmittance $\tau_e(0)$ of the PV VG-4L was measured as 22%. However, due to the limited information on the angular dependence solar direct transmittance $\tau_e(\theta)$, the study conducted by [11] was being referred to estimate $\tau_e(\theta)$ and the values summarised in Table 2.

In addition, the direct solar absorptance of the a-Si of PV VG-4L $\alpha_e(\theta)$ which is given by $1 - \tau_e(\theta) - \rho_e(\theta)$ where $\rho_e(\theta)$ is the angular dependence reflectance is also assumed to follow the trend of the $\tau_e(\theta)$. This is because, $\rho_e(\theta)$ increases with the increase in the angle of solar incidence, as concluded in [11]. Since we could measure $q_i(\theta)$, we could calculate $g(\theta)$ that also changes with time of the day. At time when the solar incidence angle is low, high heat gain of approximately 30% was obtained, with τ_e of 21.22%, the fraction of the solar energy absorbed by the PV module which is being re-emitted inside the building is almost 9%.

Table 4. The angular dependence solar direct transmittance $\tau_e(\theta)$

The angle of solar incidence θ	Angular dependence solar direct transmittance $\tau_e(\theta)$
0	22.0
10	21.8
20	21.6
30	21.3
40	21.1
50	19.6
60	18.7
70	15.1

Building Thermal Load Calculation using a Simplified Energy Balance

With the validated mathematical model, building heating load performance when retrofitted with and without PV VG-4L based on the model of the Nottingham H.O.U.S.E [12] was calculated and compared. The calculation method used in this study is based on ISO 52016-1:2017 standards [13]. In general, the energy need by the building is calculated by using the energy balance quasi-steady-method as in equation (1). The total heat load of a building Q_{load} can be calculated by considering the total heat gains for the heating mode Q_{gain} hourly and the gain utilization factor:

$$Q_{load} = Q_{loss} - \eta_{utilisation} Q_{gain} \quad (13)$$

In any building, the heat loss from the building happened via heat transmission through external walls, top roof, the floor of the ground floor, windows and doors. The following equation represents the general equation to calculate the heat loss from a building:

$$Q_{loss} = U_{cH} \cdot A_{cH} (T_{indoor} - T_{ambient}) + Q_v \quad (14)$$

Table 5. Component of the house and the associated U-Value and Area.

Component	U-Value (W/m ²)	Area (m ²)
<i>Window</i>		
PV_SG	4.67	
PV_DG	2.8	25.83
PV_VG	0.60	
<i>Block wall</i>		
Floor	0.1	53.30
Roof	0.13	54.50
Skylight	0.46	3.90
Door	0.16	2.08

of which, Q_v is the ventilation heat loss, U_{ch} and A_{ch} are the heat lost coefficient and surface area of the component of the house summarized as in Table 6 [12]:

Meanwhile, the total heat gain Q_g of the house is calculate by considering both solar heat gain Q_{SHG} from the glazing component of the house and also the internal heat gain Q_{IHG} . The total solar heat gain Q_{SHG} is calculated using the following equation

$$Q_{SHG} = SHGC \times (G_{\text{global solar radiation}}) \quad (15)$$

Meanwhile, to calculate Q_{IHG} , the following assumptions are considered; i) There are two occupants in the house, ii) all equipment were assumed to be energy efficient and iii) lighting was assumed to be provided by low-energy compact florescent bulbs. The important values in regard to the latent and sensible heat generated by the spaces in the house are summarised in Table 6 [12], :

Equation 5.25 from page 5-17 of Guide A: Environmental Design – CIBSE [14] is being referred to calculate Q_{IHG} and hence the following equation was developed in this study:

$$Q_{IHG} = (Q_{\text{kitchen}} \times t_{\text{kitchen}} + Q_{\text{diningroom}} \times t_{\text{diningroom}} + Q_{\text{livingroom}} \times t_{\text{livingroom}} + Q_{\text{bedrooms}} \times t_{\text{bedrooms}} + Q_{\text{circulation}} \times t_{\text{circulation}} + Q_{\text{toilet}} \times t_{\text{toilet}} + Q_{\text{people}} \times t_{\text{people}}) \times \frac{1}{24} \quad (16)$$

Table 6. Important values in regard to the latent and sensible heat generated by the spaces in the house.

Space	Sensible heat (W/m ²)	Latent heat (W/m ²)	Average sensible equipment gained (W/m ²)	Thermal loads due to lighting (W/m ²)
Kitchen	3.8	1.9	0.5	0.5
Dining room	5.2	2.6	0.5	0.5
Living room	5.0	2.5	0.6	0.6
Bedrooms	4.9	2.4	0.25	0.25
Circulation	1	0.5	0.25	0.25
Toilet and bathroom	1.9	0.95	0.15	0.15

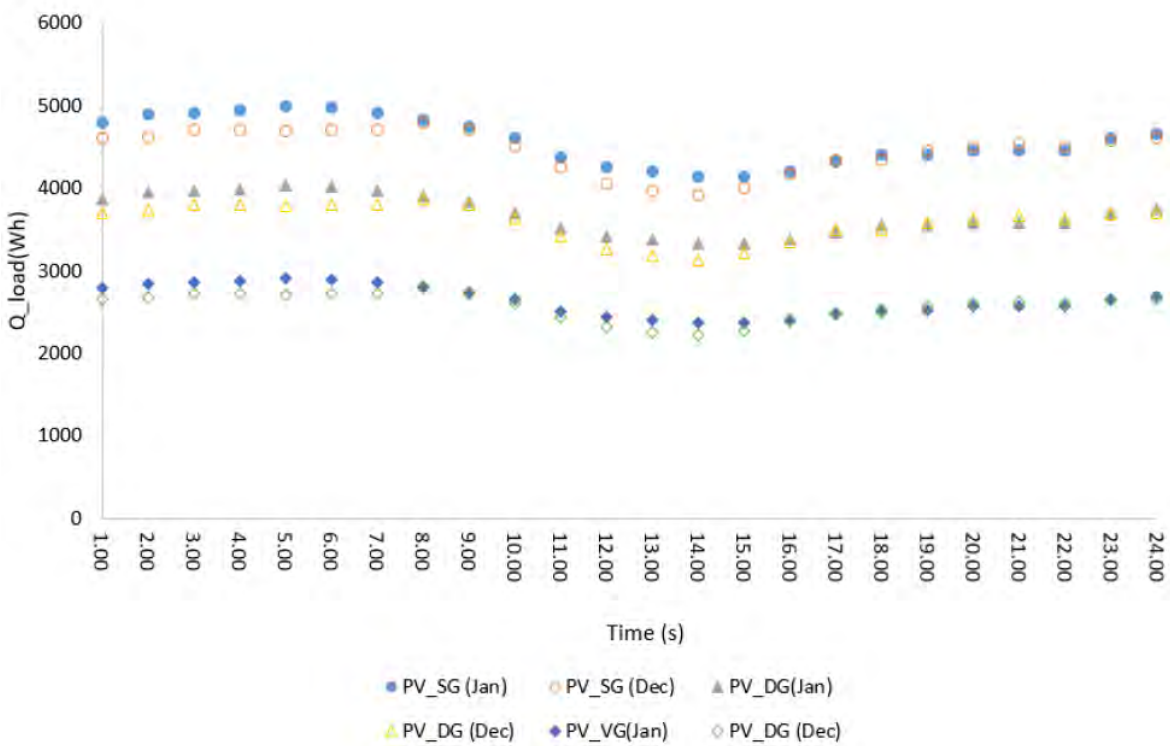


Figure 9. Predicted hourly averaged heat load in January for the a-Si (40%) type thin film PV glazing on its own (PV_SG), in double glazing (PV_DG) and vacuum glazing (PV_VG).

The energy balance equations developed to calculate the total heat load were written in MATLAB to compute the results. As shown in the figures below are the hourly average analysis of the heat load from December to March, for Nottingham, UK weather data. From the analysis, one can estimate the amount of the heat load when the thin film PV glazing installed on its own (PV_SG), with double glazing (PV_DG) and with vacuum glazing (PV VG-4L). The analysis was explicitly analyzed into two time windows. The first is from 10:00 a.m. to 4:00 p.m. and the second is from 4:00 p.m. to 10:00 a.m. where the SHCG is assumed negligible.

Based on the model of the Nottingham H.O.U.S.E, the building heat load was modelled, and the carbon emission was estimated. In comparison to the thin film PV glazing on its own i.e. PV_SG, the reduction in the amount of the building heat load by almost 50% is possible with the use of vacuum glazing (PV_VG). It is worth noting that, the PV_VG can generate power for the LED, florescent lights and appliances installed in the building. In addition, unlike conventional opaque PV panels. PV-vacuum glazing allows day lighting.

CONCLUSION

An integrated semi-transparent thin film photovoltaic glazing with vacuum insulated layer (PV VG-4L) is presented in this paper. A mathematical model was developed by taking into account all the parameters related to the individual component of a typical vacuum glazing unit which is the dominant in the design and also the fraction the solar radiation absorbed by the different layers of PV VG-4L. To validate the mathematical model, a lab-scale prototype was manufactured and tested indoors using a calibrated hot box, and outdoors by installing the sample at a research house. From the indoor analysis, the computed RMSPD value for the glazing surface temperature and the U-value are 4.75 % and 0.96% respectively. Meanwhile, when investigated under real conditions (field testing), the RMPSD computed for the glazing surface temperatures, electrical power generated under real conditions and U-value are 2.58 %, 1.4% and 6.86 % respectively. The validated mathematical model would allow us to further carry out optimisation and performance analysis of the PV VG-4L under various environmental condition which will be explored in the future. Under controlled conditions, by following closely the ISO 12567 standards, the overall U-value of the PV VG-4L was measured to be as low as 0.6 W/m²K. When investigated under real conditions, an obvious trend in glazing surface temperature variation with solar radiation was obtained. During low to zero solar radiation, the internal glazing surface temperature is on average higher in comparison to the external glazing surface temperature. However, as the

solar radiation increases, the by-product of the absorbed heat by the thin film PV glazing layer, has led to the increase in the external glazing surface temperature as the heat transfer from the secondary heat source to internal surface is reduced by the vacuum layer. Nevertheless, the heat gain into the internal building or space area was still measurable due to the solar transmittance of the PV VG-4L. At average solar radiation of 500 W/m², the PV VG-4L can in total of 12 W of power per m² of panel. Meanwhile, as shown in Figure 7, at low to zero solar radiation (i.e. during the night), at outdoor ambient temperature of 14°C, the average U-value of the typical PV VG-4L was found to be as low as 0.54 W/m²K. For a conventional thin film PV glazing, to improve the thermal performance of the thin film PV glazing, a combination with a double-glazing unit is possible with the estimated U-value of 2.5-2.8 W/m²K depending on the type of gas used to provide the insulation in the air gap. Clearly, the vacuum layer introduced in the PV VG-4L design presented in this paper is better in performance with the slim configuration of the glazing unit as an additional benefit. The results also show that the PV VG-4L not only can produce power but also has high insulation properties when compared to a single thin film PV glazing with a typical U-value of approximately 5 W/m²K; the U-value is higher by almost 90%. The promising U-value implies its range of potential applications can be improved depending on the energy needs and applications, such as for BIPV solar façade (PV curtain walling) in commercial buildings, greenhouses, skylight and conservatory.

ACKNOWLEDGEMENT

The authors gratefully acknowledge Innovate UK's financial support through Newton Fund (Project reference no: 102882) and International Science & Technology Cooperation Program of China (No. 2016YFE0124300).

References

1. IEA. Buildings Tracking Clean Energy Progress 2019; Available from: <https://www.iea.org/tcep/buildings/>.
2. Markets, R.a. \$7 Bn Building Integrated Photovoltaics (BIPV) Market - Global Outlook and Forecast 2019-2024. 2019 [cited 2019 14 October]; Available from: <https://www.globenewswire.com/news-release/2019/02/08/1713914/0/en/7-Bn-Building-Integrated-Photovoltaics-BIPV-Market-Global-Outlook-and-Forecast-2019-2024.html>.
3. Martin-Chivelet, N., et al., Comparative Performance of Semi-Transparent PV Modules and Electrochromic Windows for Improving Energy Efficiency in Buildings. *Energies*, 2018. 11(6): p. 1526.
4. Liu, H.-M., et al., Improving the Performance of a Semitransparent BIPV by Using High-Reflectivity Heat Insulation Film. *International Journal of Photoenergy*, 2016. 2016: p. 15.
5. Zhang, W., L. Lu, and X. Chen, Performance Evaluation of

- Vacuum Photovoltaic Insulated Glass Unit. *Energy Procedia*, 2017. 105(Supplement C): p. 322-326.
6. Ghosh, A., S. Sundaram, and T.K. Mallick, Investigation of thermal and electrical performances of a combined semi-transparent PV-vacuum glazing. *Applied Energy*, 2018. 228: p. 1591-1600.
 7. Schott, T. Operational temperatures of PV modules. in 6th PV solar energy conference. 1985.
 8. Evans, D., Simplified method for predicting PV array output. *Solar Energy*, 1981. 27: p. 555-560.
 9. JARIMI, H., et al. An affordable small calibrated hot box suitable for thermal performance measurement of a glazing unit. in 17th International Conference on Sustainable Energy Technologies 21st to 23rd August 2018. 2018. Wuhan, China.
 10. EDTM. EDTM SS2450 | Solar Spectrum Meter. 2019 [cited 2019 14 July 2019]; Available from: <https://www.edtm.com/index.php/ss2450-solar-spectrum-meter>.
 11. Moralejo Vázquez, F.J.a.M.C., Nuria and Olivieri, Lorenzo and Caamaño Martín, Estefanía Optical characterisation of semi-transparent PV modules for building integration., in 29th European Photovoltaic Solar Energy Conference and Exhibition (EU PVSEC 2014). 2014: Amsterdam, The Netherlands. . p. 1-9.
 12. Liu, L., Investigation on solar/thermoelectric collector for building application, in Department of Architecture and Built Environment. 2014, University of Nottingham: UK.
 13. Bsi, BS EN ISO 52016-1:2017 Energy performance of buildings. Energy needs for heating and cooling, internal temperatures and sensible and latent heat loads. Calculation procedures. 2017.
 14. CIBSE, GVA/15 CIBSE Guide A: Environmental Design 2015. 2015: CIBSE. 402.

Investigation of the Chitosan Immobilized Eggshell for the Biosorption of Brilliant Blue R Dye

Buket Bulut Kocabas¹  Ilknur Tosun Satir² 

¹Yildiz Technical University, Department of Chemistry, Istanbul, Turkey

²Hitit University, Department of Chemistry, Corum, Turkey

ABSTRACT

The biosorption method for controlling water pollution can be considered as an alternative method for the pollution of synthetic paints. In this study, the removal of Brilliant Blue R (BBR) dyestuff, which is a textile dyestuff, by biosorption is investigated. For this purpose, eggshell immobilized with chitosan (ESIC) is designed as a biosorbent. The biosorption mechanism was studied in batch and continuous mode. As far as the batch system is concerned, the following results have been obtained: The optimum pH 2, dye concentration 25 ppm, interaction time 60 minutes, biosorbent amount 2.0 g/L, removal real wastewater 53.28%. Regarding continuous systems, the following flow speed of 0.5 mL/min, biosorbent amount 2.0 g/L, removal real wastewater 91.01%. Also, recycle experiments showed that there was 24.11% loss in the biosorption capacity of ESIC for BBR dye after 7 times reuse. Obtained results were consistent with Langmuir and Freundlich isotherm models. All the results demonstrate that ESIC is a natural, recyclable and cost-effective biosorbent for BBR dye removal in wastewater.

Keywords:

Biosorption; BBR; Eggshell; Chitosan; Dye.

INTRODUCTION

Since dyes are colored compounds, they are one of the most easily recognizable contaminants in the environment. These compounds are found in many areas of the industry like: textile, color photography, cosmetics, paper, printing, plastic, food, etc. for product coloring (1-4). The fact that dye is poisonous reveals how important it is to remove dye from wastewater in terms of ecology (5, 6).

The discharge of dyes is carried out using a variety of methods such as biological degradation, membrane technologies, coagulation-flocculation, electrochemical techniques, advanced oxidation, chemical flocculation and precipitation, electrochemical, membrane filtration, ion exchange, aerobic, anaerobic and biosorption methods (7-9). Apart from these methods, the biosorption technique has been very popular in recent years in terms of chromatographic processes (10, 11).

For the first time, the adsorption method was introduced by Scheele in 1773 and Abbe Fontana in 1777 (12). Adsorption can be defined as the increase of surface concentration by attaching atoms, ions, and molecules to a solid surface (13). Several different natural and waste adsorbents have been investigated to remove

many pollutants by adsorption (14, 15). Biosorption is defined as the collection of selected ions on biomass (16). Biosorption is also the most promising technique for removing dyes in terms of simplicity, cost-efficiency, and insensitivity to toxic environments (17-19).

Chitosan is a substance found naturally in the exoskeleton of insects and in the shell of the mushroom cell walls of shellfish. Chitosan is a polysaccharide widely present in nature. It has a high number of hydroxyl and amino groups in the structure due to the repeating β - (1 \rightarrow 4) - linked glucosamine groups. Due to its advantageous properties of being nontoxic and enzymatically biodegradable chitosan is widely used in pharmaceutical and medical, wastewater treatment, biotechnology, cosmetics, food processing, agriculture and textile industries (20-22).

Eggshell is a natural material consisting of approximately 7000-17000 pores and calcium carbonate (23, 24). The fact that the eggshell is biodegradable, inexpensive and abundant material, it is an ideal alternative biosorbent, especially as the discharge of dyes and harmful inorganic ions. In addition, egg shell's natural porosity

Article History:

Received: 2019/09/18

Accepted: 2019/12/04

Online: 2019/12/31

Correspondence to: Ilknur Tosun Satir,
Hitit University, Chemistry, 19040, Corum,
TURKEY

E-Mail: ilknurtosun@hitit.edu.tr

Phone: +90 530 656 16 03

Fax: +90 364 227 7005

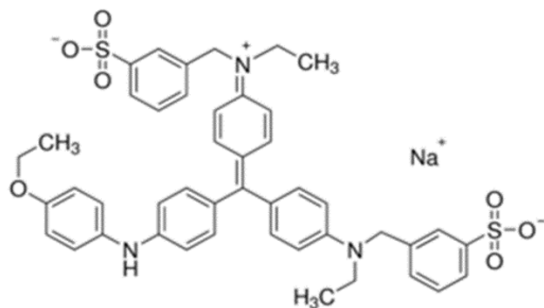


Figure 1. Chemical Structure of Brilliant Blue R Dye.

and high adsorptive capacity enable it to be an effective biosorbent to discharge dye from wastewater (25, 26).

In this study, biosorption of BBR dye known as textile dyestuff was analyzed onto ESIC biosorbent from wastewater. Effects of biosorbent amount, contact time, initial pH, adsorbate amount, the effect of different ion, temperature, biosorption-desorption cycle were studied via a batch system and flow rate, amount of biosorbent and real wastewater were studied in the continuous system. The biosorption of ESIC was investigated with different kinetics and isotherm models. In addition, BBR dye removal was analyzed in real wastewater taken from a factory in Corum.

MATERIAL AND METHODS

Preparation of ESIC

Chitosan biopolymer used in the studies was purchased from Sigma-Aldrich and Eggshell was obtained from a local market. The eggshells were washed several times with distilled water to remove impurities and then dried in an oven at 40 °C. The laboratory mill was used to grind the eggshells. Eggshell powders and chitosan were mixed with a 1:1.5 mass ratio and homogenized in 75 mL 5% (v/v) solution of acetic acid. The obtained suspension was injected into 500 mL 0.5 M solution of NaOH and eggshell-chitosan particles were washed several times with pure water and dried for 24 hours at 50°C. A grinder was used to obtain dried particles with a size below 150 µm (27).

Dye Solutions

In this study, an acidic Brilliant Blue R (BBR) dye was used. Its molecular weight is 825.96652 g/mol and the molecular formula is $C_{45}H_{44}N_3NaO_7S_2$. Fig. 1 shows the chemical structure of Brilliant Blue R (BBR) dye. The concentration of the dye solutions used in the study ranged between 50-1000 mg/L. For the adjustment of their pH 0.1 M HCl and 0.1 M NaOH solutions were used.

Biosorption Experiments

Firstly, the effect of different parameters was investigated in the batch systems. Those parameters are the biosorbent mass, interaction time, ionic strength, pH (between 1–10), temperature and dye concentration. For the pH, 0.1 g of biosorbent was added to a 50 mL 25 mg/L solution of dye and the mixture was stirred for 60 minutes at 200 rpm. After centrifuging the mixture of the dye and the biosorbent at 3000 rpm for 5 minutes, solid and liquid phases were separated. Absorbances at 586 nm wavelength were measured in order to determine the amount of the dye. The optimum biosorbent dosage between the range of 0.2 - 8.0 g/L was investigated. Interaction time was studied at 3 different temperatures (25, 35 and 45°C) in 5-90 minutes. So as to designate the effect of ionic strength on biosorption, it was adjusted using sodium chloride (NaCl) between 0.02 and 0.5 M.

BBR biosorption onto ESIC in aqueous media was performed also in a continuous system. It was supported with glass-wool placed on biosorbent in a column. A peristaltic pump was used to provide solution flow. Biosorbent amount and flow rate were studied in a continuous system. Besides, BBR biosorption from real wastewater was investigated in a continuous system.

Data Evaluation

The following equation was used to find the biosorption capacity, q_e (mg/g);

$$q_e = v \frac{(c_0 - c_e)}{m} \quad (1)$$

In the formula,

c_0 (mg/L): The starting concentration of dye,

c_e (mg/L): The dye concentration after biosorption,

v (L): The volume of biosorption setting,

m (g): The biosorbent amount.

RESULTS AND DISCUSSION

The Effect of pH at Batch System

The study was carried out with solutions having different pH values (from 1 to 10) since pH is a quite effective parameter in biosorption studies and Fig. 2 shows the results.

The biosorption capacity of the ESIC was high at low pH (maximum biosorption at pH=2) but decreased at pH

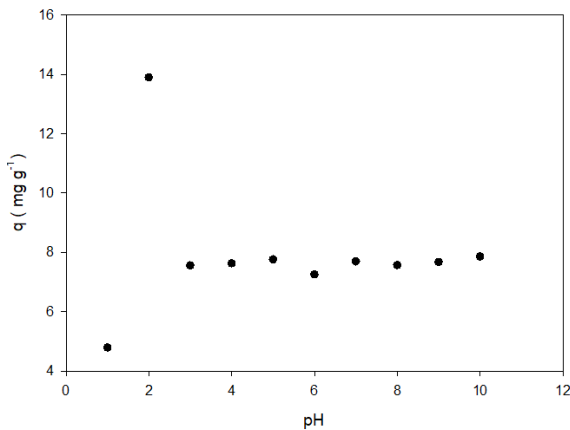


Figure 2. Investigation of pH on biosorption.

values higher than 4. This result is due to the positive charge of the surface at lower pH values and a negative charge at higher values. At pH = 2, the hydronium ions present in the medium excessively forming hydrogen bonds with the oxygen in the SO₃- group on BBR. The capacity of the biosorption showed a decrease at pH = 1. This result may be because of the dissolution of ESIC at high pH values. When the results are examined, it can be said that pH = 2.0 is the optimum value for BBR biosorption with ESIC.

The Effect of Biosorbent Amount at Batch System

Different ESIC amounts ranging between 0.2 – 8.0 g/L were used to reveal the effect of the biosorbent amount on the yield. Fig.3 shows the obtained results.

The biosorption yield increases from 0.88% to 95.73% by increasing the % removal rate of the biosorbent from 0.2 g/L to 4.0 g/L and it was found almost constant for the amounts of biosorbents greater than 2.0 g/L. An increase of biosorption efficiency was observed as the biosorbent dosage increased since the area of the surface and the possible binding sites increased (28, 29). Thus, 2.0 g/L biosorbent amount was determined as optimum.

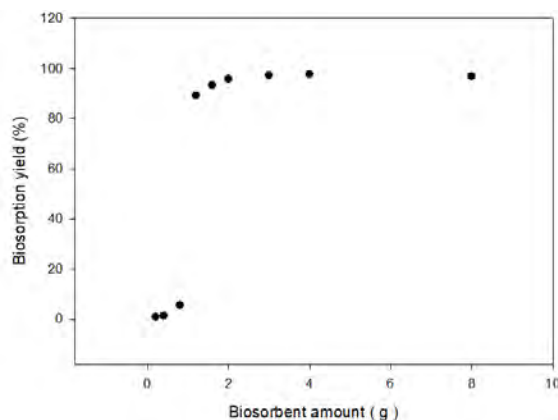


Figure 3. Investigation of biosorbent amount on biosorption.

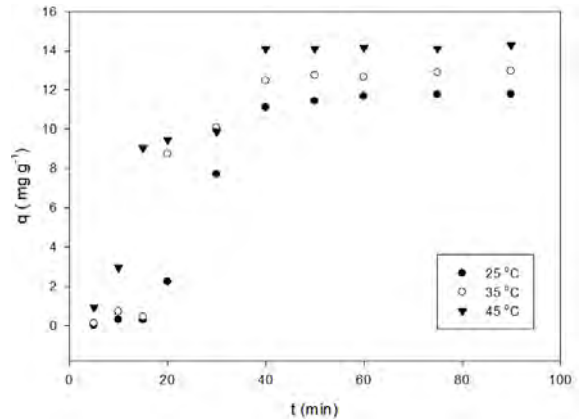


Figure 4. Investigation of interaction time and temperature on biosorption.

The Effect of Interaction Time and Temperature at Batch System

Different interaction times changing between 5 to 90 min were applied at three changing temperatures (25, 35 and 45 °C) to observe the effect of change in time and temperature on BBR biosorption. Fig.4 shows that as the contact time increased, the biosorption capacity increased and then reached a constant value. The biosorption equilibrium was reached at 60 min at all three temperatures. The biosorption capacities were found to be 11.67 mg/g for 25 °C, 12.65 mg/g for 35 °C and 14.16 mg/g for 45 °C.

Biosorption Kinetics

To determine the mechanism of the chemical reaction of the biosorption in the study, time-dependent data were evaluated by the pseudo-first-order (PFO) and pseudo-second-order (PSO) kinetic and intraparticle diffusion models.

According to Lagergren's PFO kinetic model (30), the rate of biosorption is linearly correlated to the number of vacancies on the biosorbent surface. According to this assumption, the relationship between the biosorption capacity and the duration of contact is given by the equation below.

$$\frac{dq_t}{dt} = k_1(q_e - q_t) \quad (2)$$

In this formula:

q_e (mg/g): The biosorbed dye amount at equilibrium,

q_t (mg/g): The biosorbed dye amount at time t,

k_1 (1/min): The rate constant for PFO model.

Taking advantage of this equation, when the values of $\ln(q_e - q_t)$ are plotted against t, the slope is $-k_1$ and the break-

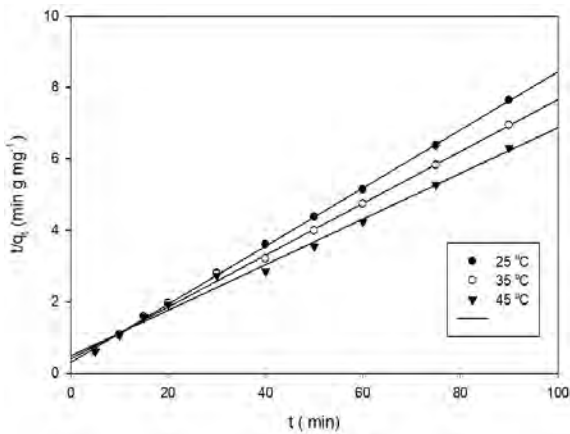


Figure 5. PSO kinetic models for BBR biosorption.

point is $\ln q_t$. The r^2 values, which represent the linearity of the graph, should be close to 1.

$$\frac{t}{q_t} = \frac{1}{k_2 q_e^2} + \frac{1}{q_e} t \quad (3)$$

is the linear expression of the equation.

Ho's PSO kinetic model of (31) is a model favored according to several investigators because it is simple and reasonable for representing the experimental results. The following equation expresses this kinetic model.

$$\frac{dq_t}{q dt} = k_2 (q_e - q_t) \quad (4)$$

In this formula:

k_2 (g/mg.min): The rate constant for a PSO kinetic model,

q_t (mg/g): The biosorbed amount of dye at time t ,

q_e (mg/g): Maximum biosorption capacity.

When this model is applied, the experimentally calculated t/q_t values are plotted against t . As can be seen from Table 1, the r^2 values of the PSO kinetic model studies are between 0.991 and 0.999 depending on the temperature. The obtained data show that the variation in this range is

Table 1. Biosorption kinetic parameters of BBR onto ESIC.

Temperature (°C)	PFO			PSO			intraparticle diffusion		
	k_1 (1/min)	q_e (mg/g)	R^2	k_2 (g/mg.min)	q_e (mg/g)	R^2	k_p (mg/g.min ^{1/2})	C (mg/g)	R^2
25	7.0×10^{-2}	7.86	0.892	2.18×10^{-2}	12.345	0.999	0.495	7.660	0.914
35	8.6×10^{-2}	9.924	0.892	1.29×10^{-2}	13.888	0.997	0.698	7.078	0.921
45	11.6×10^{-2}	21.37	0.820	8.23×10^{-3}	15.87	0.991	0.994	6.445	0.884

linear, while the q_e values are within acceptable limits, indicating that the PSO kinetic model is the most appropriate kinetic model for this study.

Weber-Morris diffusion equation is

$$q_t = k_p t^{(1/2)} + C \quad (5)$$

In this formula:

q_t (mg/g): The amount of biosorption capacity at time t ,

k_p (mg/g.dk^{1/2}): Intraparticle diffusion rate constant.

Finally, the intraparticle diffusion kinetic model was applied to the biosorption of BBR on ESIC. Values of r^2 between 0.884 and 0.921 indicate that the intraparticle diffusion kinetic model is not suitable (Table 1).

Isotherms

The results of the BBR biosorption experiment in the non-continuous system were examined with Dubinin-Radushkevich, Freundlich, and Langmuir isotherm models. The Langmuir isotherm implies that the biosorbent has a uniform structure and single-layer biosorbent occurs on the surface. After the biosorption process, the surface monolayer is coated and the amount of biosorbent material is fixed. Langmuir isotherm model (32) equation is

$$\frac{1}{q_e} = \frac{1}{q_{\max}} + \left(\frac{1}{q_{\max} K_L} \right) \cdot \frac{1}{c_e} \quad (6)$$

In the formula:

q_{\max} (mg/g): Maximum monolayer biosorption capacity,

c_e (mg/L): The amount of dye at equilibrium,

K_L (L/mol): The Langmuir biosorption equilibrium constant.

The R_L (dispersion) constant is calculated to explain the equilibrium mechanism of biosorption and in order to check if biosorption is voluntary, the following equation is

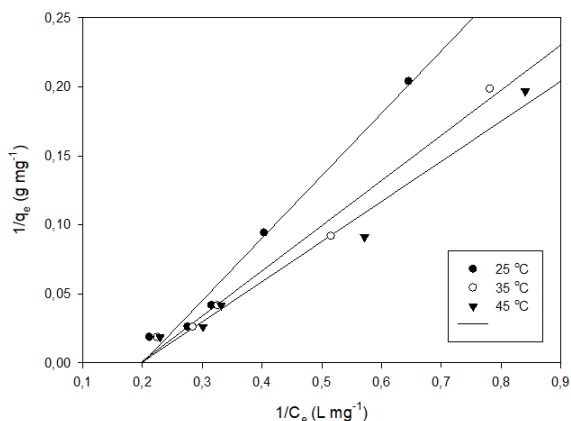


Figure 6. Langmuir isotherm for BBR biosorption onto ESIC.

used:

$$R_L = \frac{1}{1 + K_L c_0} \quad (7)$$

In the formula:

K_L (L/mg): Langmuir isotherm constant,

C_0 (mg/L): Starting concentration of the biosorbent.

Calculated R_L value between 0 and 1, shows that the biosorption takes place spontaneously (32). When r^2 values of the biosorption data in Table 2 are compared, it is seen that the BBR is in accordance with the Langmuir isotherm model on the biosorption of ESIC. This demonstrates that the biosorption process can be single-ply and homogeneous.

According to Freundlich (33), the biosorption regions on the surface of a biosorbent are heterogeneous. Thus, they consist of different types of biosorption sites. The mathematical expression of Freundlich isotherm is

$$\ln q_e = \ln K_F + \frac{1}{n} \ln C_e \quad (8)$$

In this formula:

K_F (L/g): Freundlich biosorption isotherm constant,

$\frac{1}{n}$ (dimensionless): The biosorption intensity,

q_e (m/g): Biosorption capacity at equilibrium,

C_e (mg/L): The amount of dye at equilibrium.

Usually, n as an indication of good adsorption is between 1 and 10. The value of $1/n$, which takes values in the range 0-1, is the heterogeneity factor and its value reaches to zero when the surface is more heterogeneous.

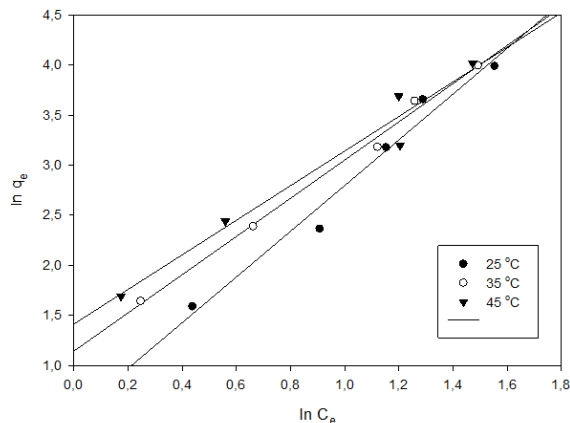


Figure 7. Freundlich isotherm for BBR biosorption onto ESIC.

According to the Freundlich isotherm model, K_F value is found between 1.673 and 4.039. When n is greater than 1, the process of biosorption is self-driven.

D-R model (34) allows to understand if the adsorption is physical or chemical. It is assumed that the energies of the eclipsed sites in this isotherm are like the Gaussian distribution. Ionic species are first connected to the energetically most suitable regions. While multi-layer biosorption occurs on these bonding ions, the D-R isotherm is calculated by the following equation:

$$\ln q_e = \ln q_m - \beta \varepsilon^2 \quad (9)$$

In this formula:

q_m (mg/g): The maximum biosorption capacity,

β : Constant gives mean free energy (E).

By applying the following equation:

$$E = -2\beta \varepsilon^{(1/2)} \quad (10)$$

To obtain the Polanyi potential ε , the following equation is used;

$$\varepsilon = RT \ln \left(1 + \frac{1}{C_e} \right) \quad (11)$$

In the formula:

T (K): The absolute temperature,

R : The gas constant (8,314 kJ/mol),

ε : The Polanyi potential.

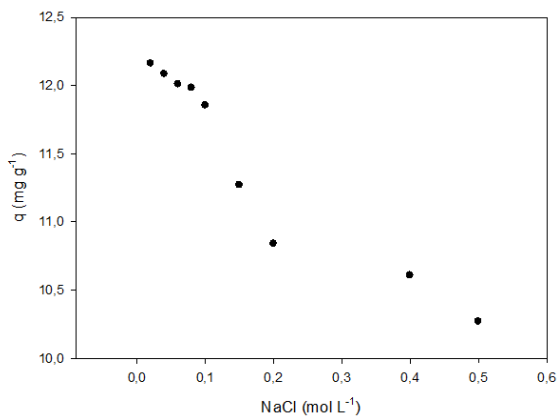
Examination of the r^2 values of the biosorption data in Table 2 reveals that the adsorption of BBR on ESIC does not conform to the Dubinin-Radushkevich isotherm model.

Table 2. Biosorption isotherm values of BBR onto ESIC.

Temperature (°C)	Langmuir				Freundlich			Dubinin–Radushkevich (D–R)			
	q_{max} (mol/g)	K_L (L/mol)	r^2	R_L	n	K_F (L/g)	r^2	q_m (mol/g)	β (mol ² /kJ ²)	r^2	E (kJ/mol)
25	11.11	19.9×10^{-2}	0.984	17.02	2.282	1.673	0.973	61.74	1.787	0.894	0.529
35	15.62	19.96×10^{-2}	0.986	7.82	1.907	3.142	0.994	55.924	1.174	0.929	0.652
45	17.54	19.96×10^{-2}	0.976	6.87	1.705	4.039	0.984	55.20	9.671	0.937	0.227

Effect of Salt

To observe the effect of salt on the biosorption, solutions were prepared to contain NaCl salt adjusted to a concentration range of 0.02–0.50 mol/L. The pH, biosorbent amount and contact time of prepared solutions were 2.0; 2.0 g/L and 60 min, respectively. The dye concentration of the solutions was chosen as 25 mg/L. Fig. 8 shows the obtained results.

**Figure 8.** Salt effect on the BBR biosorption onto ESIC.

The results show that an increase in salt concentration yields a considerable decrease in biosorption. This is due to the accumulation of other ions in the environment on the biosorbent surface.

Biosorption Thermodynamics

Gibbs free energy change ΔG° , standard enthalpy ΔH° and standard entropy change ΔS° are important thermodynamic parameters. They are used to understand the effect of temperature on the biosorption process and to determine the necessary dynamic forces. The relation between the K_L constant obtained from the Langmuir isotherm model and ΔG° is shown below:

$$\Delta G^\circ = -RT \ln K_L \quad (12)$$

As a result of the Gibbs equation with the combination of Equation 12, the relation between ΔH° and ΔS° and K_L is obtained as:

$$\ln K_L = -\frac{(\Delta H^\circ)}{RT} + \frac{(\Delta S^\circ)}{R} \quad (13)$$

In the formula:

K_L (L/mol): Langmuir isotherm constant.

The negative value of ΔG° is an indication that the reaction is exothermic as ΔH° . The entropy change ΔS° explains the irregularity of the reaction. As a result of a positive ΔS° , the irregularity of the dye molecule increases.

Thermodynamic parameters of biosorption of BBR with ESIC were evaluated by analyzing ΔG° , ΔH° , and ΔS° . K_L was used as the equilibrium constant. The thermodynamic data calculated by using the slope and the batch point of the line obtained by plotting $1/T$ against $\ln K_L$ are given in Table 3.

As seen in Table 3, free energy change has a negative value at all three temperatures. This shows that the biosorption reaction of the BBR onto the ESIC is spontaneous.

The positive change in enthalpy shows that the biosorption of BBR is endothermic. Entropy change also has a positive value enthalpy change. This indicates that the reaction mechanism increases the irregularity of the dye molecule.

Column Biosorption Studies

Flow rate, biosorbent content and actual wastewater parameters were investigated for biosorption of BBR dye in the continuous system. The effect of flow rate in a continuous system was studied by applying the rate between 0.50 mL/min and 4.00 mL/min. Fig. 9 shows the change of the biosorption capacity with the flow rate of the so-

Table 3. Biosorption thermodynamic for BBR onto ESIC.

t (°C)	ΔG° (kJ/mol)	ΔH° (kJ/mol)	ΔS° (J/K.mol)
25	-13.586		
35	-12.500	179.501	0.551
45	-2.355		

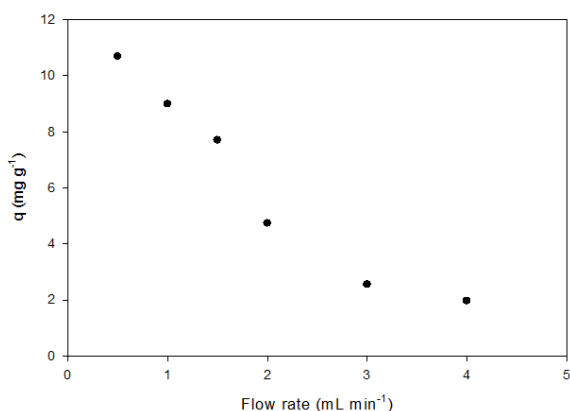


Figure 9. Flow rate change at continuous system.

lution.

An increase in flow rate significantly decreases the biosorption of BBR. The biosorption capacity at the lowest flow rate of 0.50 mL/min was determined to be 11.44 mg/g. The reason for the decrease of the biosorption capacity is the shorter contact time after increasing the flow rate. Because at high flow rates, holding the dye solution in the column becomes more difficult and the biosorption capacity decreases. However, at low flow rates, the dye solution is in contact with the biosorbent for a longer time. Thus, more dye can be removed. As a result, optimum flow rate for dye biosorption in continuous system was determined as 0.50 mL/min.

In the continuous system, dye biosorption was sought at a flow rate of 0.5 mL/min at a range of biosorbent from 0.20 g/L to 3.00 g/L. As a result of the investigated values, the change of dye removal % by the amount of biosorption is given in Fig.10.

The process was carried out by using biosorbent in different amounts in the continuous removal process of the dye. The optimum amount of biosorbent was chosen as 2.00 g/L. When the amount of biosorbent was chosen as 3.00 g/L, biosorption removal was found to approach 100%. As can be seen, BBR removal increased as the amount of biosorbent

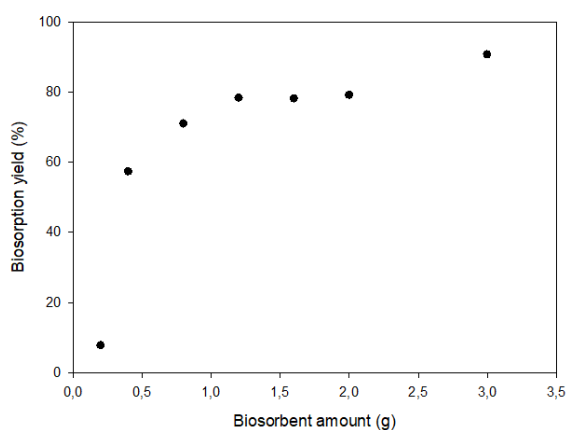


Figure 10. Change of biosorbent amount at continuous system.

increased because when the column diameter is kept constant, the column height increases along with the increase in the amount of biosorbent. The increase in column height leads to a longer contact time, which in turn causes the biosorbent and the sorbate to contact more of the column.

Characterization of the Biosorbent

SEM analysis of the ESIC used as a biosorbent in intermittent and continuous system studies has been performed to obtain information about the surface structure.

Fig. 11a shows that the surface of ESIC has a heterogeneous, rough and porous structure. Therefore, Fig. 11b shows that the surface of the ESIC biosorbent binds to different regions of the BBR.

Desorption and Reusability

After the BBR biosorption process on ESIC, cyclic desorption and reusability were investigated. The reusability of the biosorbent must be high to reduce the use of the biosorbent. Fig.12 shows the data from the biosorption-desorption cycle.

As can be seen, the biosorption-desorption cycling was

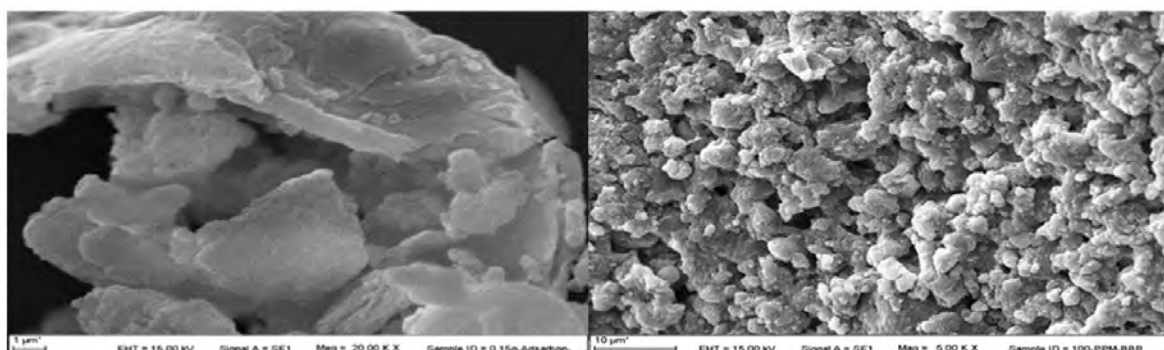


Figure 11. The SEM image of ESIC a) initial b) after biosorption.

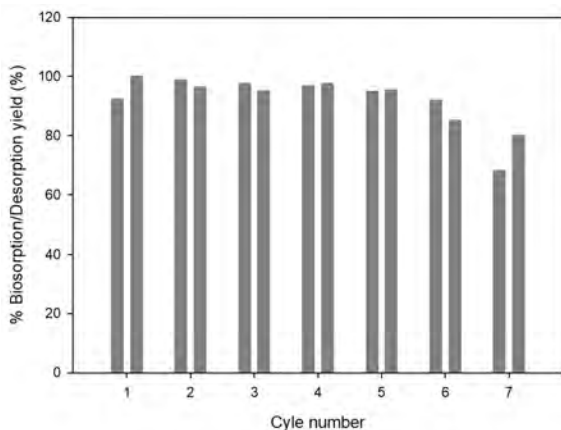


Figure 12. The reusability of ESIC.

carried out 7 times in the batch system. At the 7th cycle, a 24.11% reduction in biosorption efficiency was observed the effect was still being observed.

Application to Real Wastewater

Biosorption study with real wastewater containing 25 mg/L BBR under optimum biosorption conditions (pH = 2; 2.0 g/L biosorbent amount, 60 min contact time) determined for the removal of BBR in batch system in real wastewater conditions. The actual sample was taken from the wastewater of a factory. The biosorption process yielded 53.28 % removal of the dye. It can be seen that the ESIC biosorbent can be used reliably in industrial environment for the removal of BBR.

Working conditions for a real wastewater sample containing 25 mg/L BBR in the continuous system; pH = 2; 0.10 g of adsorbent amount; 50 mL of the dye solution and 0.50 mL/min. In this condition, the dye removal was 91.01%. These results show that BBR removal in a real wastewater environment is highly efficient.

CONCLUSION

Eggshells are inexpensive and easily available biosorbent. Because of these properties, they can be used for the removal of BBR from aqueous solutions efficiently and cost-effectively.

- With the developed biosorbent, the removal of BBR dyestuff in the real wastewater environment was carried out with high efficiency.

- For both systems, the maximum biosorption efficiency of 2.00 g/L biosorbent amount was achieved for the concentration of 25 mg/L of dye.

- In the batch system, 60 minutes of mixing time

were continuously operated and 100 minutes for the continuous system at the optimum flow rate 0.50 mL/min.

- Optimum dye removal rates for batch and continuous systems were determined as 95.73% and 78.21%, respectively.

- The % removal in the batch system remained constant by increasing the amount of biosorbent, however, it reached 100% in the continuous system. Taking all these results into consideration, it is seen that BBR in wastewater can be applied by biosorption of the removal of eggshell immobilized with chitosan.

References

1. Akar T, Tosun İ, Kaynak Z, Kavas E, Incirkus G, Akar ST. Assessment of the biosorption characteristics of a macro-fungus for the decolorization of Acid Red 44 (AR44) dye. *Journal of Hazardous Materials* 171(1) (2009) 865-871.
2. Elsherbiny AS. Adsorption kinetics and mechanism of acid dye onto montmorillonite from aqueous solutions: Stopped-flow measurements. *Applied Clay Science* 83-84(2013) 56-62.
3. Zhao X-g, Huang J-g, Wang B, Bi Q, Dong L-l, Liu X-j. Preparation of titanium peroxide and its selective adsorption property on cationic dyes. *Applied Surface Science* 292(2014) 576-582.
4. Hao OJ, Kim H, Chiang P-C. Decolorization of Wastewater. *Critical Reviews in Environmental Science and Technology* 30(4) (2000) 449-505.
5. Rauf MA, Shehadi IA, Hassan WW. Studies on the removal of Neutral Red on sand from aqueous solution and its kinetic behavior. *Dyes and Pigments* 75(3) (2007) 723-726.
6. Erol K, Köse K, Köse DA, Sızır Ü, Tosun Satır İ, Uzun L. Adsorption of Victoria Blue R (VBR) dye on magnetic microparticles containing Fe(II)-Co(II) double salt. *Desalination and Water Treatment* 57(20) (2016) 9307-9317.
7. Mao J, Won SW, Choi SB, Lee MW, Yun Y-S. Surface modification of the *Corynebacterium glutamicum* biomass to increase carboxyl binding site for basic dye molecules. *Biochemical Engineering Journal* 46(1) (2009) 1-6.
8. Moradi SE. Microwave assisted preparation of sodium dodecyl sulphate (SDS) modified ordered nanoporous carbon and its adsorption for MB dye. *Journal of Industrial and Engineering Chemistry* 20(1) (2014) 208-215.
9. Shirzad-Siboni M, Khataee A, Joo SW. Kinetics and equilibrium studies of removal of an azo dye from aqueous solution by adsorption onto scallop. *Journal of Industrial and Engineering Chemistry* 20(2) (2014) 610-615.
10. Erol K. DNA adsorption via Co(II) immobilized cryogels. *Journal of Macromolecular Science, Part A* 53(10) (2016) 629-635.
11. Erol K. Polychelated cryogels: hemoglobin adsorption from human blood. *Artificial Cells, Nanomedicine, and Biotechnology* 45(1) (2017) 31-38.
12. Greg S, Sing K. Adsorption, surface area and porosity-Academic Press, New York, 1982.
13. Juang RS, Wu FC, Tseng RL. The Ability of Activated Clay for the Adsorption of Dyes from Aqueous Solutions. *Environmental Technology* 18(5) (1997) 525-531.
14. Shen K, Gondal MA. Removal of hazardous Rhodamine dye from water by adsorption onto exhausted coffee ground. *Journal of Saudi*

- Chemical Society 21 (2017) 120-127.
15. Mittal A, Kaur D, Malviya A, Mittal J, Gupta VK. Adsorption studies on the removal of coloring agent phenol red from wastewater using waste materials as adsorbents. *Journal of Colloid and Interface Science* 337(2) (2009) 345-354.
 16. Volesky B. Biosorption and me. *Water Research* 41(18) (2007) 4017-4029.
 17. Ghaedi M, Mosallanejad N. Study of competitive adsorption of malachite green and sunset yellow dyes on cadmium hydroxide nanowires loaded on activated carbon. *Journal of Industrial and Engineering Chemistry* 20(3) (2014) 1085-1096.
 18. Shan R-r, Yan L-g, Yang Y-m, Yang K, Yu S-j, Yu H-q, et al. Highly efficient removal of three red dyes by adsorption onto Mg-Al-layered double hydroxide. *Journal of Industrial and Engineering Chemistry* 21(2015) 561-568.
 19. El-Mekkawi D, Galal HR. Removal of a synthetic dye "Direct Fast Blue B2RL" via adsorption and photocatalytic degradation using low cost rutile and Degussa P25 titanium dioxide. *Journal of Hydro-environment Research* 7(3) (2013) 219-226.
 20. Agboh O, Qin Y. Chitin and chitosan fibers. *Polymers for Advanced Technologies* 8(6) (1997) 355-365.
 21. Spulber R, Chifiriuc C, Fleancu M, Popa O, Băbeanu N. Antibacterial Activity of Magnetite Nanoparticles Coated with Bee Pollen Extracts. in "Agriculture for Life, Life for Agriculture" conference proceedings, pp.579-585, 2018 Sciendo.
 22. Knaul JZ, Hudson SM, Creber KAM. Crosslinking of chitosan fibers with dialdehydes: Proposal of a new reaction mechanism. *Journal of Polymer Science Part B: Polymer Physics* 37(11) (1999) 1079-1094.
 23. Wenming D, Zhijun G, Jinzhou D, Liying Z, Zuyi T. Sorption characteristics of zinc(II) by calcareous soil-radiotracer study. *Applied Radiation and Isotopes* 54(3) (2001) 371-375.
 24. William J, Stadelman OJC. *Egg science and technology*, fourth ed. New York, Food Products Press, 1995.
 25. Guru PS, Dash S. Sorption on eggshell waste—A review on ultrastructure, biomineralization and other applications. *Advances in Colloid and Interface Science* 209 (2014) 49-67.
 26. Saha PD, Chowdhury S, Mondal M, Sinha K. Biosorption of Direct Red 28 (Congo Red) from aqueous solutions by eggshells: Batch and column studies. *Separation Science and Technology* 47(1) (2012) 112-123.
 27. Ngah WW, Ab Ghani S, Kamari A. Adsorption behaviour of Fe (II) and Fe (III) ions in aqueous solution on chitosan and cross-linked chitosan beads. *Bioresource technology* 96(4) (2005) 443-50.
 28. Gong R, Ding Y, Li M, Yang C, Liu H, Sun Y. Utilization of powdered peanut hull as biosorbent for removal of anionic dyes from aqueous solution. *Dyes and Pigments* 64(3) (2005) 187-192.
 29. Gong R, Ding Y, Liu H, Chen Q, Liu Z. Lead biosorption and desorption by intact and pretreated spirulina maxima biomass. *Chemosphere*. 2005;58(1):125-30.
 30. Lagergren S. Zur theorie der sogenannten adsorption gelöster stoffe. *Kungliga svenska vetenskapsakademiens Handlingar* 24 (1898) 1-39.
 31. Ho Y-S, McKay G. Kinetic models for the sorption of dye from aqueous solution by wood. *Process Safety and Environmental Protection* 76(2) (1998) 183-191.
 32. Langmuir I. The adsorption of gases on plane surfaces of glass, mica and platinum. *Journal of the American Chemical society* 40(9) (1918) 1361-1403.
 33. Freundlich H. Über die adsorption in lösungen. *Zeitschrift für physikalische Chemie* 57(1) (1907) 385-470.
 34. Radushkevich MDL. The equation of the characteristic curve of the activated charcoal USSR Phys. *Chem Sect* 55(1947) 331.

Schiff Base-Pd(II) Complexes Containing Pyridine and Thiophene Rings: Synthesis, Characterization, Suzuki-Miyaura C-C Coupling Reactions

Kenan Buldurun¹  Metin Ozdemir²

¹Mus Alparslan University, Department of Food Processing, Mus, Turkey

²Mus Alparslan University, Department of Chemistry, Mus, Turkey

ABSTRACT

New Schiff base-palladium(II) complexes (1a-d) were synthesized with the reaction of Schiff base ligand and $[\text{PdCl}_2(\text{CH}_3\text{CN})_2]$. Pd(II) complexes (1a-d) were solid and stable to moisture and air. Their structures were characterized through the spectroscopic techniques including microanalysis, FT-IR, UV-Vis, proton (^1H) and carbon (^{13}C) NMR, mass spectrometry. The data obtained from the spectroscopic techniques showed that Schiff base-Pd(II) complexes 1a, 1b and 1c were formed through the coordination of azomethine nitrogen and carbonyl/hydroxyl oxygen atoms, while 1d complex coordinated only azomethine nitrogen atom of the Schiff base. All complexes were found to have square plane. In addition, Pd(II) complexes (1a-d) were investigated in Suzuki-Miyaura coupling reactions of different aryl bromides using phenylboronic acid. The reactions were carried out in a mixed aqueous EtOH/H₂O (1/3) at room temperature with K₂CO₃ as the base for 1 hour. The Pd(II) complexes (1a-d) used as catalysts exhibited perfect catalytic activity in the Suzuki-Miyaura reaction.

Keywords:

Aryl bromides; Pd(II) complexes; Schiff base; Suzuki-Miyaura; Mass spectrometry.

INTRODUCTION

Schiff bases are a multinucleated ligand group that forms complexes with many metal atoms through donor atoms. They have been extensively studied due to their important properties such as easy accessibility, low cost, selectivity and sensitivity to central metal ions [1-6]. Schiff base complexes exhibit high catalytic activities for a wide range of chemical reactions (e.g., hydrosilylation, homogenous catalyst, transfer hydrogenation, C-C coupling reactions and epoxidation) [7-9]. The Suzuki-Miyaura reaction, which is one of the present C-C cross-coupling reactions, is the most important reaction between aryl halides and arylboronic acids and widely used to obtain biaryls. The Suzuki-Miyaura coupling reaction has been extensively studied in the field of synthesis owing to its ease of operation, perfect functional group compatibility, attainable and environmental friendly properties of the initial reagents. Due to their superior properties, biaryls is a widely preferred compound in numerous industrial applications such as pharmaceuticals, natural products, agrochemicals, advanced materials, cosmetics [10-17].

In the last decade, the synthesis of Schiff base-Pd(II) complexes has gained great attention since they are cost-effective and environmentally friendly. Particularly, the studies on the catalytic application of Schiff base-Pd(II) complexes, which do not contain phosphine ligands, have increased in Heck-Mizoroki and Suzuki-Miyaura coupling reactions. The research on the synthesis and catalytic activities of Schiff bases and their transition metal complexes has been ongoing [15, 18].

In this article, four Schiff base-palladium complexes (**1a-d**) were prepared using $[\text{PdCl}_2(\text{CH}_3\text{CN})_2]$ metal salts, and their catalytic activities were investigated. The formation of Pd(II) complexes was determined through FT-IR, microanalysis, UV-Vis, ^1H and ^{13}C -NMR and mass spectrometer. The catalytic activity of (**1a-d**) complexes was examined in the Suzuki-Miyaura carbon-carbon coupling reaction. Pd(II) complexes showed excellent activity as catalysts in the Suzuki-Miyaura coupling reaction.

Article History:

Received: 2019/10/01

Accepted: 2019/12/09

Online: 2019/12/31

Correspondence to: Kenan Buldurun, Mus Alparslan University, Food Processing, 49250, Mus, TURKEY

E-Mail: k.buldurun@alparslan.edu.tr

Phone: +90 436 249 49 49

Fax: +90 436 249 13 18

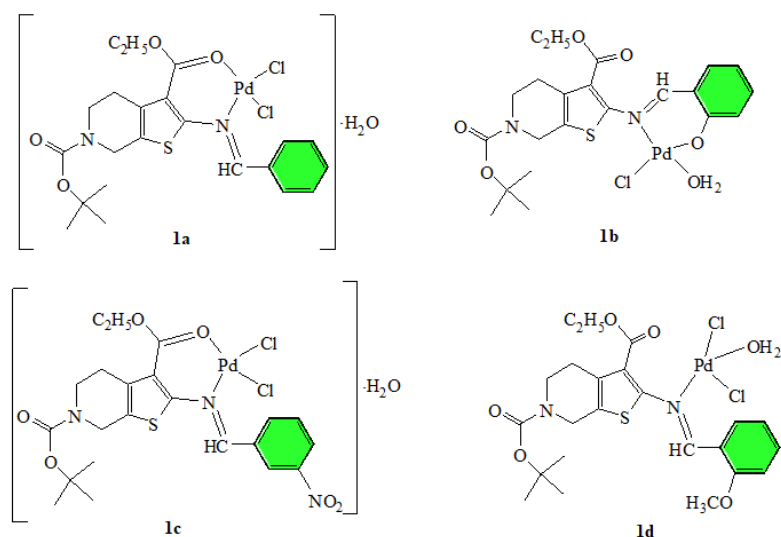


Figure 1. Synthesis of Schiff base-Pd(II) complexes (**1a-d**)

MATERIAL AND METHODS

Material and physical measurements

FT-IR spectra were performed in the range of 400-4000 cm^{-1} on a Perkin Elmer 65 spectrometer. UV-Vis spectra were performed in the range of 200-800 nm (in EtOH) on a Shimadzu-1800 spectrophotometer. Mass spectra of the complexes were measured on an Agilent 1100 MSD spectrophotometer. The NMR (^1H and ^{13}C) spectra were determined with a Bruker 300 MHz and 75 MHz. Microanalysis of C, H, N and S were determined on a CHNS-932 LECO instrument. The catalytic conversions were performed with GC-MS analysis by Agilent 7890B GC system and 5977MSD instrument. All reagents and solvents utilized were of commercial grade and without purified. All reactions were prepared under atmospheric condition.

Synthesis of Schiff base-Pd(II) Complexes (**1a-d**)

The **1a** complex was prepared in 20 mL of methanol through the reaction of (E)-6-tert-butyl 3-ethyl 2-(benzylideneamino)-4,5-dihydrothieno[2,3-c]pyridine-3,6(7H)-dicarboxylate (0.5 g; 1.2 mmol) and $[\text{PdCl}_2(\text{CH}_3\text{CN})_2]$ (0.31 g; 1.2 mmol). The mixture was stirred at boiling temperature for one day, and the solvent was completely evaporated in a vacuum. The product was crystallized from a dichloromethane/diethyl ether (1:3) mixture. The proposed structure for the Pd(II) complex is given in Fig. 1. The other three complexes **1b**, **1c**, **1d** were prepared following the same procedure as for the complex **1a**.

Anal. calcd. for $\text{C}_{22}\text{H}_{28}\text{N}_2\text{O}_5\text{SPdCl}_2$ (%): C, 43.35; H, 4.59,

N, 4.59; S, 5.25. Found: C, 43.40; H, 4.66; N, 4.65; S, 5.32. IR (KBr, cm^{-1}): 3426 (-OH), 3043 (Ar-H), 2979 (Al-H), 1679 (C=O), 1578 (CH=N), 1577, 1491 (Ar-C), 781 (C-S-C), 554, 525 (M-O), 503, 491 (M-N). $^1\text{H-NMR}$ (300 MHz, DMSO-d_6 , ppm): 8.10 (s, 1H, CH=N), 7.81-7.49 (m, 5H, ArH), 4.35, 4.20 (m, 4H, -2CH₂), 3.80-3.11 (m, 4H, CH₂ (pyridine)), 1.36, 1.20 (d, 12H, -CH₃). $^{13}\text{C-NMR}$ (75 MHz, DMSO-d_6 , ppm): 158.00, 155.00 (2C=O), 163.00 (CH=N), 136.00-130.00 (thiophenyl), 134.00-127.00 (benzene ring), 79.80 (tert-butyl), 58.96, 14.00 (-OC₂H₅), 43.00, 18.00 (pyridine), 24.01 (C(CH₃)₃). UV-Vis. (λ_{max} , nm): $\pi \rightarrow \pi^*$, 217, 225, 233; $n \rightarrow \pi^*$, 302, 384. LC-MS: m/z: 590.90 (calcd.), 590.97 (found) $[\text{M-H}_2\text{O}]^+$.

Complex **1b**: Anal. calcd. for $(\text{C}_{22}\text{H}_{27}\text{N}_2\text{O}_6\text{SPdCl})$ (%): C, 44.83; H, 4.58; N, 4.75; S, 5.43. Found: C, 44.81; H, 4.56; N, 4.62; S, 5.46. IR (KBr, cm^{-1}): 3506, 3442 (-OH), 3020 (Ar-H), 2977 (Al-H), 1685 (C=O), 1605 (CH=N), 1572, 1521 (Ar-C), 1151 (C-O), 760 (C-S-C), 565, 550 (M-O), 463 (M-N). $^1\text{H-NMR}$ (300 MHz, DMSO-d_6 , ppm): 8.80 (s, 1H, CH=N), 7.69-6.97 (m, 4H, ArH), 4.54, 4.40 (m, 4H, -2CH₂), 3.35-2.51 (m, 4H, CH₂ (pyridine)), 1.46-1.26 (d, 12H, -CH₃). $^{13}\text{C-NMR}$ (75 MHz, DMSO-d_6 , ppm): 162.70, 154.24 (2C=O), 161.61 (CH=N), 133.00-129.00 (thiophenyl), 136.00, 117.00 (benzene ring), 80.00 (tert-butyl), 61.07, 14.59 (-OC₂H₅), 44.02, 18.00 (pyridine), 28.51 (C(CH₃)₃). UV-Vis. (λ_{max} , nm): $\pi \rightarrow \pi^*$, 221; $n \rightarrow \pi^*$, 301, 391, 504. LC-MS: m/z: 553.42 (calcd.), 553.17 (Found) $[\text{M-Cl}]^+$.

Complex **1c**: Anal. calcd. for $(\text{C}_{22}\text{H}_{27}\text{N}_3\text{O}_7\text{SPdCl}_2)$ (%): C, 40.34; H, 4.12; N, 6.42; S, 4.89. Found: C, 40.31; H, 4.17; N, 6.49; S, 5.01. IR (KBr, cm^{-1}): 3434 (-OH), 3051 (Ar-H), 2982 (Al-H), 1682 (C=O), 1580 (CH=N), 1531, 1467 (Ar-C), 1385 (C-NO₂), 781 (C-S-C), 556, 516 (M-O), 493, 467 (M-N). $^1\text{H-NMR}$ (300 MHz, DMSO-d_6 , ppm): 8.32 (s, 1H, CH=N), 7.50-7.01 (m, 4H, Ar-H), 5.76, 4.19 (m, 4H, -2CH₂), 3.35-2.80

Table 1. Optimization of the reaction conditions for Suzuki coupling reaction.

Entry	Base	Time (h)	Yield (%)
1	NOH	8	64
2	CS ₂ CO ₃	8	51
3	KOH	8	67
4	K ₂ CO ₃	8	95
5	KOBu ^t	8	68
6	-	8	-
7	K ₂ CO ₃	1	95

²Reaction conditions: Phenyl boronic acid (3.0 mmol), aryl bromide (2.0 mmol), base (4.0 mmol), catalyst (0.01 mmol), EtOH/H₂O (5 mL) and 25 °C.

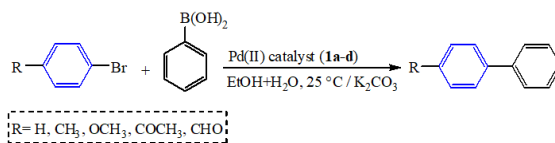
(m, 4H, CH₂ (pyridine)), 1.69-1.21 (d, 12H, -CH₃). ¹³C-NMR (75 MHz, DMSO-d₆, ppm): 165.00, 163.00 (2C=O), 159.30 (CH=N), 134.00-129.94 (thiophenyl), 129.00, 108.00 (benzene ring), 94.47 (tert-butyl), 59.50, 14.84 (-OC₂H₅), 47.00, 15.16 (pyridine), 29.16 (C(CH₃)₃). UV-Vis. (λ_{max}, nm): π→π*, 226; n→π*, 309, 343, 362. LC-MS: m/z: 652.90 (Cald.), 652.73 (Found) [M-H].

Complex **1d**: Anal. calcd. for (C₂₃H₃₀N₂O₆SPdCl₂) (%): C, 43.17; H, 4.69; N, 4.37; S, 5.00. Found: C, 43.13; H, 4.70; N, 4.38; S, 5.16. IR (KBr, cm⁻¹): 3445 (-OH), 3060 (Ar-H), 2978 (Al-H), 1683 (C=O), 1583 (CH=N), 1533 (Ar-C), 1247 (-OCH₃), 757 (C-S-C), 573, 510 (M-O), 487 (M-N). ¹H-NMR (300 MHz, DMSO-d₆, ppm): 8.68 (s, 1H, CH=N), 7.95-6.90 (m, 4H, ArH), 5.37, 4.32 (m, 4H, -2CH₂), 3.97-2.42 (m, 4H, CH₂ (pyridine)), 1.28-1.22 (d, 12H, -CH₃). ¹³C-NMR (75 MHz, DMSO-d₆, ppm): 165.00, 161.00 (2C=O), 157.20 (CH=N), 134.00-120.10 (thiophenyl), 128.70-111.00 (benzene ring), 77.24 (tert-butyl), 55.60, 14.47 (-OC₂H₅), 53.44 (pyridine), 28.70 (C(CH₃)₃). UV-Vis. (λ_{max}, nm): π→π*, 205, 215, 251; n→π*, 315, 398. LC-MS: m/z: 550.89 (Cald.), 550.99 (Found) [M-Cl₂, H₂O]²⁺.

Table 2. Optimization of the reaction conditions for Suzuki coupling reaction.

Entry	Solvent	Time (h)	Yield (%)
1	Ethanol	10	72
2	Methanol	10	60
3	Acetonitrile	10	35
4	Toluene	10	52
5	DMF	10	41
6	THF	10	39
7	Dioxane	10	41
8	i-PrOH+H ₂ O	10	76
9	EtOH+H ₂ O	1	95

²Reaction conditions: Phenyl boronic acid (3.0 mmol), aryl bromide (2.0 mmol), base (4.0 mmol), catalyst (0.01 mmol), solvent (5 mL) and 25 °C.

**Figure 2.** Suzuki-Miyaura cross-coupling reaction.

Catalytic Activity of Pd(II) Complexes for Suzuki-Miyaura Cross-Coupling Reaction

Suzuki-Miyaura cross-coupling is a reaction with palladium-catalyzed aryl and vinyl halide-containing aryl or vinyl boronic acid [19]. A reaction mixture of phenylboronic acid (3.0 mmol), aryl bromide (2.0 mmol), base (4.0 mmol) and catalyst (0.01 mmol) was mixed in (EtOH/H₂O) (1:3) (5 mL) at 25 °C for 1 h (Fig. 2). After the reaction completed, the mixture was extracted with ethyl acetate. The ethyl acetate solution was dried over MgSO₄ and filtered to remove the trace water content. The ethyl acetate solution was passed through a silica column (60-120 mesh), and there for impurities were removed. The yields were measured by GC-MS.






The optimization conditions were determined first during the experimental studies. In order to determine the appropriate base to be used in the Suzuki reaction, a reaction of p-bromoacetophenone and phenylboronic acid was performed in EtOH/H₂O (1:3) mixture at 25 °C and atmospheric condition for 1 h. Optimum conditions were formed using **1a** complex as catalyst. Various bases such as KOH, NaOH, KOBu^t, K₂CO₃ and Cs₂CO₃ were checked. The obtained results are given in Table 1 and Table 2.

RESULTS AND DISCUSSION

IR spectra of Pd(II) complexes (**1a-d**) showed that azomethine peaks shifted to a high or low area, unlike ligands. This indicated that the Pd metal was coordinated with the N atom of the azomethine group of ligands. In the complexes **1a** and **1c**, it was connected with carbonyl oxygen and supported by band shifts [15]. In the **1b** complex, the absence of the peak of the OH group seen in the ligand and the shift in the (C-O) peak, unlike the ligand, indicated that there was coordination with the phenolic oxygen atom [16]. The new bands for all Pd(II) complexes (**1a-d**) in range of 573-510 cm⁻¹ and 503-463 cm⁻¹ suggested a coordination of the carbonyl/hydroxyl oxygen and azomethine nitrogen atom to the palladium, respectively [6, 17-19].

The ¹H-NMR spectra of Pd(II) complexes (**1a-d**) showed signals 8.10, 8.80, 8.32, 8.68 ppm for azomethine (-CH=N-) proton, respectively. For **1b** complex, the phenolic OH proton disappeared because of the deprotonation of

Table 3. Suzuki coupling reaction of various aryl bromide with phenylboronic acid.

Entry	Pd (II)	Aryl Bromide	Temp (°C)	Yield (%)
1	1a			95
2	1b		25	96
3	1c			98
4	1d			98
5	1a			66
6	1b		25	97
7	1c			99
8	1d			98
9	1a			93
10	1b		25	95
11	1c			96
12	1d			96
13	1a			96
14	1b		25	75
15	1c			89
16	1d			94
17	1a			100
18	1b		25	100
19	1c			100
20	1d			73

^aReaction conditions: Phenyl boronic acid (3.0 mmol), aryl bromide (2.0 mmol), base (4.0 mmol), catalyst (0.01 mmol), solvent (5 mL) and 25 °C, 1h.

the ligand.

The ¹³C-NMR spectra resonance of azomethine (-CH=N-) carbon atom of Pd(II) complexes (**1a-d**) observed at 163.01, 161.61, 159.30, 157.20 ppm, respectively. This signal indicated coordination of azomethine nitrogen Pd atom [18-20].

The UV-Vis spectrum of the complexes (**1a-d**) exhibited the bands 205-251 nm, which might be attributed to $\pi \rightarrow \pi^*$ transition of the aromatic rings. The bands observed at 301-343 nm region might be attributed to $n \rightarrow \pi^*$ transitions of the C=N moiety. Pd(II) complexes (**1a-d**) showed a low energy band in the range of 504-343 nm for MLCT (metal to ligand charge transfer) transitions. These results may suggest that Pd(II) complexes had a square-planar geometry [6, 22-26].

Table 3 showed that the palladium complexes (**1a-d**) had a good activity in Suzuki-Miyaura C-C coupling reaction. It was seen that there was no precise ranking between the activities of the complexes. The catalytic activities of some complexes were observed to vary between 66-100%,

depending on the aryl bromides used (Table 3, entries 1-20). A yield of up to 100% was obtained with halogenated substrates bearing substituted groups attached to the aromatic ring. The activity of the bromoaryls used as the substrate appeared to vary from *p*-bromoacetophenone > *p*-bromoanisole > *p*-bromobenzene > *p*-bromoaldehyde > *p*-bromotoluene. This means that the catalytic activity of Pd(II) (**1a-d**) complexes were the highest in the case of *p*-bromoacetophenone, providing 95-98% conversion (Table 3, entries 1-4). It was found that both catalysts and aryl bromide were active in terms of structure.

In the present study, it was observed that the efficiency of catalytic transformations for all complexes did not change significantly depending on the substituting groups of Schiff base-Pd(II) complexes. The electronic parameters had no important effect on the catalytic conversion, but the steric effect of the groups present in the Schiff base structure significantly altered the activity of the complexes. In case of *p*-bromoaldehyde used as an aryl bromide, it provided a conversion between 66-98% (Table 3, entries 5-8). In this study, it was found that the efficiency of catalytic transformations for all complexes varied depending on the substitu-

ted groups of Schiff base-Pd(II) complexes. Electronic parameters of Schiff base ligands had a significant effect on the catalytic conversion. The absence of any groups attached to the benzene ring of the ligand resulted in a low yield of 66% in the **1a** complex. Therefore, it was concluded that the catalysts significantly affected the activity of the electronic structures.

When *p*-bromoanisole was used as an aryl bromide, catalytic conversion of the (**1a-d**) complexes ranging from 93-96% was obtained in the rate of catalytic conversion (Table 1, entries 9-12). When the catalytic transformations of the (**1a-d**) complexes were evaluated, it was seen that the activity of the catalysts did not change due to the substituted groups of Schiff base-Pd(II) complexes and gave close results to each other. Although the electronic parameters did not have an important influence on the catalytic conversion, the steric effect changed the activity of the complexes significantly. Therefore, it was found that the groups in the Schiff base structure had a significant influence on the activity of the catalysts.

When *p*-bromotoluene was used as an aryl bromide, catalytic transformations ranging from 75-96% were obtained in the catalysis of **1a-d** complexes (Table 1, entries 13-16). The assessment of the catalytic transformations of Pd(II) complexes (**1a-d**) showed that the activity of the catalysts did not change due to the substituting groups of Schiff base-Pd(II) complexes and gave similar results. The electronic parameters did not have an important impact on the catalytic conversion; however, the steric effect significantly changed the activity of the complexes. Pd(II) complex (**1b**) with *p*-bromotoluene was found to show the lowest rate of catalytic activity (Table 1, entry 14). This was due to the electron attracting -OH group in the structure of the **1b** complex.

When *p*-bromobenzene was used as aryl bromide, a good catalytic conversion of 73-100% was achieved (Table 1, entries 17-20). The catalytic transformations of **1a-d** complexes indicated that the activity of the catalysts did not change due to the substituted groups of Schiff base-Pd(II) complexes (**1a-d**) and gave similar results. Although the electronic parameters had no significant impact on the catalytic conversion, the steric effect significantly influenced the activity of the complexes. **1d** complex with *p*-bromobenzene was found to show a relatively low rate of catalytic activity (Table 1, entry 20). This was due to the electron-providing -OCH₃ group in the structure of the **1d** complex.

The Schiff base-Pd(II) complexes (**1a-d**) used in the Suzuki reaction yielded a good degree of catalytic conversion ranging from 66-100%. At the same time, the structure and position of the ligand-bound substituted groups incre-

ased their catalytic activity. It was found that the electronic structure of the Schiff base groups and the electronic effect of the substrate used did not significantly affect the activity of the catalysts. When the catalytic results of Pd(II) complexes were examined, it was observed that all complexes were active for Suzuki-Miyaura coupling reactions and formed active catalytic systems under optimum conditions. Pd(II) complexes (**1a-d**) were found to have a very good catalytic activity.

CONCLUSION

In this study, four new stable and easily soluble Schiff base-Pd(II) complexes (**1a-d**) containing thiophene and pyridine rings were synthesized. The structures were elucidated using different spectroscopic techniques. Spectroscopic data showed that the Pd(II) complexes had a square plane geometric structure. It was also found that Schiff base-Pd(II) complexes provided an excellent catalytic activity in the Suzuki-Miyaura coupling reaction. Pd(II) complexes (**1a-d**) occurred in the Suzuki coupling reactions in a short time and at low temperatures. Thus, it was concluded that the groups in the Schiff base structure had a significant effect on the activity of the catalysts.

ACKNOWLEDGEMENT

This study has been undertaken as part of a research project in Muş Alparslan University with a project number of "BAP-18-TBMY-4902-01". The authors would like to thank BAYPUAM (Scientific Research-Publication and Projects Research and Application Center) for their financial support.

References

1. Beigi Z, Kianfar AH, Farrokhpour H, Roushani M, Azarian MH, Mahmood WAK. Synthesis, characterization and spectroscopic studies of nickel(II) complexes with some tridentate ONN donor Schiff bases and their electrocatalytic application for oxidation of methanol. *Journal of Molecular Liquids* 249 (2018) 117-125.
2. Turan N, Buldurun K, Gündüz B, Çolak N. Synthesis and structures of Fe(II), Zn(II) and Pd(II) complexes with a Schiff base derived from methyl 2-amino-6-methyl-4,5,6,7-tetrahydrothieno[2,3-c]pyridine-3-carboxylate and comparison of their optical constants for different solvents and molarities. *Journal of Nanoelectronics and Optoelectronics* 12 (2017) 1028-1040.
3. Pratihari JL, Mandal P, Lai CK, Chattopadhyay S. Tetradentateamidoazo Schiff base Cu(II), Ni(II) and Pd(II) complexes: Synthesis, characterization, spectral properties, and applications to catalysis in C-C coupling and oxidation reaction. *Polyhedron* 161 (2019) 317-324.
4. Mucse S, Harms K, Biernasiuk A, Malm A, Popiolek L, Hordyjewska A, Olszewska A, Hołynska M. New Pd(II) Schiff base complexes derived from ortho-vanillin and L-tyrosine or L-glutamic acid: Synthesis, characterization, crystal structures and biological

- properties. *Polyhedron* 151 (2018) 465–477.
- Buldurun K, Turan N, Çolak N, Özdemir İ. Schiff base and its Fe(II), Zn(II), Ru(II), Pd(II) complexes containing ONS donor atoms: Synthesis, characterization and catalytic studies. *Dokuz Eylül Üniversitesi Mühendislik Fakültesi Fen ve Mühendislik Dergisi* 21 (2019) 73–82.
 - Kumar SB, Solanki A, Kundu S. Copper(II) and palladium(II) complexes with tridentate NSO donor Schiff base ligand: Synthesis, characterization and structures. *Journal of Molecular Structure* 1143 (2017) 163–167.
 - Ali OAM. Characterization, thermal and fluorescence study of Mn(II) and Pd(II) Schiff base complexes. *Journal of Thermal Analysis and Calorimetry* 128 (2017) 1579–1590.
 - Debono N, Iglesias M, Sanchez F. New Pyridine ONN-Pincer gold and palladium complexes: Synthesis, characterization and catalysis in hydrogenation, hydrosilylation and C-C cross-coupling reactions. *Advanced Synthesis & Catalysis* 349 (2007) 2470–2476.
 - Patel MN, Dosi PA, Bhatt BS. Square planar palladium(II) complexes of bipyridines: Synthesis, characterization, and biological studies. *Journal of Coordination Chemistry* 65 (2012) 3833–3844.
 - Nandhini R, Venkatachalam G, Kumar MD, Jaccob M. Dinuclear Pd(II) complexes containing bis-O,N-bidentate Schiff base ligands: Synthesis, characterization, DFT study and application as Suzuki-Miyaura coupling catalysts. *Polyhedron* 158 (2019) 183–192.
 - Das P, Linert W. Schiff base-derived homogeneous and heterogeneous palladium catalysts for the Suzuki-Miyaura reaction. *Coordination Chemistry Reviews* 311 (2016) 1–23.
 - Ozdemir İ, Çetinkaya B, Demir S, Gürbüz N. Palladium-catalyzed Suzuki-Miyaura reaction using saturated N-heterocarbene ligands. *Catalysis Letters* 97 (2004) 37–40.
 - Baran NY, Baran T, Menteş A, Karakişla M, Saçak M. Highly effective and recoverable Pd(II) catalyst immobilized on thermally stable Schiff base polymer containing phenol group: Production, characterization and application in Suzuki coupling reactions. *Journal of Organometallic Chemistry* 866 (2018) 87–94.
 - Kalita M, Gogoi P, Barman P, Sarma B, Buragohain AK, Kalita RD. A new series of Ni(II), Cu(II), Co(II) and Pd(II) complexes with an ONS donor Schiff base: Synthesis, crystal structure, catalytic properties and bioactivities. *Polyhedron* 74 (2014) 93–98.
 - Priyarega S, Raja DS, Babu SG, Karvembu R, Hashimoto T, Endo A, Natarajan K. Novel binuclear palladium(II) complexes of 2-oxoquinoline-3-carbaldehyde Schiff bases: Synthesis, structure and catalytic applications. *Polyhedron* 34 (2012) 143–148.
 - Amalina MT, Hadariah B, Karimah K, Nazihah WIW. Pd(II) Complexes with nitrogen-oxygen donor ligands: Synthesis, characterization and catalytic activity for Suzuki-Miyaura cross-coupling reaction. *ASEAN Journal on Science and Technology for Development* 31 (2014) 15–23.
 - Layek S, Anuradha, Angrahari B, Pathak DD. Synthesis and characterization of a new Pd(II)-Schiff base complex [Pd(APD)2]: An efficient and recyclable catalyst for Heck-Mizoroki and Suzuki-Miyaura reactions. *Journal of Organometallic Chemistry* 846 (2017) 105–112.
 - León AD, Pons J, Antón JG, Solans X, Bardia MF, Ros J. Preparation, NMR studies and crystal structure of mononuclear and dinuclear Pd(II) and Pt(II) complexes that contain 1,2-bis[3-(3,5-dimethyl-1-pyrazolyl)-2-thiopropyl]benzene. *Polyhedron* 26 (2007) 2921–2928.
 - Agrahari B, Layek S, Anuradha, Ganguly R, Pathak DD. Synthesis, crystal structures, and application of two new pincer type palladium(II)-Schiff base complexes in C-C cross-coupling reactions. *Inorganica Chimica Acta* 471 (2018) 345–354.
 - Hassana HMA, Saad EM, Soltan MS, Betiha MA, Butler IS, Mostafa IS. A palladium(II) 4-hydroxysalicylidene Schiff-base complex anchored on functionalized MCM-41: An efficient heterogeneous catalyst for the epoxidation of olefins. *Applied Catalysis A: General* 488 (2014) 148–159.
 - Bon VV, Orysyk SI, Pekhnyo VI, Volkov SV. Square-planar 1:2 Ni(II) and Pd(II) complexes with different coordination mode of salicylaldehyde (4)-phenylthiosemicarbazone: Synthesis, structure and spectral properties. *Journal of Molecular Structure* 984 (2010) 15–22.
 - Anan NA, Hassan SM, Saad EM, Butler IS, Mostafa SI. Preparation, characterization and pH-metric measurements of 4-hydroxysalicylidenechitosan Schiff-base complexes of Fe(III), Co(II), Ni(II), Cu(II), Zn(II), Ru(III), Rh(III), Pd(II) and Au(III). *Carbohydrate Research* 346 (2011) 775–793.
 - Turan N, Buldurun K, Çolak N, Özdemir İ. Preparation and spectroscopic studies of Fe(II), Ru(II), Pd(II) and Zn(II) complexes of Schiff base containing terephthalaldehyde and their transfer hydrogenation and Suzuki-Miyaura coupling reaction. *Open Chemistry* 17 (2019) 571–580.
 - Mohamed RG, Elantabli FM, Abdel Aziz AA, Moustafa H, El-Medani SM. Synthesis, characterization, NLO properties, antimicrobial, CT-DNA binding and DFT modeling of Ni(II), Pd(II), Pt(II), Mo(IV) and Ru(II) complexes with NOS Schiff base. *Journal of Molecular Structure* 1176 (2019) 501–514.
 - Zaghal HM, Qaseer HA. Complexes of palladium, platinum and rhodium with 2,2'-biquinoline and 2-(2-pyridyl)quinolone. *Transition Metal Chemistry* 16 (1991) 39–44.
 - Zaghal MH, Bani Saeed MS, Abdel Hamid AAG, Ali BF. Substitution reactions of cis-dichloro(2,2'-biquinoline)palladium(II) with amino acids. *Arabian Journal of Chemistry* 10 (2017) S3920–S3928.

Triplex-forming DNA Probe Approach for Silver Detection and the Effect of C-G-C Triplet Distribution on Triplex Stability

Osman Doluca 

Izmir University of Economics, Biomedical Engineering, Izmir, Turkey

ABSTRACT

In this study novel triplex forming DNA probes have been designed in order to detect Ag⁺ ion in low concentrations. The use of triplex forming oligonucleotides is a convenient in applications of sensing biomolecules due to their sequence specificity and programmability. However, the use of triplexes has its own obstacles. While antiparallel triplex forming sequences tend to prefer G-quadruplex formation over triplexes, parallel triplexes are also challenging because their formation is triggered by lowering the pH, or using of high concentrations of cations for the stabilization of C-G-C triplets, ie. Ag⁺. While due to electrostatic forces C-G-C triplets stabilize in the presence of cations, this limits possible choices for a triplex forming sequence. A better understanding of the impact of the sequence and designing accordingly may improve the stability of a triplex and lower the need for high cation concentration. Here we have present Triplex-forming DNA-based probes with different distributions of C-G-C triplets for detection of Ag⁺ and show the impact of the C-G-C triplet distribution on the stability of parallel triplexes. Our results indicate Ag⁺ detection as low as 20 nM and show dramatic increase in stability when C-G-C triplets are positioned at the flanks of the triplex.

Keywords:

Parallel triplex DNA; Triple helical DNA; Triplex DNA; DNA topology, Ag; Silver.

INTRODUCTION

Besides the knowledge that DNA is the primary hereditary molecule with possessing genetic code hidden in its double stranded helix form (B-form), an increasing number of evidence demonstrate that DNA, due to its non-canonical (non-B-form) structures, have regulatory functions on various cellular processes as well [1]. While duplex form of DNA is built up via Watson-Crick base pairing edges of nucleotide residues, some forms of the DNA are created by binding of auxiliary strands to a duplex DNA via Hoogsten base pairing edges of nucleotides [2,3]. In particular, triplex DNA forms have become one of the primary research areas due to the possibility of targeting regulatory regions of several oncogenes [2-4] and that their providing ease to manipulation due to exhibiting high stability in comparison to duplex forms [5].

These triplex DNA forms could be created via binding of an auxiliary strand which is either rich in purine or pyrimidine, purine rich strand of the duplex DNA [6].

Depending on the orientation of the auxiliary strand versus the purine rich strand of the duplex, these DNA forms could be created in a parallel fashion, possessing C⁺•G-C and T•A-T triplets or antiparallel fashion possessing G•G-C and A•A-T triplets (• indicates Hoogsten base pairing of third strand, – indicates Watson-Crick base pairing between two strands of duplex DNA) [7]. Despite the fact that both parallel and antiparallel triplex DNA forms could be created in physiological environment, C⁺•G-C triplexes require protonation of cytosine residues of third strand at the position of N3. Therefore, particularly low pH values enable formation of C⁺•G-C triplets and associated parallel triplexes [8]. Furthermore, there are many characteristics affecting stability of triplexes, such as complementarity and base distribution. A random distribution of purine residues on the duplex sequence does help binding of the third strand and higher stability could be achieved via stacking of these residues consecutively [5]. In the light of these information triplex DNA forms are frequently investigated and manipulated in biotechnological applica-

Article History:

Received: 2019/10/30

Accepted: 2019/12/04

Online: 2019/12/31

Correspondence to: Osman Doluca, Izmir University of Economics, Biomedical Engineering, Izmir, TURKEY

E-Mail: osman.doluca@ieu.edu.tr Phone: +90 232 488 82 72

tions. For instance the use of triplex DNA as probes is one of promising applications [9]. In this scope, many triplex DNA probes have been designed recently detecting oligonucleotide molecules with sequence specificity such as those including mutations in their sequence [10] and heavy metals that cause health issues around the globe [11].

The main efforts on triplex DNA structures are focused on increasing stability of both parallel and antiparallel triplexes as well as to achieve C⁺•G-C triplexes at neutral pH values. There are many studies applying chemical modifications on nucleotide residues and redesign the backbone of DNA molecules in literature [12]. As such Ihara and his colleagues have demonstrated that Ag⁺ stabilized the C⁺•G-C motif via displacing N3 proton of cytosines. Therefore they have achieved parallel C⁺•G-C triplexes at neutral pH values without protonation of cytosine residues enabling alternative [13].

Silver ion (Ag⁺) has reached wide utilization area from jewelry designing [14] to photography [15] and electronic industry [16] over the years due to its prominent characteristics such as high thermal [17] and electrical conductivity [18], contact resistance [19] etc. Furthermore, due to its high antibacterial [20] and antifungal characteristics [20,21], silver ion is frequently used in medical applications as well, such as production of bone prostheses [22], dental amalgams [23], and catheters [24]. Besides, silver ion could be used as a therapeutic agent in the treatment of many other disorders, for instance mental illness, epilepsy, infectious diseases, nicotine addiction etc [25].

On the other hand, exposure to high amounts of silver through ingestion, inhalation, and skin contact may also cause serious illnesses. Silver is attributed as bioactive compound as it could form protein complexes once it enters the human body through any exposure route. It's discovered that this bioactivity serve a toxic profile of the silver ion which could cause various hazardous disorders in human body. [26] Most studied and prevalent diseases by high exposure of silver ion are called argyria and argyrosis which are characterized as pigment disorders on skin and eyes, respectively. Symptoms of these diseases are observed as turning color of exposure areas into ash gray [27,28]. Additionally, that silver accumulates among many tissues such as kidney, liver, skin, and spleen when high exposure of silver is observed is another fact affecting human health. This accumulation causing impairment over various pathways on related tissue indicates high toxicity of silver ion. [29] For instance it's revealed that high amount of silver causes to structural and functional disorders on red blood cells by depleting of reduced glutathione that is required for biochemical reactions. As such permissible exposure limit (PEL) of both metallic and soluble silver ion was determined as 0.01 mg/m³ by the

Mine Safety and Health Administration (MSHA) and the Occupational Safety and Health Administration (OSHA) in the past decades. [26] Thereby, the detection of silver concentration even in low values among food products, tap water, environment, and any product that could contact with body has been came into prominence when to consider its exposure routes and possible effects on human health.

In this study we report three novel triplex DNA probes (TP1, TP2, and TP3) with parallel C⁺•G-C motifs in order to detect silver ion concentration. Each triplex probes have been functionalized with fluorescein (FAM) and TAMRA molecules at 5' end and in the middle, respectively. The stabilization of the triplex formation via binding of Ag⁺ gives rise to quenching of FAM strength of which depends on the ion concentration. Moreover, the effect of C⁺•G-C sequence alignment on the stability of triplex probes against temperature and urea was investigated. Comparison of the probe sequences also demonstrated that while our triplex DNA probes are efficient tools for detection of silver concentration even in low values, C⁺•G-C distribution has a significant effect on the stability of the triplex DNA forms, with little impact on the ion detection range.

MATERIAL AND METHODS

Triplex DNA Probes Designs and Sample Preparations

The three triplex-forming DNA probes have been designed with distinct C-G-C triplet distribution. TP1, TP2 and TP3, triplex-forming DNA sequences have been purchased with sequences of 5'-/FAM/CTC TCT CTC TCT TTT TCT CTC TCT CTC TTT/TAMRA/ TGA GAG AGA GAG A-3', 5'-/FAM/CTT CCT TCC CTT TTT TTC CCT TCC TTC TTT/TAMRA/ TGA AGG AAG GGA A-3' and 5'-/FAM/CCC TTC CTT CTT TTT TTC TTC CTT CCC TTT/TAMRA/ TGG GAA GGA AGA A-3', respectively. (Pentabase, Denmark) All sequences were dissolved in 10 mM Tris-EDTA (TE) buffer at pH 7.4 with 100 μM final sequence concentration. As a silver ion source, AgNO₃ was dissolved in Tris-Acetate buffer at 10 mM concentration. No HCl was used during pH adjustment to avoid precipitation with silver. All solutions were stored in 4 °C until utilization in further analysis.

Circular Dichroism (CD) Spectrophotometry Analysis

The structural alterations of free triplex DNA probes with silver binding have been investigated with Jasco J-1500 circular dichroism (CD) spectrophotometer device. All CD measurements were performed at 0.1μM

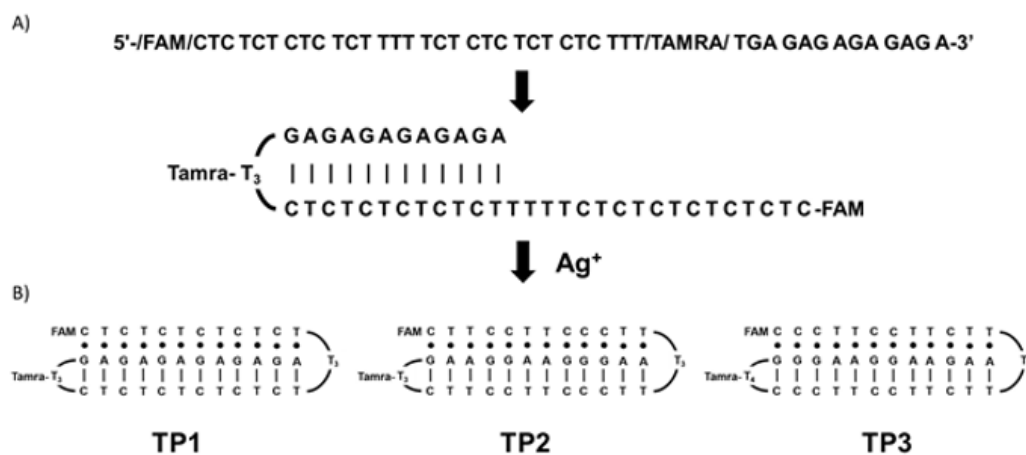


Figure 1. Silver mediated triplex formation (A) and triplex-forming probes used in this study (B).

probe concentration with or without 100 μM Ag^+ in TE buffer. Samples were analyzed between 200-350 nm and 300-700 nm wavelengths.

Fluorescence Spectrophotometry Analysis

FRET characteristic fluorescence change following silver binding of triplex DNA probes have been analysed by Jasco FP-8500 fluorescence spectrophotometer with Ag^+ concentration set between 0.02 and 2.0 μM in TE buffer. Triplex DNA probes were set to 0.1 μM . The emission spectra have been analysed between 500 and 700 nm. All fluorescence measurements were performed using 5 nm slit sizes and 0.5 nm data pitch at 100 nm/min data collection rate.

Urea Denaturation Analysis

Stability differentiation of triplex DNA probes against urea denaturation has been analyzed by Jasco FP-8500 fluorescence spectrometer. Samples containing 0.1 μM DNA probe mixed with 120 μM Ag^+ in TE buffer has been incubated with different concentrations of urea ranging from 0M to 8M. The samples had been excited at 485 nm and the emission of FAM was analyzed between 500-700 nm wavelength. Denaturation curves were constructed from the emission at 522 nm.

Annealing Temperature Analysis

The annealing temperatures and the formation of the triplexes were analysed using fluorescence characteristics by Jasco FP-8500 fluorescence spectrophotometer. Samples containing 0.1 μM DNA probes mixed with 120 μM Ag^+ had been heated to 80 $^\circ\text{C}$ and FAM emission was analyzed by cooling with constant scales until room temperature was reached. Samples were excited at 485 nm and emission values has been detected between 500-700

nm wavelengths. Renaturation curves were constructed from the emission at 522 nm.

RESULTS AND DISCUSSION

Three intramolecular parallel triplex forming sequences were designed so that the second loop from the 5' end is required to fold to form a duplex and the first one to fold to form a triplex. The sequences bear a 5' FAM modification and an internal TAMRA modification attached to a thymine located in the second loop so that in unfolded form the distance should be around 10 nm which is too large for FRET to occur. The sequences are designed so that duplex formation alone should not decrease FAM and TAMRA distance except only upon triplex formation this distance would decrease allowing TAMRA quenching FAM fluorescence. The only differences between the three probe designs is at the sequence level, particularly the distribution of C-G-C triplet, while keeping overall counts of C-G-C triplets equal to 6. In TP1 C-G-C triplets are evenly distributed and separated by T-A-T triplets. In TP2 C-G-C triplets were concentrated to be located further away from the fluorescent moieties and the second loop and closer to the first loop which was responsible for triplex formation. In case of TP3, C-G-C triplets were located away from the first loop and closer to the fluorescent moieties. All loops were composed of four thymines (Fig. 1).

Duplex Triplex Transition

The triplex formation is expected to occur upon the folding of the first loops and controlled by Ag^+ concentration. FAM emission at 520 nm decrease was observed for all probes upon addition of AgNO_3 . For probe concentrations of 0.1 μM , this transition was apparent starting from as low as 20 nM of AgNO_3 until 2 μM . In comparison TAMRA emission become apparent at 580 nm as

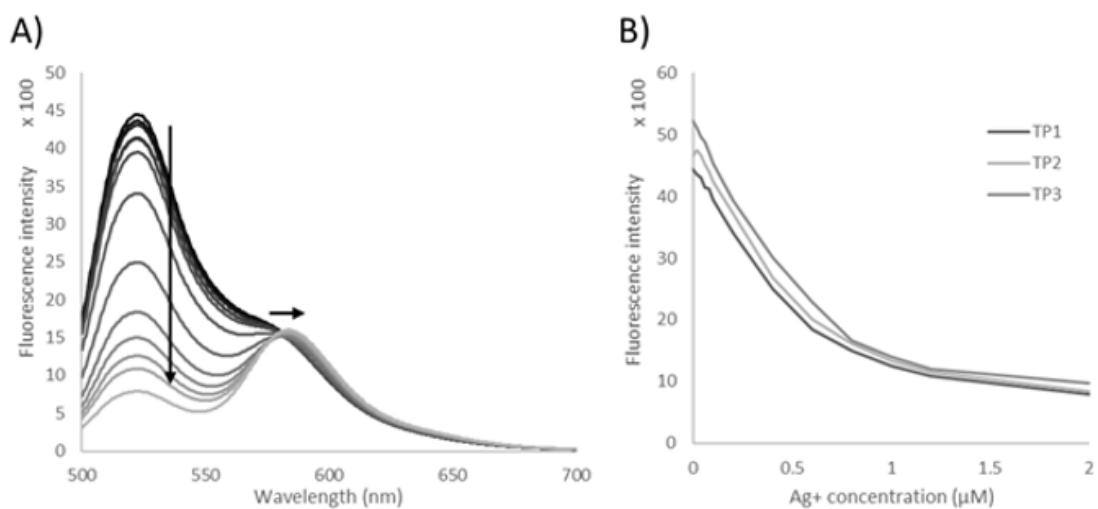


Figure 2. Change in fluorescence spectrum of TP1 (A) and fluorescence intensity of all probes (B) with increasing Ag^+ concentration.

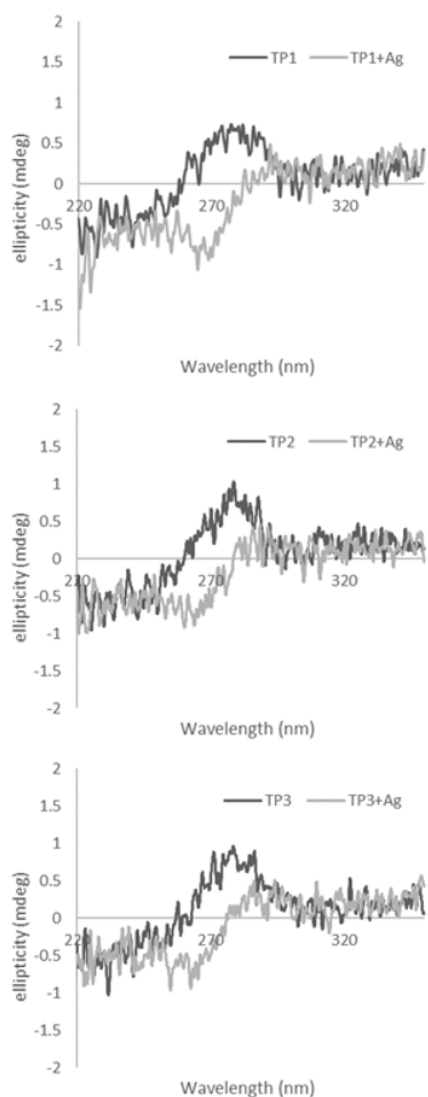


Figure 3. Change in circular dichroism spectra of the probes upon triplex formation.

FAM fluorescence decreased. The transition was sharp and linear between 0.1 and 0.8 μM . We observed little difference in fluorescence with Ag^+ titration of the probes. (Fig. 2) Structural transition was also confirmed by CD analysis where addition of AgNO_3 dramatic change in CD signatures as the maxima at 280 nm of the duplex converts to a minima at 260 nm. At the same time, no significant CD signature was detected above 300 nm. It should be noted that the CD signals were quite low due to low probe concentrations (Fig. 3).

Difference in Melting and Annealing

Although all probes showed highly similar characteristics upon AgNO_3 addition, they differed in terms of their stability. Urea mediated denaturation showed that while TP1 and TP2 showed similar denaturation curves with a maximum change between 0 and 1 M Urea, TP3 showed significantly better stability. TP3 denaturation showed a longer transition period starting from 0 M to 3 M. The improved stability of TP3 was also apparent in case of annealing studies. When probes melt at elevated temperatures were allowed to cool down and form triplex in the presence of Ag^+ , the annealing temperature (T_a) was found as the temperature where emission change was maximum. It was shown that 32°C was the T_a for both TP1 and TP2, while for TP3 T_a was 62°C (Fig. 4).

For all three probes tested here, Ag^+ mediated parallel triplex formation was demonstrated. Ag^+ titration decreased FAM fluorescence while TAMRA showed slight increase in fluorescence, indicating FRET between FAM and TAMRA which is explained by decreased distance between the fluorophores. The decreased distance is expected to occur upon folding of the first loop as a result of parallel triplex formation. Alternatively it may be possible upon association

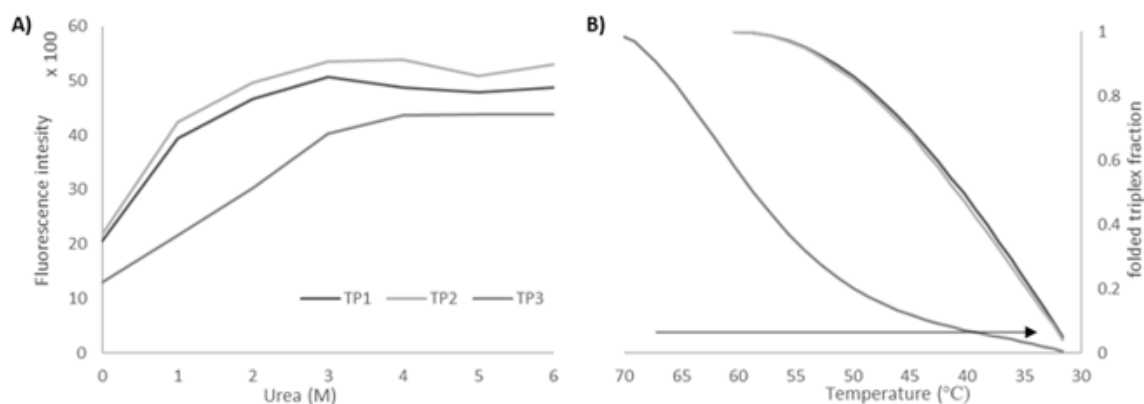


Figure 4. Urea denaturation (A) and annealing (B) analysis of the probes used in the study.

of two probes to form a bimolecular parallel triplex, however, it is less likely, especially in lower concentrations of the probes. The structural difference was also shown via circular dichroism at around 250 and 280 nm where the signal may only depend on the nucleobases, indicating a structural transition at the DNA level.

While the impact of the distribution of the C-G-C triplets was not apparent for their affinity towards Ag^+ , it became clear with the stability tests. The melting of a helical structure, whether it be duplex or triplex, is expected to start from the ends. In the case of the triplex-forming probes used here, the 3' end of the triplex-forming branch is stabilized by the loop, leaving the 5' end as the melting-start site. Comparing the triplex-forming probes, with three C-G-C triplets located at the 5' end in TP3 is expected to benefit its stability over others, through the stabilising effect of the Ag^+ on the C-G-C triplets. Indeed, on both urea denaturation and annealing studies TP3 showed significantly better stability. In comparison, TP1 and 2, which have only one C-G-C triplets at the 5' end, showed marginal difference between each other.

CONCLUSION

Here we have showed triplex forming probes with different C-G-C distributions are equally effective in detection of Ag^+ . While Ag^+ stabilized C-G-C triplets that are located at the ends of the sequence does not affect the affinity towards the Ag^+ , it contributes to the overall stability of the triplexes. In the light of our findings we advise inclusion of three C-G-C triplets at the flanks of parallel triplex-forming sequences whether it be stabilized by Ag^+ or H^+ for improved overall stability. With either cation the C-G-C triplets would contribute to the stability more than T-A-T triplets due to the additional electrostatic forces besides the H-bonds. Furthermore, in the light of knowledge about disorders basing on Ag^+ toxicity, the importance of Ag^+ detection was emphasized previously. Our results demonstrated that the triplex formings DNA

probe could be a novel biotechnological approach to detect Ag^+ even in low concentrations between the range of 0.02-2.0 μM .

ACKNOWLEDGEMENT

This study was supported by Izmir University of Economics (BAP 2017-05).

References

1. Pugeta N, Miller KM, Legube G. Non-canonical DNA/RNA structures during Transcription-Coupled Double-Strand Break Repair: Roadblocks or Bona fide repair intermediates? *DNA Repair* (2019) 102661.
2. Travers A, Muskhelishvili G. DNA structure and function. *FEBS Journal* 282 (2015) 2279–2295.
3. Frank-Kamenetskii MD, Mirkin SM. Triplex DNA structures. *Annual Reviews of Biochemistry* 64 (1995) 65–95.
4. Christensen LA, Finch RA, Booker AJ, Vasquez KM. Targeting oncogenes to improve breast cancer chemotherapy. *Cancer Research* 66 (2006) 4089–4094.
5. Rusling DA. The stability of triplex DNA is affected by the stability of the underlying duplex. *Biophysical Chemistry* 145 (2009) 105–110.
6. Maldonado R, Filarsky M, Grummt I, Längst G. Purine- and pyrimidine-triple-helix-forming oligonucleotides recognize qualitatively different target sites at the ribosomal DNA locus. *RNA* 24 (2018) 371–380.
7. Jain A, Wang G, Vasquez KM. DNA triple helices: biological consequences and therapeutic potential. *Biochimie* 90 (2008) 1117–1130.
8. Bacolla A, Wang G, Vasquez KM. New Perspectives on DNA and RNA Triplexes As Effectors of Biological Activity. *PLoS Genetics* 11 (2015) e1005696.
9. Hu Y, Ceconello A, Idili A, Ricci F, Willner I. Triplex DNA Nanostructures: From Basic Properties to Applications. *Angewandte Chemie International Edition* 56 (2017) 15210–15233.
10. Yang Y, Huang Y, Li C. A reusable electrochemical sensor for one-step biosensing in complex media using triplex-forming oligonucleotide coupled DNA nanostructure. *Analytica Chimica Acta* 1055 (2019) 90–97.
11. Ma DL, Ma VPY, Chan DSH, Leung KH, He HZ, Leung CH. Recent advances in luminescent heavy metal complexes for

- sensing. *Coordination Chemistry Reviews* 256 (2012) 3087–3113. doi:10.1016/j.ccr.2012.07.005.
12. Torigoe H, Nakagawa O, Imanishi T, Obika S, Sasaki K. Chemical modification of triplex-forming oligonucleotide to promote pyrimidine motif triplex formation at physiological pH. *Biochimie* 94 (2012) 1032–1040.
 13. Ihara T, Ishii T, Araki N, Wilson AW, Jyo A. Silver ion unusually stabilizes the structure of a parallel-motif DNA triplex. *Journal of the American Chemical Society* 131 (2009) 3826–3827.
 14. Aktepe N, Kocyyigit A, Yukselten Y, Taskin A, Keskin C, Celik H. Increased DNA damage and oxidative stress among silver jewelry workers. *Biological Trace Element Research* 164 (2015) 185–191.
 15. Villena AN. Exploring confocal microscopy to analyze ancient photography. *Journal of Cultural Heritage* 36 (2019) 191–199.
 16. Zhang H, Suganuma K. Sintered Silver for LED Applications, in: Siow KS (Ed) *Die-Attach Materials for High Temperature Applications in Microelectronics Packaging*. Springer, pp 35–65, 2019. doi:10.1007/978-3-319-99256-3_2.
 17. Abbasi S. The thermal conductivity modeling of nanofluids involving modified Cu nanorods by Ag nanoparticles. *Heat and Mass Transfer* 55 (2019) 891–897. doi:10.1007/s00231-018-2476-2.
 18. Sun G, Wang Z, Huang J. Electromagnetic shielding effectiveness and electrical conductivity of a thin silver layer deposited onto cellulose film via electroless plating. *Journal of Materials Science: Materials in Electronics* 30 (2019) 12044–12053. doi:10.1007/s10854-019-01562-z.
 19. Chung S, Jeong J, Kim D, Park Y, Lee C, Hong Y. Contact Resistance of Inkjet-Printed Silver Source–Drain Electrodes in Bottom-Contact OTFTs. *Journal of Display Technology* 8 (2012) 48–53.
 20. Sarkar R. Aqueous synthesis and antibacterial activity of Silver nanoparticles against *Pseudomonas putida*. *Materials Today: Proceedings* 11 (2019) 686–694.
 21. Bocate KP. Antifungal activity of silver nanoparticles and simvastatin against toxigenic species of *Aspergillus*. *International Journal of Food Microbiology* 291 (2019) 79–86.
 22. Streitberger A, Henrichs MP, Hauschild G, Nottrott M, Guder W, Harges J. Silver-coated megaprotheses in the proximal femur in patients with sarcoma. *European Journal of Orthopaedic Surgery & Traumatology* 29 (2019) 79–85.
 23. Mohammadi Z, Mesgar AS, Rahmdar S, Farhangi E. Effect of setting time and artificial saliva on the strength evaluated by different methods of dental silver amalgam: A comparative study. *Materialwissenschaft Und Werkstofftechnik* 50 (2019) 747–760. doi:10.1002/mawe.201800022.
 24. Akcam FZ, Kaya O, Temel EN, Buyuktuna SA, Unal O, Yurekli VA. An investigation of the effectiveness against bacteriuria of silver-coated catheters in short-term urinary catheter applications: A randomized controlled study. *Journal of Infection and Chemotherapy* 25 (2019) 797–800. doi:10.1016/j.jiac.2019.04.004.
 25. Gulbranson SH, Hud JA, Hansen RC. Argyria following the use of dietary supplements containing colloidal silver protein. *Cutis* 66 (2000) 373–374.
 26. Drake PL, Hazelwood KJ. Exposure-Related Health Effects of Silver and Silver Compounds: A Review. *Annals of Occupational Hygiene* 49 (2005) 575–585.
 27. Molina-Hernandez AI, Diaz-Gonzalez JM, Saeb-Lima M, Dominguez-Cherit J. Argyria after Silver Nitrate Intake: Case Report and Brief Review of Literature. *Indian Journal of Dermatology* 60 (2015) 520.
 28. Pala G, Fronterré A, Scafa F, Scelsi M, Ceccuzzi R, Gentile E, Candura SM. Ocular argyrosis in a silver craftsman. *Journal of Occupational Health* 50 (2008) 521–524.
 29. Lansdown ABG. A pharmacological and toxicological profile of silver as an antimicrobial agent in medical devices. *Advances in Pharmacological Science* 2010 (2010) 910686.

Nucleate Pool Boiling on A Plain Surface

Tugba Tetik^{1,2}  Ismail Yalcin Uralcan¹

¹Istanbul Technical University, Department of Mechanical Engineering, Istanbul, Turkey

²Istanbul Medeniyet University, Department of Mechanical Engineering, Istanbul, Turkey

ABSTRACT

Nucleate pool boiling of distilled water on a plain copper surface has been investigated experimentally and modeled numerically. In the experimental study, bubble behavior on a single nucleation site was observed using high-speed photography and long-distance microscopy. Diameter for a single bubble growth was determined during the ebullition cycle via recordings. Numerical simulations have been carried out using CLSVOF method using ANSYS 18.2. To verify the simulation, the bubble growth period is compared with the results of the experimental study. Data from the numerical results compare reasonably well with the experimental study.

Keywords:

Nucleate Pool Boiling, Bubble Growth Rate, High-Speed Photography; CLSVOF

INTRODUCTION

Multiphase flows are used in a wide range of industrial applications such as heat exchangers, nuclear reactors, food production, chemical processes, and electronic cooling. It is important to understand, model and simulate multiphase phenomena such as boiling, for cooling technology.

In boiling systems, a large amount of heat is transferred from the surface within small temperature differences between the surface and saturation temperature of the fluid. Although there are many experimental, computational and analytical studies on boiling phenomena, its highly complex physical mechanism hasn't been clarified yet. In recent years, bubbling characteristics have been observed visually on several surface materials with various surface properties such as roughness, cavity size, shape, and spacing.

Zhang and Shoji (2003), made experiments on a silicon surface (15 mm diameter, 0.2 mm thickness) with distilled water [1]. They worked on cylindrical artificial cavities (10 μm diameter and 80 μm depth) arranged as single or twin cavities with 1, 2, 3, 4, 6 and 8 mm spacing. The bubbling behavior is recorded with a high-speed camera and temperature fluctuations beneath and around the cavities are measured with radiation thermometers. According to their observation and analysis, three significant factors involving nucleation site interactions are determined: hydrodynamic interaction between bubbles; thermal interaction between nucleation sites;

horizontal and declining bubble coalescences. Qi and Klausner (2005), studied the activation of cavities with cylindrical, triangular, square and rectangular cross-sections, experimentally [2]. They proposed a vapor trapping mechanism for cylindrical cavities. Mchale and Garimella (2010) conducted pool boiling experiments with FC-77 on smooth and rough surfaces [3]. The bubble diameter at departure, bubble departure frequency, active nucleation site density, and bubble terminal velocity are measured via monochromatic video recordings obtained using a CCD camera. Interactions between bubbles are characterized. Moita et al. made heat transfer and bubble dynamics analysis on smooth and microstructured surfaces in cooling applications [4]. Their results showed that the heat transfer coefficient for water in the microstructured surface was 10 times higher than the smooth surface.

Boiling phenomena has also been modeled using different numerical schemes. In these models, the liquid-vapor interface is captured with VOF and CLSVOF methods. CLSVOF method was proposed by Bourlioux (1995) [5] and developed by Sussmann&Puckett (2000) [6]. This method is one of the most widely used interface capturing methods and has been used by many researchers in different fields [7-9]. In CLSVOF method, transport equations are solved both for VOF and level-set fields. VOF provides mass conservation in every mesh, while Level-set defines the interface contour and differentiable fields. Lamas et al. (2012), investigated fluid

Article History:

Received: 2019/11/07

Accepted: 2019/11/20

Online: 2019/12/31

Correspondence to: Tugba Tetik Istanbul Technical University, Department of Mechanical Engineering, Istanbul, Turkey
Tel: +90 212 293 13 00
Fax: +90 212 245 07 95
E-Mail: tetikt@itu.edu.tr

flow around bubbles by analyzing nucleation, growing and detachment processes [10]. In the study, open source software OpenFOAM was used. Depending on the numerical results, a correlation for bubble departure diameter was proposed. Zahedi et al.(2014), simulated bubble formation from an orifice with Fluent 6.3 [11]. In the study, VOF model is used and numerical results were compared with experimental observations and literature results. According to the results, bubble size and detachment time are linear functions of surface tension and decreases with increasing liquid density. Stojanović et al. (2016), studied pool boiling of saturated water under atmospheric conditions, numerically [12]. In the study, density of nucleation sites and bubble residence time on the wall was studied. The influence of these parameters was discussed on pool boiling dynamics.

Although there are many parameters affecting heat transfer in boiling, in the present paper, only bubble growth and departure diameter were studied. Bubble departure diameter and frequency were obtained both experimentally and numerically in the growth period and at departure. The numerical study considers vapor nuclei on a heated wall in a pool of liquid.

METHOD OF ANALYSIS

Bubble dynamics were observed experimentally and modeled numerically.

Experimental Study

Experimental setup used for pool boiling tests is shown in Fig. 1. It mainly composed of a test pool which incorporates the boiling surface, the power supply system and measurement instrumentation.

The heater is a cylindrical copper rod (6 mm in diameter) which was molded into annular bakelite under high pressure and temperature. The top surface of the copper rod is used as the boiling surface. The smooth surface was produced by mechanical polishing, using sandpapers and alumina particles. The bottom end of the copper rod is screwed into the copper heating block which encompasses the electric heater powered with a 15 V x 200 A DC supply. Three K-type thermocouples (0.5 x 0.8 mm duplex PFA insulated) were positioned on the axis of the copper rod, below the heating surface, and connected to a KEITHLEY 2750 DMM data acquisition system. Axial temperature distribution along the rod, determined via thermocouple readings, is extrapolated in order to specify the boiling surface temperature. The product of the gradient of the temperature profile and the thermal conductivity of Cu gave the heat flux at the boiling surface.

Auxiliary heaters, powered with a 35 V x 20 A DC supply, are placed around the pool in order to maintain satu-

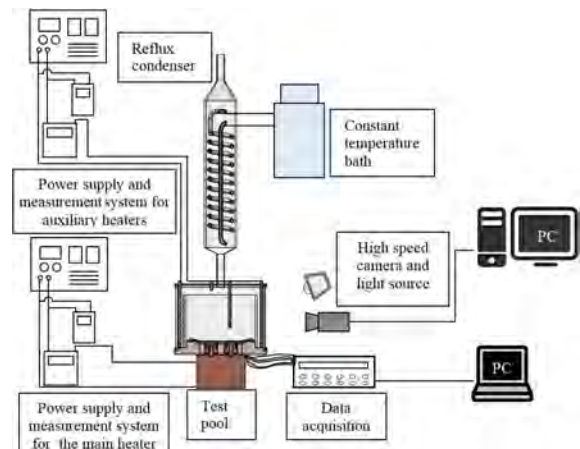


Figure 1. Experimental set-up

ration conditions within the pool. A reflux condenser, equipped with a thermostatic water circulation bath, condenses the vapor formed on the boiling surface and the condensate is returned to the pool.

Prior to each test, the working fluid was boiled by auxiliary heaters to degas it, for at least 2 hours. Afterwards, the DC current to the main heater was adjusted to yield a certain heat flux at the boiling surface. Temperature readings and video recordings were observed until the system attained the steady state and then saved for at least 30 minutes at steady state. All experiments were performed under atmospheric pressure.

The sides of the boiling pool are made of borosilicate glass to visualize the test surface. A high-speed camera (Photron 512-PCI), equipped with a long-distance microscope (Keyence K2 DistaMax) was used to record the images of the growing bubble and the boiling phenomena. Videos are recorded in 4000 fps at 512x256 resolution.

To determine the bubble growth period, at least thirty bubble cycles were examined and average values were plotted. In order to measure bubble diameter, an image processing code was developed in MATLAB. The bubble images were imported into MATLAB and read as a two-dimensional array of color values. After removing noise, Canny method was applied with specified threshold values to detect edges of the bubbles (Fig. 2). The results were given in pixels and then converted to millimeters.



Figure 2. a) Binary image of a bubble b) bubble edge obtained with MATLAB code.

The boiling curve was plotted with experimental heat flux data and compared to Rohsenow's model. Rohsenow's correlation [13], i.e.

$$q'' = \mu_l h_{lv} \left[\frac{(\rho_l - \rho_v) g}{\sigma} \right]^{1/2} \left[\frac{c_{pl} (T_w - T_{sat})}{C_{s,l} h_{lv} Pr_l^n} \right]^3$$

closely approximates nucleate boiling heat flux for clean surfaces. $C_{s,l}$ and n are empirical constants which depend on the surface/liquid combination. Recommended values for the Cu-water pair are $C_{s,l} = 0.013$ and $n = 1$. [13]

Numerical Simulation Model

Numerical simulations were carried out for visualizing the behavior of a single bubble during saturated nucleate boiling of water. Pool boiling is modeled by ANSYS Fluent using CLSVOF (Coupled Level-Set and Volume of Fluid) model and numerical results were obtained by using computational fluid dynamics techniques.

Model geometry has been created in Fluent section of ANSYS workbench. Generated geometry was meshed with hexagonal elements. The computational domain is a 2D axisymmetric rectangular domain having 5 mm radius and 6 mm height. The domain consists of solid and fluid regions in accordance with the experimental set-up. The solid region is copper and, water vapor and liquid water form the liquid region. Liquid water was selected as the primary phase and water vapor as the secondary phase.

Transient conservation mass and momentum equations were solved by the pressure implicit splitting operator (PISO) algorithm. Gravitational effects and surface tension were considered.

In the beginning, the pool was filled with saturated stagnant water. The pressure outlet boundary condition was applied to the boundary of fluid at the top of the calculation domain, the backflow temperature was set to the saturation temperature of the water. Both the left and right sides of the pool were given the insulated boundary condition. Initially, a constant temperature boundary condition was applied to the heater. This period is the waiting period and thermal boundary layer forms. When microlayer formed, spherical water vapor was patched in the cavity as the initial bubble. Calculations continued with constant heat flux applied to the heater.

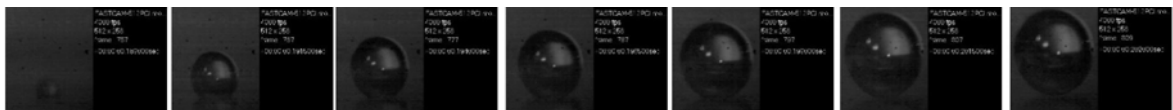


Figure 4 Bubble ebullition cycle for a heat flux 25 kW/m²

CLSVOF method was used to solve conservation equations for the domain and capture the interface of two-phase fluid.

Bubble growth period predicted from the numerical simulations were compared to experimental results.

RESULTS AND DISCUSSION

In the experimental work, temperature distribution along the y-axis of the copper rod was measured with located thermocouples. Surface temperature is estimated by extrapolating thermocouple readings. With using the temperature gradient through the copper rod, heat flux was calculated as

$$q'' = -k_c \frac{dT}{dx}$$

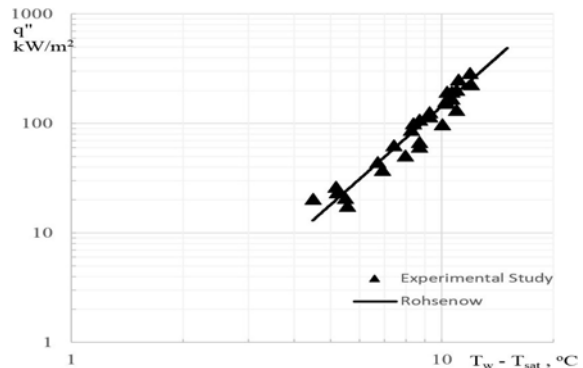


Figure 3 Experimental heat flux data in comparison with Rohsenow equation.

where k_c is the thermal conductivity of copper.

Fig. 3 depicts the heat flux data versus wall superheat for distilled water on a plain copper surface. In the figure, surface heat flux has been predicted both using Rohsenow's well-known model and Fourier's law.

The boiling curve of Rohsenow's model and experimental heat flux data obtained via thermocouple readings show good agreement as plotted in Fig. 3.

The bubble growth under pool boiling conditions was investigated under constant heat flux condition and bubble diameter was measured via fast camera recordings. Photographic images of phases of bubble formation at a nucleation site for a heat flux of 25 kW/m² are shown in Fig. 4.

At low heat fluxes, observed bubbles present a spherical

shape. Since the theoretical boiling models assume bubbles to be spherical we can compare our experimental results with numerical results. However, at high heat fluxes, bubble shapes differ from the sphere due to fluctuations in the fluid and increasing bubble interactions.

The average bubble departure diameters for various Ja numbers are given in comparison with empirical and semi-empirical mathematical models from the literature in Fig. 5. [14–18] Proposed correlations are listed in Table 1. All suggested models have a limited range of application but show a

Table 1. Correlations for bubble departure diameter.

Authors	Correlations
Fritz [14]	$D_b = 0.02080 \sqrt{\frac{\sigma}{g(\rho_s - \rho_b)}}$
Cole [15]	$D_b = 0.04Ja \sqrt{\frac{2\sigma}{g(\rho_s - \rho_b)}}$
Cole & Rohsenow [16]	$D_b = CJa^{5/4} \sqrt{\frac{2\sigma g_c}{g(\rho_s - \rho_b)}}$
Wenzel [17]	$D_b = 0.25 \left[1 + \left(\frac{Ja}{Pr} \right)^2 \frac{100000}{Ar} \right]^{0.5} \sqrt{\frac{2\sigma}{g(\rho_s - \rho_b)}}$
Lee et al. [18]	$D_d = 2 \left[\frac{25}{2} \sqrt{27} Ja \alpha \left(\frac{\rho_s}{\sigma} \right)^{0.5} \right]^2$

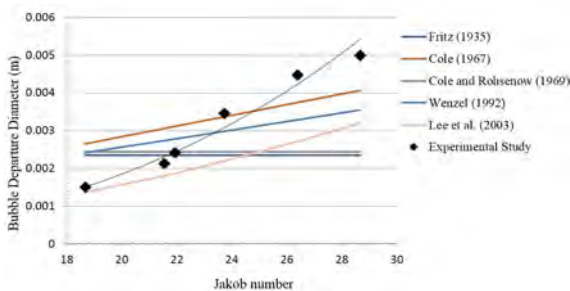


Figure 5. Measured bubble departure diameter at various Ja

Table 2. Correlations for bubble departure diameter and frequency relationship.

Authors	Correlations
Jakob&Fritz [19]	$f D_b = 0.078$
Zuber [20]	$f D_b = 0.59 \left[\frac{\sigma g (\rho_l - \rho_v)}{\rho_l^2} \right]^{0.25}$
Cole [21]	$f D_b^{1/2} = \left[\frac{4g(\rho_l - \rho_v)}{3C_D \rho_l} \right]^{0.5}$

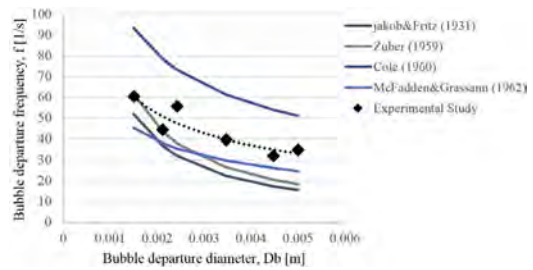


Figure 6. Bubble departure frequency vs departure diameter

similar trend for bubble diameter with increasing Ja.

In the experimental study, each point represents the average value of 30 bubbles. Measured data exhibits a non-linear relationship and increases with Ja. At higher Ja numbers bubbles merge and vapor departs in a larger size from the surface. Also increasing fluid motion near the surface affects the diameter. A power or exponential model can be suggested when more data are deduced from video recor-

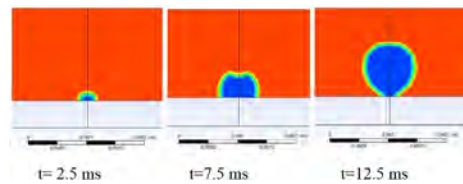


Figure 7. Bubble profile at various time steps

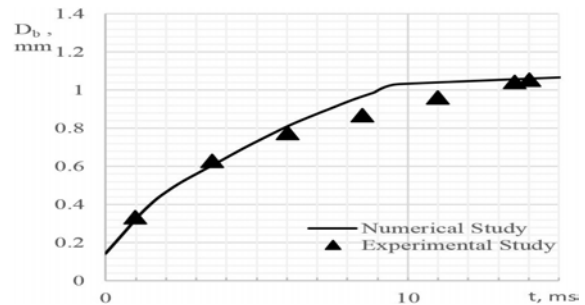


Figure 8. Bubble radius with respect to time. Comparison of experimental and numerical study.

dings in a wider range of Ja number.

Bubble departure frequency versus corresponding bubble departure diameters is given in Fig. 6. Correlations for the determination of departure diameter in pool boiling proposed by researchers are shown in Table 2.

Measured data are compared with theoretical models in the literature. The models predict the experimental trend within an error of $\pm 35\%$.

Fig. 7 represents the computed bubble growth period on a copper surface, using CLSVOF method. In the analysis, 2D axisymmetrical simulations were conducted for water at equilibrium with its vapor phase. The computational domain is symmetrical along the y-axis.

In order to validate the numerical model, experimental data were used. Time dependence of bubble diameters mea-

sured from the experimental data are plotted in comparison with obtained data from numerical analyses results. Numerical analyses match well with the experimental results (Fig. 8).

Both from the experimental and numerical results, one can see that at the initial stage bubble grows rapidly due to liquid inertia and the effects of surface tension. In the second stage, the growth is controlled by the heat transfer from liquid to the vapor-liquid interface. Thus, when the evaporation governs the bubble growth, growth rate decreases. The developed numerical model predicts the bubble growth reasonably well with the experimental measurements

CONCLUSION

In nucleate pool boiling, heat is transferred with bubbles formed on the superheated surface and detached to the bulk liquid. To understand the vapor removal process and determine the heat transfer rate, diameter and the frequency of the vapor bubbles are important parameters.

Nucleate pool boiling experiments at 25 kW/m² were conducted. Heat flux and surface temperature measurements have been made for nucleate pool boiling of water on a polished copper surface. Experimental data is found to be in good agreement with Rohsenow's well-known correlation.

Boiling phenomena was visualized with a high-speed camera system and variation of bubble diameter, from initiation to departure, was measured from the acquired images with developed MATLAB code. Video recordings give detailed information on bubble detachment parameters, i.e. the bubble departure diameter and frequency. At higher heat flux, bubble departure diameter is increasing due to bubble coalescence.

Numerical simulation of bubble dynamics was performed for a single nucleation site. The CLSVOF method is applied to simulate bubble behavior in pool boiling conditions. From the numerical simulation, bubble growth rate and departure diameter were observed. In order to validate simulation, computational results were compared with the experimental data.

The bubble growth rate predicted from the numerical simulations agrees well with the experimental observations captured with high-speed photography technique.

ACKNOWLEDGEMENT

This work is partially supported by "The Office of Scientific Research Projects" at Istanbul Technical University. Project number: 38663

REFERENCES

- Zhang L, Shoji M. Nucleation site interaction in pool boiling on the artificial surface. *International Journal of Heat and Mass Transfer* 46 (2003) 513-522.
- Qi Y, Klausner JF. Heterogeneous nucleation with artificial cavities. *Journal of Heat Transfer* 127 (2005) 1189-1196.
- Mchale JP, Garimella SV. Bubble nucleation characteristics in pool boiling of a wetting liquid on smooth and rough surfaces. *International Journal of Multiphase Flow* 36 (2010) 249-260.
- Moita AS, Teodori E, Moreira ALN. Influence of surface topography in the boiling mechanisms. *International Journal of Heat and Fluid Flow* 52 (2015) 50-63.
- Bourlioux A. A coupled level-set volume-of-fluid algorithm for tracking material interfaces. Paper presented at 6th International Symposium on Computational Fluid Dynamics. Lake Tahoe, NV, pp. 15-22, 1995.
- Sussman M, Puckett EG. A Coupled Level Set and Volume-of-Fluid Method for Computing 3D and Axisymmetric Incompressible Two-Phase Flows. *Journal of Computational Physics* 162 (2000) 301-337.
- Wang Z, Yang J, Koo B, Stern F. A coupled level set and volume-of-fluid method for sharp interface simulation of plunging breaking waves. *International Journal of Multiphase Flow* 35 (2009) 227-246.
- Son G, Hur N. A coupled level set and volume-of-fluid method for the buoyancy-driven motion of fluid particles. *Numerical Heat Transfer, Part B: Fundamentals* 42 (2002) 523-542.
- Arienti M, Sussman M. An embedded level set method for sharp-interface multiphase simulations of Diesel injectors. *International Journal of Multiphase Flow* 59 (2014) 1-14.
- Lamas MI, Sáiz Jabardo JM, Arce A, Fariñas P. Numerical analysis of the bubble detachment diameter in nucleate boiling. *Journal of Physics: Conference Series*, 395 (2012).
- Zahedi P, Saleh R, Moreno-Atanasio R, Yousefi K. Influence of fluid properties on bubble formation, detachment, rising and collapse; Investigation using volume of fluid method. *Korean Journal of Chemical Engineering* 31 (2014) 1349-1361.
- Stojanović A, Stevanović V, Petrović M, Živković D, Stanković B. Numerical study of heat transfer during nucleate pool boiling. *Advanced Technologies* 5 (2016) 73-80.
- Rohsenow WM. A Method of correlating heat transfer data for surface boiling of liquids. Technical Report (1951).
- Fritz W. Berechnung des maximalvolumen von dampfblasen. *Physikalische Zeitschrift*. 36 (1935) 379-388.
- Cole R. Bubble frequencies and departure volumes at subatmospheric pressures. *AIChE Journal* 13 (1967) 779-783.
- Cole R, Rohsenow WM. Correlation of bubble departure diameters for boiling of saturated liquids. *Chemical Engineering Progress Symposium Series* 65 (1969) 211-213.
- Wenzel U. Saturated pool boiling and subcooled flow boiling of mixtures at atmospheric pressure. PhD Thesis, The University of Auckland (1992).
- Lee HC, Oh BD, Bae SW, Kim H. Single bubble growth in saturated pool boiling on a constant wall temperature surface. *International Journal of Multiphase Flow* 29 (2003) 1857-1874.
- Jakob M, Fritz W. Versuche über den verdampfungsvorgang. *Forsch Ingenieurwes.* 2(1931) 435-447.
- Zuber N. Hydrodynamic aspects of boiling heat transfer. PhD Thesis, University of California (1959).
- Cole R. A photographic study of pool boiling in the region of the critical heat flux. *AIChE Journal* 6 (1960) 533-538.

A modified Soft-thresholding Approach in the Transcriptomic Analysis of Adaptation of E.coli to Alternating Substrate Conditions

Muhammed Erkan Karabekmez 

Istanbul Medeniyet University, Department of Bioengineering, Istanbul, Turkey

ABSTRACT

The expression of genes that are functionally related is considered to change together in response to deterioration of internal or external order. The system-level analysis of these changes has become widespread in recent years. Weighted gene co-expression network analysis (WGCNA) is an important tool in the literature. This method has two options in the form of hard and soft thresholding. The power function is used commonly in soft thresholding option. The other alternative of soft thresholding, symmetric sigmoid function, may give less importance to the meaningful co-expression data and not preferred frequently. Both functions has some drawbacks. In this study, it was tried to increase the efficiency of WGCNA approach by using asymmetric sigmoid function. RNA-seq dataset on adaptation of E.coli to alternating substrate conditions was re-investigated with this modified approach and its use was proven by GO and pathway enrichment analysis.

Keywords:

WGCNA, Transcriptomics, Asymmetric Sigmoid Function

INTRODUCTION

Computational techniques have been developed to reveal the biological significance of the large transcriptomic datasets with the emergence of microarray technique in 2000s, which allows high-throughput measurement of gene expression data at the genome level. These techniques are largely based on clustering algorithms, mathematical modeling and network analysis. In addition to the applications of a wider range of mathematical approaches, there are also mathematical approaches developed specifically for this biological context. The most common of these approaches is Zhang and Horvath's weighted gene co-expression analysis (WGCNA) approach, published in 2005 [1]. This method was later improved by many studies [2-9], expanded for meta-analysis [10] and R ready-to-run software was also provided [11]. The WGCNA approach has been used in many studies and has received thousands of citations [12-16].

First, WGCNA numerically calculates the correlations of gene expression across different conditions or temporal points between each gene pair. It then thresholds these pairwise correlation coefficients to transform them into discrete values - which is defined as solid thresholding - or uses the force function or the sig-

moid function to inflate high attenuation and weaken weak attenuation, which is called soft thresholding [1].

In the WGCNA approach, α (when sigmoid function is used), β (when force function is used), and τ (when hard-thresholding used) variables are determined in a way that ensure the network will be independent of the scale, because biological networks are known to be scale-free [17].

By using sigmoid function for transformation, gene pairs whose correlation coefficient is slightly higher than the saddle point, which supposed to be 0.5 are overrated that is why power function is much more common in the literature. On the other hand, by using power function, correlation coefficients that are slightly lower than 1.0 are underrated. Intuitively, it can be hypothesized that shifting saddle point of sigmoid function upwards, i.e. asymmetric sigmoid function, can be used for transformation to avoid both of the drawbacks. However, asymmetric sigmoidal functions have more than one coefficients which complicates the parameterization step. Here in this study we attempted to develop a pipeline to use asymmetric sigmoidal function for soft-thresholding in WGCNA. We used an RNAseq

Article History:

Received: 2019/11/07

Accepted: 2019/11/20

Online: 2019/12/31

Correspondence to: Muhammed Erkan Karabekmez

Istanbul Medeniyet University,

Department of Bioengineering

Tel: 0(216) 280 3333

E-Mail:

erkan.karabekmez@medeniyet.edu.tr

dataset on adaptation of E.coli to alternating substrate conditions to validate this novel approach.

MATERIALS AND METHODS

RNA-seq dataset of E.coli was retrieved from GEO with the accession code of GSE97944 [18]. Quantifications of the dataset was in terms of fragments per kilobase per million (FPKM) and obtained by cufflinks [19] following alignment by using Bowtie 2 algorithm [20].

Cytoscape version 3.6.1 was used to visualize networks [21].

MATLAB R2018b platform was used for thresholding calculations.

When clustering with the WGCNA approach, the existing package on the R platform was used [11].

By using gene ontology and pathway enrichment analyzes, the biological significance of the resulting modules was examined. DAVID 6.8 web-based software tool was used for this purpose [22].

RESULTS

RNA-seq dataset of E.coli is composed of expression levels of 3754 genes at 8 conditions. One of the advantages of WGCNA approach is making use of the whole dataset instead of reducing to a subset of differentially expressed genes. First of all for each gene pair a distance metric (Pearson Correlation Coefficient) is calculated to quantify the similarities between expression profiles across 8 conditions. Secondly, a thresholding approach is followed to reduce the noise. Three basic thresholding approaches- hard thresholding, soft thresholding with power function and soft thresholding with sigmoid function- were used to assess the scale-free networks. Transformation functions with different parameters of sigmoid function (Fig. 1A) and power function (Fig. 1B) were plotted. Sigmoid function provides little transformation while power function leads a huge difference between high similarities.

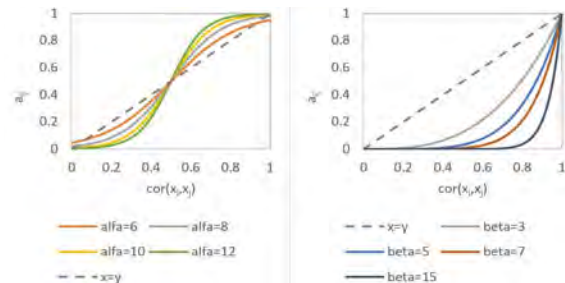


Figure 1. Sigmoid functions with various α values (A) and power function with various β values (B)



Figure 2. A typical scale-free network with a degree-distribution that fit to a linear decrease of frequency with increasing degree on log-scale ($R^2 = 0.918$).

In scale-free networks degree distribution follows power law distribution that is why it should be linear in logarithmic scale. If a line fit to a distribution by linear regression with a slope less than -0.5 and an R^2 value higher than 0.7 the degree distribution was accepted as scale-free. Hereby one can conclude that the constructed network is biologically relevant. A typical scale-free network were plotted by using Cytoscape in order to display the structure (Fig. 2).

It was found that minimum τ value for hard-thresholding was 0.76 to attain scale-free criteria and minimum β value for soft-thresholding with power function was 7. Scale-free criteria could not be attained with sigmoidal function with any parameter.

As a forth thresholding strategy, here in this study, asymmetric sigmoidal function with two parameters (Eq. 1) was used as a novel transformation function.

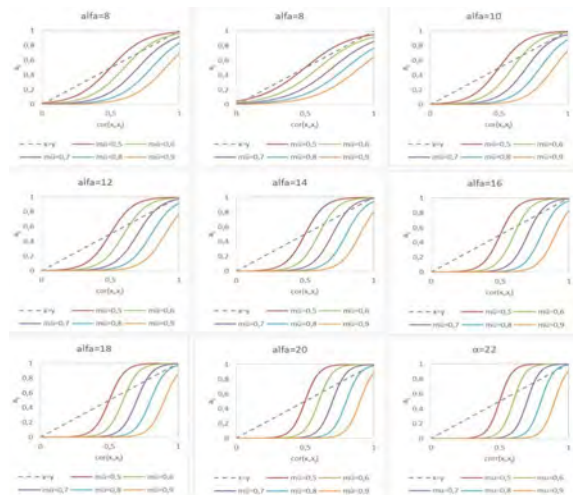


Figure 3. Effect of parameterization on transformation by asymmetric sigmoid function

$$a_{ij} = \frac{1}{1 + e^{-a(|cor(x_i, x_j) - \mu|)}} \tag{1}$$

The effect of different values of α and μ were simulated to display the transformation that they can cause (Fig. 3).

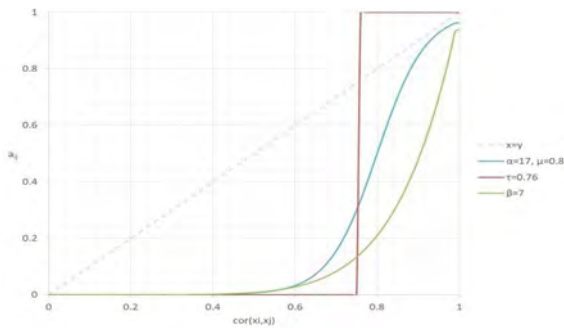


Figure 4. Transformations by hard-thresholding (step-function) (red curve) and soft thresholding by using conventional power function (green curve) and novel asymmetric sigmoidal function (blue curve)

Two hundred different combinations of α and μ were searched by grid search approach and scale-free nature of resulting network for each combination was investigated. The lowest possible μ value was picked first and lowest possible α in combination with the fixed μ was chosen. As a result 0.8 for μ and 17 for α parameters were identified to be attaining scale-free criteria (Fig. 4).

Resulting modules calculated by using the parameterized asymmetric sigmoidal function through the R-package. Biological significance of the modules identified by using power function and asymmetric sigmoidal function were compared with respect to gene ontology and pathway enrichments.

It was observed that larger modules with finer association to specific biological roles were attained by using asymmetric sigmoidal function. For instance; KEGG pathway ribosome was found to be associated with a module with a size of 40 genes with a p-value of $2.42E-04$ with power function whereas there is a larger module of 56 genes with a more significant association to the same pathway with a p-value of $1.65E-13$.

Resulting enrichment analysis were also showed that genes involved in following biological processes and pathways mediates adaptive response of *E.coli* to alternating substrate conditions; oxidative phosphorylation, biosynthesis of amino acids, flagellar assembly and response to stress.

DISCUSSION

WGCNA is one of the most common approaches for transcriptomic data analysis. It is shown in this study that asymmetric sigmoidal function with two parameters can improve performance of WGCNA and its usefulness was shown in adaptive response of *E.coli* to alternating substrate conditions. The parameterization process should be validated across different datasets and a systematic procedure should be developed to standardize the future efforts. And as another further work this approach should be included into automated R-packages of WGCNA for its wider use.

ACKNOWLEDGEMENT

This work was supported by Istanbul Medeniyet University through BAP Grant No. F-GAP-2018-1245.

REFERENCES

- Zhang B and Horvath S. A General Framework for Weighted Gene Co-Expression Network Analysis. *Statistical Applications in Genetics and Molecular Biology*: Vol. 4: No. 1, (2005) Article 17 PMID: 16646834.
- Dong J, Horvath S. Understanding Network Concepts in Modules. *BMC Systems Biology*, 1:24 (2007) PMID: 17547772 PMID: PMC3238286.
- Horvath S, Dong J. Geometric Interpretation of Gene Coexpression Network Analysis. *PLoS Comput Biol* 4(8): (2008) e1000117 PMID: 18704157 PMID: PMC2446438.
- Yip A, Horvath S. Gene network interconnectedness and the generalized topological overlap measure. *BMC Bioinformatics*, 8:22. (2007) PMID: 17250769 PMID: PMC1797055.
- Li A, Horvath S. Network Neighborhood Analysis with the multi-node topological overlap measure. *Bioinformatics*. (2006) PMID: 17110366 doi:10.1093/bioinformatics/btl581.
- Langfelder P, Zhang B, Horvath S. Defining clusters from a hierarchical cluster tree: the Dynamic Tree Cut library for R. *Bioinformatics*. November/btm563 (2007) PMID: 18024473.
- Aten JE, Fuller TF, Lusis AJ, Horvath S. Using genetic markers to orient the edges in quantitative trait networks: the NEO software. *BMC Systems Biology* 2008, 2:34 (2008) PMID: 18412962 PMID: PMC2387136.
- Langfelder P, Luo R, Oldham MC, Horvath S. Is my network module preserved and reproducible? *PLoS Comp Biol*. 7(1): (2011) e1001057 PMID: 21283776 PMID: PMC3024255.
- Song L, Langfelder P, Horvath S. Random generalized linear model: a highly accurate and interpretable ensemble predictor. *BMC Bioinformatics* 14:5 (2013) PMID: 23323760 DOI: 10.1186/1471-2105-14-5.
- Langfelder P, Horvath S. Eigengene networks for studying the relationships between co-expression modules. *BMC Systems Biology* 2007, 1:54 (2007) PMID: 18031580.
- Langfelder P, Horvath S. WGCNA: an R package for weighted correlation network analysis. *BMC Bioinformatics* 2008, 9:559. (2008) PMID: 19114008 PMID: PMC2631488.
- Xue Z, Huang K, Cai C, Cai L, Jiang CY, Feng Y, Liu Z, Zeng Q, Cheng L, Sun YE, Liu JY, Horvath S, Fan G. Genetic programs in human and mouse early embryos revealed by single-cell RNA sequencing. *Nature*. 2013 Jul 28. (2013) doi: 10.1038/nature12364 PMID: 23892778.
- van Eijk KR, de Jong S, Boks MP, Langeveld T, Colas F, Veldink JH, de Kovel CG, Janson E, Strengman E, Langfelder P, Kahn RS, van den Berg LH, Horvath S, Ophoff RA. Genetic analysis of DNA methylation and gene expression levels in whole blood of healthy human subjects *BMC Genomics*. 2012 Nov 17;13(1):636 (2012) PMID: 23157493.
- Wang, W., Jiang, W., Hou, L., Duan, H., Wu, Y., Xu, C., ... & Zhang, D. Weighted gene co-expression network analysis of expression data of monozygotic twins identifies specific modules and hub genes related to BMI. *BMC genomics*, 18(1), 872. (2017).
- Miller, J. A., Guillozet-Bongaarts, A., Gibbons, L. E., Postupna, N., Renz, A., Beller, A. E., ... & Szafer, A. Neuropathological and transcriptomic characteristics of the aged brain. *eLife*, 6. (2017).
- Simon, S., Sagasser, S., Saccenti, E., Brugler, M. R., Schranz, M.

- E., Hadrys, H., ... & DeSalle, R. Comparative transcriptomics reveal developmental turning points during embryogenesis of a hemimetabolous insect, the damselfly *Ischnura elegans*. *Scientific Reports*, 7(1), (2017) 13547.
17. Albert, R., & Barabási, A. L. Statistical mechanics of complex networks. *Reviews of modern physics*, 74(1), (2002), 47.
 18. Sandberg, T. E., Lloyd, C. J., Palsson, B. O., & Feist, A. M. Laboratory evolution to alternating substrate environments yields distinct phenotypic and genetic adaptive strategies. *Appl. Environ. Microbiol.*, 83(13), (2017), e00410-17.
 19. Trapnell, C., Williams, B. A., Pertea, G., Mortazavi, A., Kwan, G., Van Baren, M. J., ... & Pachter, L.. Transcript assembly and quantification by RNA-Seq reveals unannotated transcripts and isoform switching during cell differentiation. *Nature biotechnology*, 28(5), 511, (2010).
 20. Langmead, B., & Salzberg, S. L. Fast gapped-read alignment with Bowtie 2. *Nature methods*, 9(4), 357, (2012).
 21. Shannon, P., Markiel, A., Ozier, O., Baliga, N. S., Wang, J. T., Ramage, D., ... & Ideker, T. Cytoscape: a software environment for integrated models of biomolecular interaction networks. *Genome research*, 13(11), 2498-2504, (2003).
 22. Huang, D. W., Sherman, B. T., & Lempicki, R. A. Systematic and integrative analysis of large gene lists using DAVID bioinformatics resources. *Nature protocols*, 4(1), (2008), 44.

Effect of Different Acid Components on Multi-Walled Carbon Nanotubes

Ugur Akbaba 

Kafkas University, Department of Physics Teaching, Kars, Turkey

ABSTRACT

In this study, interactions of multi-walled carbon nanotubes (MWCNTs) samples with Hydrochloric acid (HCl), Nitric acid (HNO_3), Aqua regia [(AR)=HCl: HNO_3 (3:1)] and Reverse aqua regia, [(RAR)=HCl: HNO_3 (1:3)] acid and acid mixtures were investigated. Changes in the structure of the samples were analyzed by Fourier transform infrared spectroscopy (FT-IR) and Raman spectroscopy. In addition, the adsorption rates of the acid solutions of the samples were determined. The MWCNTs material has been found to exhibit a high adsorption rate (%34.70) for the RAR mixture. The same mixture caused the highest defect formation in the structure (%25). The AR mixture significantly reduced the number of defects in the sample (%63). According to the purposes of industrial and technological applications, acid and acid mixtures can be used to purify carbon-based structures and to extend the surface area by adding functional groups to the structure.

Keywords:

MWCNTs, Defect formation, Adsorption rate, Acid interaction, Purification, Surface extending.

Article History:

Received: 2019/11/17

Accepted: 2019/12/03

Online: 2019/12/31

Correspondence to: Uğur Akbaba

Kafkas University, Department of Physics

Teaching

E-Mail: ugurakbaba@hotmail.com

INTRODUCTION

With the discovery of multi-walled carbon nanotubes (MWCNTs), it has become a desirable material in various technological applications. This material is desirable because of its unusual properties. These properties include the desired electrical, physical, optical and mechanical properties, thermal stability, large surface areas, tensile strength, and their ability to be modified according to the purpose [1-4]. Owing to this remarkable properties, MWCNTs and other forms of carbon based materials have a wide range of applications in technological applications. Drug delivery systems, biosensors, transistors, nanocomposites, nanoscale electronic devices, hydrogen storage devices, energy storage devices, composite-materials use MWCNTs and other carbon based materials (Single walled carbon nanotubes (SWCNTs), double walled carbon nanotubes (DWCNTs), graphene, Functionalization Carbon Nanotube (FCNTs), Buckypapers etc.) extensively [4,5]. The interaction of MWCNTs with different acid species causes serious modifications on the structure of the material. The changes resulting from this exposure may be beneficial and harmful according to the intended use. This interaction has been used to modify the material for purpose. Different methods such as laser vaporization, electric-arc discharge and chemical vapor deposition are used to produce MWCNTs. Very little of

the product obtained in this production process is MWCNTs, the other parts being undesirable nanocrystalline graphite, amorphous carbon, carbonyl structures such as fullerenes and other metals. These unwanted parts are regarded as defects in the structure and may need to be removed from the structure and purification of the structure according to the purpose of application [4]. Many different methods have been developed to remove these unwanted structures. The most common method used for purification is oxidative treatments using strong oxidizing acids [6]. In these acid treatments, HNO_3 , H_2SO_4 , HCl acids and mixtures of these acids in different ratios were used [7-9]. The effect of acid type, amount and acid mixture ratios applied varies in every carbon based structure. It was determined that amorphous carbon structures in SWCNTs were better removed by applying concentrated HNO_3 and H_2SO_4 mixtures, while HCl application was more effective in removing catalytic nanoparticles [10]. Carbon nanotubes tend to achieve thermodynamic stability by forming bonds with many π - π and Van der Waals interactions. Due to this tendency, it is quite difficult to obtain carbon structures having a homogeneous distribution. Many methods such as ultra-sonication, addition of surfactant, chemical modification of nanotube surface are used to disperse these bond struc-

tures. By adding functional groups to carbon nanotube surfaces, solubility and dispersibility of nanotubes can be improved. This allows the construction of new hybrid materials with liquid-compatible carbon content. One way to add a functional group to the surface is to expose the carbon material to the acid. Nitric acid was used for oxidation of MWCNTs structure. Graphite and metal catalytic structures were removed by gradual purification with a low acid concentration solution. Oxygenated groups were added to the surface of the MWCNTs using more concentrated acid solutions. This gives the opportunity to obtain functionalized materials which can be used in different technological applications [11]. In highly sensitive applications such as the construction of electronic devices, the production of chemical and biological sensors, carbon nanotube with high purity is required. Purification of this material is a highly popular field of research. For example, refluxing of nitric acid is extensively used in the purification of SWCNTs. In this purification process, foreign metals, amorphous carbons, graphite nanoparticles and other imperfections that are in the structure of SWCNTs are eliminated [12]. Observing the changes in the structure of MWCNTs subjected to three different chemical oxidation processes with gave interesting results. In these processes, sonication and refluxing techniques with H_2SO_4/HNO_3 acids were applied together and separately. As a result, intensive oxidation was detected in MWCNTs structure which was subjected to acidic sonication for 24 hours. The dimensions of the carbon nanotubes have changed significantly due to the damage occurring to the MWCNTs walls [5]. Another reason why multi-walled carbon nanotubes are preferred in technological applications is that they have a lower cost production process. But due to the van der Waals interactions inherent in this structure, its solubility is very low. This is the biggest obstacle to hybrid applications of the material. The best way to increase solubility is to form functional groups on the structure. By forming carboxylated groups, the modifiable structure is increased. Different functional groups can be introduced to the structure with different acidic treatments [13]. Sulfuric and nitric acid treatment was also applied to modify the surface of MWCNTs according to their intended use. By means of surface modification, the electrical, chemical and optical properties of the structure can be changed in accordance with the purpose. This provides flexibility to use in important technologies such as hydrogen storage and medical applications etc. [14]. When the structural analysis of MWCNTs subjected to nitric and sulfuric acid was done, it was found that after the acid application, the oxygen content increased in the structure and COOH groups formed on the nanotube surfaces. But these formations did not deform the carbon nanotube lattice. This is an important observation [15].

The ability of carbon-based structures to adsorb acid, other organic chemicals, heavy metals from aqueous solutions, and to store hydrogen is particularly useful for environmental cleaning, wastewater cleaning, and energy storage mechanisms. The toxic adsorption capabilities of carbon nanotubes (CNTs) are important for the environment and human health. Carbon-based structures owe these capabilities due to their large surface area, high reactivity, and unique hollow tube structure. With this motivation, many studies have been conducted especially on the adsorption mechanisms of MWCNTs. As a result of the activation of MWCNTs with different acid species, significant increases in surface areas occur according to the degree of functional group formation. This expansion of the surface area also results in significant yield increases in hydrogen storage applications. In this context, changes in the surface area of the HCl, HNO_3 , H_2SO_4 and HF acids in MWCNTs were investigated and it was found that HF acid significantly increased the surface area of the structure. Other acid types have increased their surface area less than HF acid [1]. It was found that fulvic acid (FA) was adsorbed by SWCNTs better than MWCNTs. The electrostatic, hydrophobic, π - π and hydrogen bond interaction mechanisms between FA and CNTs surfaces are the main causes of adsorption [16, 17]. The adsorption capacity of copper II ions by MWCNTs in the presence and absence of humic and fulvic acid environments was investigated. As a result of the study, it was observed that the presence of these acid environments positively affected the adsorption at pH values less than 7.5, but the ionic strength did not contribute to the adsorption process in the wide pH range. It was concluded that MWCNTs are the materials that can be used to remove heavy metals present in aqueous solutions [18]. MWCNTs modified by polyaluminum chloride in water treatment processes, which is one of the biggest problems of today, have been found to be a very effective material for removing humic acid from aqueous solution [19]. As a result of all interactions that cause adsorption, it is obvious that there are changes in the structure of the material such as defect formation, functional group formation, and defect reduction.

To observe the structural changes in MWCNTs lattice due to interaction acidic solutions with carbon-based structures, Transmission electron microscopy (TEM), thermogravimetric analysis (TGA), Raman spectroscopy, high-resolution, transmission electron microscopy (HR-TEM), Fourier transform infrared spectroscopy (FTIR), Field Emission Scanning Electron Microscopy (FE-SEM), Energy dispersive X-Ray spectroscopy (EDX), Thermal Gravimetric measurements (TG) are used extensively [5, 12, 15].

Here, the changes in the structure of MWCNTs exposed to HCl, HNO_3 , HCl: HNO_3 (3:1) and HCl: HNO_3 (1:3) acid and acid mixtures were determined by FT-IR and Ra-

man spectroscopy. It was also evaluated how much the material adsorbs these acid species. In particular, the interaction of HCl: HNO₃ (3: 1) and HCl: HNO₃ (1: 3) acid mixtures with MWCNTs has rarely been studied.

MATERIALS AND METHODS

MWCNTs with the diameter of 10-20 nm, length of 10-30 μm, and 99% purity (provided by Grafen Chemical Industries Co., Ltd.) were used in this examination. In different flasks, 30 mL concentrated HCl, HNO₃, HCl: HNO₃ (3:1) and HCl: HNO₃ (1:3) were added to MWCNTs (0.035 g). The mixtures were allowed to room temperature for 48 h. The mixture was poured into a pre-weighed Gooch crucible (no 3) to filter. After the filtrations, for obtaining percentage of adsorption, the Gooch crucibles and their contents were dried in room temperature and then weighed. FT-IR spectra were recorded from the solid samples in the range of 4000–600 cm⁻¹ by using a PerkinElmer Frontier FT-IR spectrometer with an ATR diamond accessory. For Raman experiments, a WITec alpha 300 R Micro-Raman spectrometer using a 532 nm wavelength laser with 0.5 mWatt laser power.

RESULTS AND DISCUSSION

MWCNTs Adsorption Percentages For Acids And Acids Mixtures

The percentages of adsorption of HCl, HNO₃, aqua regia (AR) and reverse aqua regia (RAR) on the MWCNTs were presented in the graph in Fig. 1.



Figure 1. The percentages of adsorption of HCl, HNO₃, aqua regia (AR) and reverse aqua regia (RAR) on the carbon nanotube.

When the adsorption rates in the Fig. 1 are considered, it is seen that the MWCNTs structure absorbs the most RAR acid mixture. The least adsorption rate is seen for HNO₃ acid. An interesting result is that MWCNTs absorb the acid mixtures more than the single acid species. Acidic structures are known to be harmful to living organisms. However, acid structures are used extensively in industrial applications. Acid pollution is one of the main factors, especially in the pollution of water resources. In this context, the graph gives remarkable results considering the removal of acid from aqueous media by MWCNTs [19-21].

FT-IR Spectra Results

FT-IR technique is one of the most effective methods for identifying and naming functional groups formed on carbon-based structures [5, 31]. The FT-IR spectra of MWCNTs, MWCNTs-HCl, MWCNTs-HNO₃, MWCNTs-AR (Aqua Regia) and MWCNTs-RAR (Reverse Aqua Regia) were given in Fig. 2.

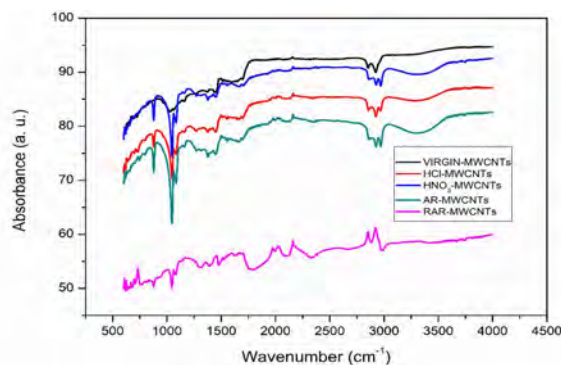


Figure 2. FT-IR Spectra of CNT, CNT-HCl, CNT-HNO₃, CNT-AR and CNT-RAR

The spectra of MWCNTs-HCl, MWCNTs-HNO₃, MWCNTs-AR and MWCNTs-RAR were evaluated by investigating the changes in the vibration modes of the functional groups of the CNT. FT-IR spectra of MWCNTs observed dominant peaks at 1030, 1283, 1328, 1443, 2852 and 2973 cm⁻¹ attribute to Si-O, C-N, N-CH₃, CNT, and C-H stretching vibrations, respectively [22]. The Si-O vibration bands were showed at 1046 cm⁻¹ for MWCNTs-HCl, MWCNTs-HNO₃, MWCNTs-AR and MWCNTs-RAR. The N-CH₃ stretching frequencies for MWCNT-HCl, MWCNTs-HNO₃, MWCNTs-AR and MWCNTs-RAR were appeared at 1373, 1378, 1378 and 1397 cm⁻¹, respectively. The characteristic vibration band related to MWCNTs displayed at 1454 cm⁻¹ (for MWCNTs-HCl), 1454 cm⁻¹ (for MWCNTs-HNO₃), 1456 cm⁻¹ (for MWCNTs-AR) and 1480 cm⁻¹ (for MWCNTs-RAR). The C-H stretching vibrations were observed at 2973 and 2924 cm⁻¹ (for MWCNTs-HCl), 2970 and 2923 cm⁻¹ (for MWCNTs-HNO₃), 2926 and 2970 cm⁻¹ (for MWCNTs-AR) and 3010 and 2976 cm⁻¹ (for MWCNTs-RAR). Unlike the vibrations of MWCNTs, the Q-branch for HCl was showed at 2855 cm⁻¹ (for MWCNTs-HCl), 2836 cm⁻¹ (for MWCNTs-AR) and 2880 cm⁻¹ (for MWCNTs-RAR) [23, 24]. The broad band in the region 3500–3300 cm⁻¹ in FT-IR spectra of MWCNTs-HNO₃, MWCNTs-AR and MWCNTs-RAR was attributed to O-H stretching vibrations of nitric acid. Similarly, the NO₂ stretching vibrations of nitric acid were observed at 1688 cm⁻¹ (for MWCNT-HNO₃), 1698 cm⁻¹ (for MWCNTs-AR) and 1699 cm⁻¹ (for MWCNTs-RAR) [25]. When the results are examined, the shifts occurring after acid exposure at characteristic peaks indicate that the acid structures penetrate the MWCNTs structure to different sizes and form different functional groups. Again, the significant shift in characte-

ristic carbon peaks in the sample exposed to the RAR acid mixture is noteworthy. The highest adsorption rate was determined in this mixture.

Raman Results

Raman spectroscopy is the most widely used reliable technique for characterizing different carbon based structures such as graphite-like and diamond-like [26]. The ratio of the D band showing the vibrations of the defects and the G band showing the graphitization (ID/IG) is the quality parameter of these structures. The low rate means that the better structure quality. Again, the shifts in the formation points of the D, G and 2D bands are clues indicating the changes in the structure [27]. Fig. 3 presents Raman spectra of virgin MWCNTs sample and MWCNTs samples subjected to various acid and acid mixtures.

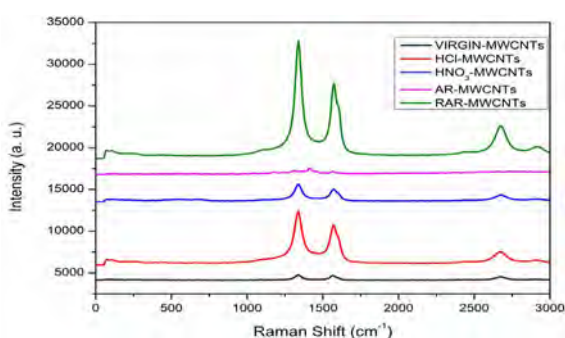


Figure 3. Raman spectra of virgin MWCNTs and MWCNTs subjected to HCl, HNO₃, AR and RAR acids solutions.



Figure 4. ID/IG ratios obtained from the analysis of Raman spectra.

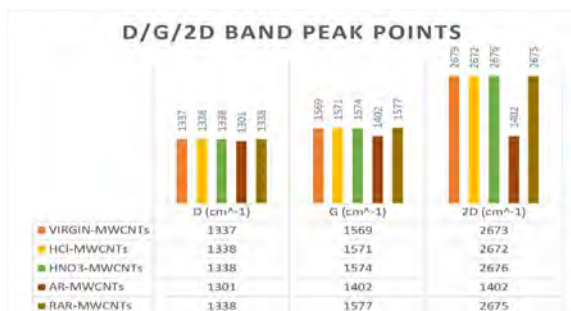


Figure 5. Bands peak points of virgin and acidified samples.

Raman results (in Figs. 3 and 4) show that the highest defect rate is in the sample subjected to RAR mixture. There has been a 25% defect increase compared to the virgin sample. On the contrary, the sample exposed to AR mixture shows a significant reduction in defect formation (63%) compared to the virgin sample. In the samples exposed to HCl and HNO₃ solutions, the defect increase was 18% and 24% respectively. Since some industrial and technological applications require high purity MWCNTs, the applicability of the AR mixture in the purification process of MWCNTs should be evaluated. It is also notable that band peaks shifts in the same sample (in Fig. 5). The adsorption rate of the sample (34.70%) exposed to the RAR mixture is highest (in Fig. 1). The highest adsorption rate and defect formation rate in this sample are compatible results. The structure of MWCNTs is believed to be suitable for removing the mixture in an environment where the RAR mixture is present. There are also visible differences in the FT-IR graph (in Fig. 2) of the sample that has been subjected to the RAR sample compared to the other samples graphs. This shows that the structure adsorbs this solution intensely and new functional groups are formed as a result of adsorption. When other adsorption rates are examined, it is seen that this structure absorbs acid mixtures better than pure acid contents. These results can be taken into account for environmental health and water treatment.

CONCLUSION

In this study, MWCNTs were exposed to HCl, HNO₃, HCl: HNO₃ (3: 1, aqua regia, AR) and HCl: HNO₃ (1: 3, reverse aqua regia, RAR) acids and acid mixtures. Changes in MWCNTs structure were investigated by FT-IR, Raman spectroscopy techniques. In addition, its reaction to the solutions was examined with adsorption rates. MWCNTs samples were determined to adsorb AR and RAR acid mixtures better than single acid type. The highest adsorption was obtained for RAR solution. When FT-IR spectra are considered, the most intense functional group formation occurs in the RAR mixture. Raman analysis shows that the most intense defect formation occurs within this sample. In terms of purification, the AR mixture was found to be very suitable with a 63% defect reduction. The shifts in FT-IR and Raman peaks show that the material reacts more with the acid mixtures rather than the single acid type. The electrostatic, hydrophobic hydrogen and π - π coactions, which are the cause of these interactions, are indicative of the interaction densities between the structure and acid mixtures. The results obtained should be taken into account in the purification of MWCNTs and in the expansion of the surface area by forming functional groups. The results can be examined in more detail for the hydrogen storage process and additional investigations can be made. Adsorption capabilities according to acid types can be considered for

waste treatment and environmental health.

ACKNOWLEDGEMENT

This study was supported by the scientific research project unit of Kafkas University in Turkey under the project number (2016-FM-71).

REFERENCES

1. Reyhani A, Mortazavi SZ, Golikand AN, Moshfegh AZ, Mirershadi S. The effect of various acids treatment on the purification and electrochemical hydrogen storage of multi-walled carbon nanotubes. *Journal of Power Sources*, 183 (2) (2008) 539-543.
2. Špitalský Z, Aggelopoulos C, Tsoukleri G, Tsakiroglou C, Parthenios J, Georga S, Krontiras C, Tasis D, Papagelis K, Galiotis C. The effect of oxidation treatment on the properties of multi-walled carbon nanotube thin films. *Materials Science and Engineering: B* 165(3) (2009) 135-138.
3. Saleh TA. The influence of treatment temperature on the acidity of MWCNT oxidized by HNO₃ or a mixture of HNO₃/H₂SO₄. *Applied Surface Science* 257(17) (2011) 7746-7751.
4. Kruusenberg I, Alexeyeva N, Tammeveski K, Kozlova J, Matisen L, Sammelselg V, Gulo'n JS, Feliu JM. Effect of purification of carbon nanotubes on their electrocatalytic properties for oxygen reduction in acid solution. *Carbon* 49(12) (2011) 4031-4039.
5. Maciejewska BM, Jasiurkowska DM, Vasylenko AI, Koziol KK, Jurga S. Experimental and theoretical studies on the mechanism for chemical oxidation of multiwalled carbon nanotubes. *RSC Advances* 4(55) (2014) 28826-28831.
6. MacKenzie K, Dunens O, Harris AT. A review of carbon nanotube purification by microwave assisted acid digestion. *Separation and Purification Technology* 66(2) (2009) 209-222.
7. Pumera M, Šmíd B, Veltruská K. Influence of nitric acid treatment of carbon nanotubes on their physico-chemical properties. *Journal of Nanoscience and Nanotechnology* 9(4) (2009) 2671-2676.
8. Shen L, Liu M. A New Purification Way for Multi-walled Carbon Nanotubes. In *Applied Mechanics and Materials* (Trans Tech Publications) 457 (2014) 240-243.
9. Pillai SK, Ray SS, Moodley M. Purification of multi-walled carbon nanotubes. *Journal of nanoscience and nanotechnology*, 8(12) (2008) 6187-6207.
10. Chiang IW, Brinson BE, Huang AY, Willis PA, Bronikowski MJ, Margrave JL, Smalley RE, Hauge RH. Purification and characterization of single-wall carbon nanotubes (SWNTs) obtained from the gas-phase decomposition of CO (HiPco process). *The Journal of Physical Chemistry B* 105(35) (2001) 8297-8301.
11. Yudianti R, Onggo H, Saito Y, Iwata T, Azuma JI. Analysis of functional group sited on multi-wall carbon nanotube surface. *The Open Materials Science Journal* 5(1) (2011).
12. Hu H, Zhao B, Itkis ME, Haddon RC. Nitric acid purification of single-walled carbon nanotubes. *The Journal of Physical Chemistry B* 107(50) (2003) 13838-13842.
13. Lee GW, Kim J, Yoon J, Bae J S, Shin BC, Kim IS, Oh Weontae, Ree M. Structural characterization of carboxylated multi-walled carbon nanotubes. *Thin Solid Films*, 516(17) (2008) 5781-5784.
14. Turgunov MA, Oh JO, Yoon SH. Surface modification of multiwall carbon nanotubes by sulfuric acid and nitric acid. *Materials* 64 (2014) 22-25.
15. Le TMH. Characterization of multi-walled carbon nanotubes functionalized by a mixture of HNO₃/H₂SO₄. *Diamond and Related Materials* 89 (2018) 43-51.
16. Yang K, Xing B. Adsorption of fulvic acid by carbon nanotubes from water. *Environmental Pollution* 157(4) (2009) 1095-1100.
17. Pan B, Xing B. Adsorption mechanisms of organic chemicals on carbon nanotubes. *Environmental Science & Technology* 42(24) (2008) 9005-9013.
18. Sheng G, Li J, Shao D, Hu J, Chen C, Chen Y, Wang X. Adsorption of copper (II) on multi-walled carbon nanotubes in the absence and presence of humic or fulvic acids. *Journal of Hazardous Materials* 178(1-3) (2010) 333-340.
19. Li S, Li Z, Ke B, He Z, Cui Y, Pan Z, Li D, Su J, Lai C, Su J. Magnetic multi-walled carbon nanotubes modified with polyaluminium chloride for removal of humic acid from aqueous solution. *Journal of Molecular Liquids* 279 (2019) 241-250.
20. Liesivuori J, Savolainen AH. Methanol and formic acid toxicity: biochemical mechanisms. *Pharmacology & Toxicology* 69(3) (1991) 157-163.
21. Kudo N, Kawashima Y. Toxicity and toxic-kinetics of perfluorooctanoic acid in humans and animals. *The Journal of Toxicological Sciences* 28(2) (2003) 49-57.
22. Misra A, Tyagi PK, Rai P, Misra DS. FTIR Spectroscopy of multi-walled carbon nanotubes: a Simple approach to study the nitrogen doping. *Journal of nanoscience and nanotechnology* 7(6) (2007) 1820-1823.
23. Perez J, Velasco S, White JA, Hernández AC. Infrared spectra of HCl, HBr and HI dissolved in liquid xenon. *Journal of Molecular Liquids* 45(1-2) (1990) 71-76.
24. Lehman JH, Terrones M, Mansfield E, Hurst KE, Meunier V. Evaluating the characteristics of multiwall carbon nanotubes. *Carbon* 49(8) (2011) 2581-2602.
25. Robert MS, Francis XW, David JK. *Spectrometric identification of organic compounds*. seventh ed. John Wiley & Sons, Inc, Hoboken, (106) 2005.
26. Antunes EF, Lobo AO, Corat EJ, Airoldi VJT, Martin AA, Veríssimo C. Comparative study of first-and second-order Raman spectra of MWCNT at visible and infrared laser excitation. *Carbon* 44(11) (2006) 2202-2211.
27. Akbaba U, Kasapoğlu AE, Gür E. Gamma and neutron irradiation effects on multi-walled carbon nanotubes. *Diamond and Related Materials* 87 (2018) 242-247.

